Thermodynamically constrained closed-form surface energy balance using medium-resolution remote sensing for efficient evapotranspiration mapping

Yeonuk Kim[a,*], Justin L Huntington[a], Bruno Comini de Andrade[b], Mark S Johnson[c,d], John M Volk[a], Sayantan Majumdar[a], Charles Morton[a], Peter ReVelle[a]

Affiliations

a. Division of Hydrologic Sciences, Desert Research Institute, Reno, Nevada, USA
b. Hydraulic Research Institute, Federal University of Rio Grande do Sul, Porto Alegre, Brazil
c. Institute for Resources, Environment and Sustainability, University of British Columbia, Vancouver, BC, Canada
d. Department of Earth, Ocean and Atmospheric Sciences, University of British Columbia, Vancouver, BC, Canada

Corresponding author: Yeonuk Kim (yeonuk.kim@dri.edu)

This manuscript is a non-peer reviewed preprint submitted to EarthArXiv.

Abstract

Medium-resolution (10-100 m) satellite evapotranspiration (ET) products are rapidly advancing agricultural water resources research and management, however, underperformance across non-agricultural land cover limits research and application potentials more broadly. These inconsistencies are the result of multiple factors, including model structure and representation of ET dynamics across space and time. In regionally expansive land covers such as forests and shrublands, ET is primarily governed by equilibrium radiative energy exchange, whereas in croplands it is often amplified by advected heat from adjacent water-limited areas. While select models represent these processes, opportunities for improved conceptual and numerical representation are clear based on recent satellite ET model intercomparison studies. Here, we introduce a thermodynamic constraint in which ET is independent of aerodynamic conductance, enabling a closed-form analytical solution to the two-source surface energy balance under advection-free conditions. To account for advection, we conditionally incorporate an aerodynamic term where and when advection is significant. Landsat thermal, optical, and land cover data are used in combination with gridded meteorological data within the presented Radiation Advection Diffusivity-independent ET (RADET) modeling framework to predict ET. Performance is evaluated using in situ flux observations at daily and monthly scales across the contiguous United States (CONUS) along with intercomparisons to the widely used operational OpenET and MODIS products. Results indicate that RADET has superior performance across all land cover classes, with substantial improvements in forests and shrublands. Application of Landsat data with novel analytical solutions of the surface energy balance enables computationally efficient generation of medium-resolution ET products at scale with good performance across all land cover, advancing research and application potentials across many disciplines.

Keywords

satellite remote sensing, Landsat, evapotranspiration, equilibrium, advection

Highlights

- Proposed RADET, a Radiation Advection Diffusivity-independent ET framework
- Generated 30 m daily and monthly ET maps using Landsat and gridded meteorology
- Comparable to OpenET in croplands, with superior performance elsewhere
- Outperformed MODIS ET products across both managed and natural landscapes
- Computationally efficient and operational scalable via Google Earth Engine

1. Introduction

Evapotranspiration (ET), the sum of plant transpiration and soil evaporation, is the second-largest terrestrial hydrologic flux after precipitation and commonly represents the dominant loss term in terrestrial water budgets (Oki & Kanae, 2006). It is a key variable that governs runoff, aquifer recharge, and water availability for ecosystems and society (Wang & Dickinson, 2012). ET also serves as a key linkage among the water, carbon, and energy cycles (Gentine et al., 2019). It modulates weather and climate, and reflects soil moisture conditions indicative of drought severity and ecosystem function (Katul et al., 2012). Because of these roles, accurate, spatiotemporally continuous ET mapping using medium- to moderate-resolution (~10-100 m and 100-1000 m scale) satellite imagery has substantial practical relevance, with applications including improved water resources management through more accurate estimation of water availability and sectoral use, advances in climate research via characterization of long-term variability and coupled land-atmosphere processes, and enhanced agricultural and ecosystem management through improved drought monitoring and wildfire risk assessment (Fisher et al., 2017; Loveland et al., 2022; Radeloff et al., 2024; Seitzinger et al., 2026).

Despite the availability of numerous satellite-based ET models and products, their widespread adoption for routine decision-making by water and land management agencies, farmers, and practitioners remains limited (Kumar et al., 2024). Key barriers include operational constraints, coarse spatial resolution, and inconsistent performance across land cover types (Jung et al., 2019; Miralles et al., 2025). Many global ET products, such as FLUXCOM and GLEAM, are available only at kilometer-scale spatial resolutions and lack timely low-latency operational updates (Mu et al., 2011; Zhang et al., 2019). MODIS-based ET products, including MOD16 and PML-V2 (Radeloff et al., 2024), are widely used for regional-scale assessments; however, their moderate resolution (500 m) limits applicability for field- to small watershed-scale agricultural and water resource management (McCabe & Wood, 2006), and their performance is limited in croplands and wetlands (Fisher et al., 2020; Pierrat et al., 2025). More recently, ECOSTRESS thermal observations have enabled the development of instantaneous ET products, including ECO3ETPTJPL and ECO3ETALEXI, at ~70 m spatial resolution with revisit intervals of approximately 1–5 days and observations acquired at varying local times. However, their utility for routine resource applications remains constrained by limited historical coverage, irregular temporal sampling and need for temporal upscaling, and variable performance across land cover types (Fisher et al., 2020; Pierrat et al., 2025).

OpenET is an operational medium-resolution Landsat-based ensemble ET product (Melton et al., 2022), which integrates six well-established remote sensing ET models including eeMETRIC, ALEXI/DisALEXI, geeSEBAL, PT-JPL, SIMS, and SSEBop (Allen et al., 2007; Anderson et al., 2012; Bastiaanssen et al., 1998; Fisher et al., 2008; Melton et al., 2012; Senay, 2018). Owing to its high public accessibility, medium-resolution (30 m), strong performance in croplands, and operational delivery through Google Earth Engine cloud computing (Gorelick et al., 2017), OpenET is now widely used for agricultural water use assessments by federal, state, and local agencies, consulting firms, and farmers (Huntington et al., 2025; Martin et al., 2025; Ott et al., 2024; Pearson et al., 2024; Romera & Silver, 2025; Wobus et al., 2025)(Reitz et al., 2025; Volk et al., 2024). However, despite its demonstrated accuracy in croplands, OpenET performance is more limited across other land cover types and exhibits well-documented systematic biases (Reitz et al., 2025; Volk et al., 2024). In particular, OpenET models exhibit greater uncertainty and systematic positive bias in forested ecosystems, which can result in overestimation of ET and poor water balance closure in forest-dominated watersheds (Khand et al., 2025; Nassar et al., 2025). Consequently, OpenET applications remain predominantly agricultural, despite considerable potential for multidisciplinary research and water resource management, underscoring the need for medium-resolution ET estimation approaches that are robust across diverse land cover types.

We hypothesize that variable performance of medium-resolution ET models across land cover types reflects fundamental differences in land–atmosphere coupling rather than satellite limitations (e.g. Landsat's 8-16 day revisit frequency). Many ET models scale instantaneous ET to daily and longer timescales as a function of reference ET (ETo), whereby increased atmospheric dryness enhances ETo through Penman's aerodynamic term and, in turn, increases estimated ET (Allen et al., 2007; Allen et al., 2005; Melton et al., 2012; Senay et al., 2013). Over irrigated croplands, atmospheric dryness often results from advection of warm, dry air from surrounding arid regions, leading to increased ET that can exceed locally available radiative energy (de Bruin et al., 2016; Rana & Katerji, 2000). In contrast, over natural landscapes where advective influences are weak, atmospheric dryness largely reflects reduced ET, and elevated ETo indicates suppressed rather than enhanced ET, consistent with the complementary relationship of evaporation framework (Bouchet, 1963; Brutsaert & Stricker, 1979; Morton, 1969). This contrast helps explain strong model performance over croplands and degraded performance over extensive natural land covers where land–atmosphere coupling is strongest. Additional uncertainties arise from neglected biomass heat storage in tall forest canopies (Lindroth et al., 2010), errors in semi-empirical aerodynamic conductance—particularly over rough forest canopies where small surface-air temperature gradients render aerodynamic conductance the primary control on sensible heat flux (Melton et al., 2022)—and the common assumption of constant evaporative fraction or ETo fraction when upscaling instantaneous ET to daily or longer time scales, which frequently breaks down (Cammalleri et al., 2014; Crago & Brutsaert, 1996; Gentine et al., 2011; Liu, 2021).

2. Objectives

Despite decades of satellite-based ET model development and continued advances in remote sensing observations, these limitations remain only partially addressed. In some settings, parsimonious frameworks with little or no reliance on satellite inputs—such as complementary relationship and surface flux equilibrium theories—have been shown to achieve performance comparable to, or in some cases or exceeding, that of more complex satellite-driven approaches (Comini de Andrade et al., 2025; Thakur et al., 2025). Together, these findings motivate continued refinement of ET model structures grounded in land-atmosphere feedback theory that build upon foundational scientific advances and strategically leverage medium-resolution thermal and optical satellite observations to deliver robust, scalable, operationally viable ET estimates for water resources research and applications from field to national scales.

Our objective is to accurately map ET at 30-m resolution across diverse land cover types while maintaining operational scalability. We introduce RADET (Radiation Advection

Diffusivity-independent Evapotranspiration), a physically-based model build on four elements: (1) a diffusivity-independent flux hypothesis that yields a closed-form analytical solution for ET under advection-free conditions without aerodynamic conductance parameterization; (2) direct estimation of daily ET from the instantaneous satellite observations, avoiding constant evaporative fraction assumptions and minimizing canopy heat storage issues; (3) separate treatment of canopy and soil to represent distinct stomatal and soil-water controls; and (4) conditional inclusion of the Penman's aerodynamic term where advection effects are expected. We apply RADET to Landsat imagery, gridded daily meteorology, and annual land cover data, and evaluate performance against in situ ET data and common satellite ET products across the conterminous United States.

3. Theoretical basis and model description

3.1. The diffusivity-independent flux hypothesis

Evaporation converts liquid water to vapor by consuming energy. The newly formed vapor raises the water vapor pressure at the surface–air interface, creating a vertical gradient in vapor density between the surface skin and the reference height air. This gradient, together with turbulent mixing, drives a vertical water vapor flux according to Fick's law. Efficient turbulent mixing, which is typically parameterized by aerodynamic conductance (g_a), is therefore frequently interpreted as enhancing ET. While this interpretation may appear intuitive, it does not necessarily hold, particularly at aggregated temporal scales.

Early atmospheric boundary layer (ABL) theories showed that, as the ABL evolves toward steady state over spatially extensive wet surfaces where advection is minimal, ET approaches an "equilibrium ET" that is independent of g_a (McNaughton, 1976; Priestley & Taylor, 1972; Slatyer & McIlroy, 1961). Accordingly, several studies explicitly define equilibrium ET as the state in which ET is independent of g_a (Monteith, 1965; Raupach, 2001). This wet-surface equilibrium ET was originally framed as a theoretical upper bound, rather than as a general description of actual ET under natural conditions. To bridge this gap, approaches based on complementary relationship (CR) were developed to estimate actual ET from equilibrium ET and Penman's potential ET (Brutsaert & Stricker, 1979; Morton, 1969). Within CR-type formulations, increases in g_a (or wind speed) do not enhance ET, contrasting with the expectation of a positive relationship between g_a and ET.

The insensitivity of ET to g_a has also been demonstrated experimentally. Davarzani et al. (2014) used wind-tunnel experiments coupled with a Navier–Stokes free-flow model to demonstrate that soil evaporation becomes progressively insensitive to wind speed as the coupled soil–atmosphere system approaches steady state at multiday time scales. Consistent with these findings, Surface Flux Equilibrium (SFE) theory further demonstrates that even over dry land surfaces, parsimonious ABL dynamics with minimal advection can evolve toward a steady state in which actual ET is well approximated by SFE evaporation that is independent of g_a (McColl & Rigden, 2020; McColl et al., 2019). Consistent evidence also comes from eco-physiological studies that commonly assume canopy surface and atmospheric vapor pressure deficits are equal at daily time scale (e.g., Beer et al., 2009; Keenan et al., 2013), an assumption equivalent to ET being independent of g_a (Monteith, 1965).

If these lines of evidence are broadly applicable across a wide range of conditions, an important question arises: how can ET become insensitive to g_a? From an atmospheric dynamics perspective, the weak dependence of ET on g_a can be understood as a compensating feedback between g_a and the vertical humidity gradient (e.g., Salvucci & Gentine, 2013). Stronger turbulent mixing, represented by higher g_a, reduces the vertical humidity gradient, while weaker mixing, represented by lower g_a, allows the gradient to increase (Figure 1). This compensating adjustment results in near-invariant ET despite variations in g_a. Such feedback emerges when turbulent mixing is not a limiting factor of ET. For example, in chemical engineering or cloud microphysics, a dimensionless quantity Damköhler number (Da) is widely used to characterize whether a system is limited by phase change process (evaporation) or by turbulent transport (e.g., Kumar et al., 2018). When evaporation proceeds much more slowly than the turbulent transport capacity due to constraints such as limited water availability or energy supply, ET can become independent of g_a.

Given this reasoning and these lines of evidence, we posit that daily aggregated ET is subject to the following constraint under typical advection-free conditions:

$$\frac{\partial ET}{\partial g_a} \approx 0 \tag{1}$$

This constraint is equivalent to assuming that the water vapor flux is independent of eddy diffusivity. Thus, we refer to Equation (1) as the Diffusivity-independent flux (DIF) hypothesis in which phase change process (evaporation), not transport efficiency, control water vapor flux under advection-free conditions, allowing ET to be expressed without parameterization of g_a.

Importantly, the DIF hypothesis does not imply that turbulence, surface roughness, or atmospheric stability are negligible, but rather that their effects are implicitly embedded in surface–air gradients when land–atmosphere coupling is strong. Where this assumption is violated—such as under advective forcing, heterogeneous roughness, or atmospheric decoupling—the DIF framework is not expected to hold, motivating the conditional inclusion of aerodynamic controls.

The main exception to the DIF hypothesis occurs when the surface remains consistently close to saturation while the overlying atmosphere is dry (e.g., under advective conditions) (Figure 1). In this situation, the humidity gradient is fixed and cannot adjust to changes in turbulent mixing. Under such wet surface conditions (e.g., irrigated cropland, open water, wetland, riparian), efficient turbulent mixing can increase ET (i.e., $\frac{\partial ET}{\partial g_a} > 0$), which is consistent with the addition of an aerodynamic or "drying power of the air" term in Penman's energy balance-bulk mass transfer combination equation, and interpreted as a measure of the departure from equilibrium conditions (Brutsaert & Stricker, 1979; Penman, 1948).

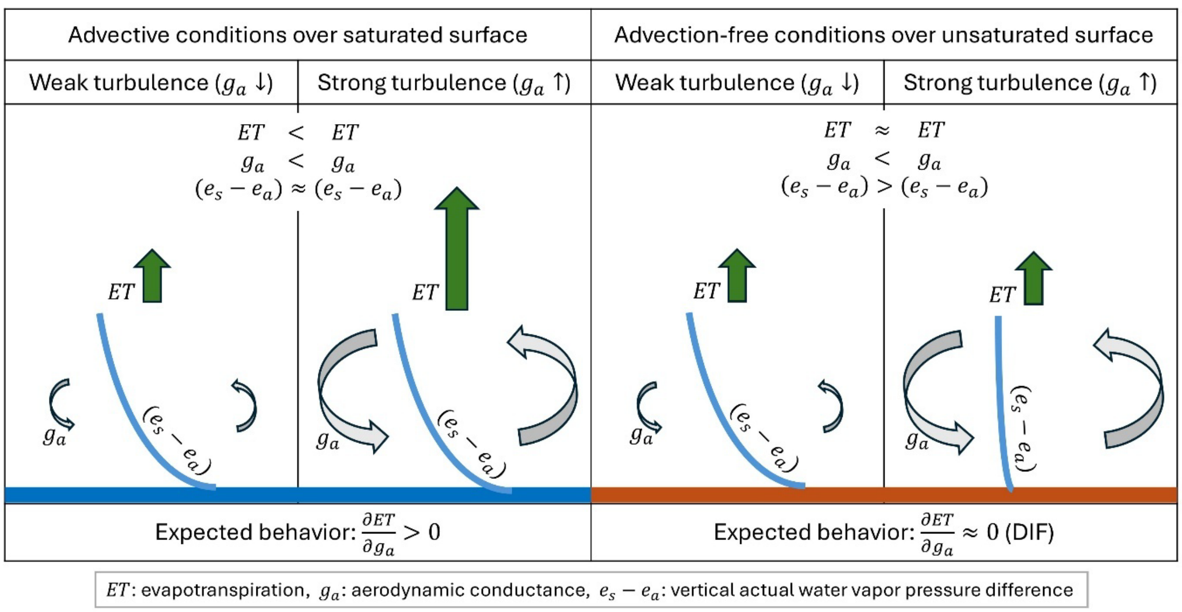

Figure 1 Schematic diagram illustrating the diffusivity-independent flux (DIF) hypothesis. Under advective conditions, evapotranspiration increases with aerodynamic conductance, whereas under advection-free conditions this dependence weakens due to adjustment of the humidity gradient. In both cases, ET is a function of the product of aerodynamic conductance and the vertical water vapor pressure difference.

3.2. Evapotranspiration under the DIF hypothesis

The DIF constraint was originally introduced as an analytical expression for equilibrium ET (Monteith, 1965; Raupach, 2001). Specifically, substituting Equation (1) into the Penman or

Penman-Monteith (PM) equations yields conventional equilibrium ET when the dependence of land surface temperature (LST) on g_a is neglected. Raupach (2001) further introduced the concept of isothermal net radiation (Martin, 1989; Monteith, 1981) to remove the explicit LST term from the PM formulation, thereby deriving radiatively-coupled equilibrium ET via the DIF constraint.

Building on this theoretical foundation, we derive an ET formulation under the DIF hypothesis in Appendices A and B. While the formulation by Raupach (2001) retains an explicit dependence on g_a, we remove this dependency by reintroducing LST after applying the DIF constraint. As a result, g_a no longer appears in the final expression, and the temperature difference between LST and air temperature (T_a) emerges as the primary control on equilibrium ET. This reformulation is particularly advantageous for ET modeling, as LST is directly observable from satellite remote sensing. We further found that parameterizing surface water constraints using surface conductance representing stomatal conductance versus surface relative humidity representing soil surface water potential produces distinct outcomes under the DIF hypothesis (Kim et al., 2023). To capture this difference, we adopt a two-source framework and apply the DIF assumption separately to canopy and soil. As derived in Appendices A and B, introducing the DIF assumption into the two-source surface energy balance ultimately yields the following analytical expression:

$$ET_{DIF} = \frac{1}{L_v}[\underbrace{\frac{\Delta R_{nc}}{\Delta + \mu_c \gamma}}_{canopy} + \underbrace{\frac{RH_s \Delta (R_{ns} - G)}{RH_s \Delta + \mu_s \gamma}}_{soil}] \tag{2}$$

where ET_{DIF} is daily ET under the DIF assumption (mm d^{-1}); L_v is latent heat of vaporization (MJ kg^{-1}); Δ is the slope of the saturation vapor pressure curve at T_a (kPa K^{-1}); γ is the psychrometric constant (kPa K^{-1}); R_{nc} and R_{ns} are net radiation at canopy and soil surface, respectively (MJ m^{-2} d^{-1}); G is the soil heat flux (MJ m^{-2} d^{-1}) ; RH_s is the relative humidity at the soil surface (kPa kPa^{-1}). μ_c and μ_s are nondimensional parameters, which are defined as follows:

$$\mu_c = \frac{R_{nc} + 8(1-\tau_L)\varepsilon\sigma {T_a}^3 (T_c - T_a)}{2R_{nc}} + \frac{\sqrt{[R_{nc} + 8(1-\tau_L)\varepsilon\sigma {T_a}^3 (T_c - T_a)]^2 + 32\frac{\Delta}{\gamma} R_{nc}(1-\tau_L)\varepsilon\sigma {T_a}^3 (T_c - T_a)}}{2R_{nc}} \tag{3a}$$

$$\mu_s = \frac{AE_s + (4\varepsilon\sigma {T_a}^3 + \frac{k_g}{d_g})(T_s - T_a)}{2AE_s} + \frac{\sqrt{[AE_s + (4\varepsilon\sigma {T_a}^3 + \frac{k_g}{d_g})(T_s - T_a)]^2 + 4\frac{RH_s\Delta}{\gamma}AE_s(4\varepsilon\sigma {T_a}^3 + \frac{k_g}{d_g})(T_s - T_a)}}{2AE_s} \qquad (3b)$$

where T_c and T_s are canopy and soil surface temperature, respectively, derived from Landsat LST; ε is the Landsat-derived surface emissivity; $\sigma(= 4.901 \times 10^{-9})$ is Stefan-Boltzmann constant (MJ K^{-4} m^{-2} d^{-1}); $AE_s(= R_{ns} - G)$ is available energy at the soil surface (MJ m^{-2} d^{-1}); τ_c is the transmissivity of diffuse longwave radiation through the canopy (details in section 2.3.2); $\frac{k_g}{d_g}$ is soil thermal conductivity (MJ m^{-1} K^{-1} d^{-1}) divided by a soil storage length scale (m), and $\frac{k_g}{d_g}$ is treated as effective conductive exchange coefficient (details in section 2.3.7).

The canopy component of ET_{DIF} aligns with conventional equilibrium ET formulations (Slatyer & McIlroy, 1961), whereas the soil component resembles surface flux equilibrium ET (McColl et al., 2019). A key distinction is that ET_{DIF} explicitly incorporates μ_c and μ_s parameters. In principle, μ_c and μ_s become unity when $T_c = T_a$ and $T_s = T_a$, and exceed unity when $T_c > T_a$ and $T_s > T_a$. This indicates that ET_{DIF} decreases with increasing vertical temperature difference. This vertical temperature-difference adjustment is conceptually similar to other ET models derived from distinct thermodynamic perspectives, including Hamiltonian based approaches and a combined framework linking equilibrium ET with the maximum entropy production principle (Kim et al., 2023; Liu et al., 2012; Pan et al., 2024). The demonstrated skill of these methods in estimating ET further supports the robustness of the DIF hypothesis for broad range of conditions.

3.3. The RADET model

The proposed ET_{DIF} in Equation (2) can lead to significant bias when the DIF assumption is violated. As illustrated in Figure 1, the DIF assumption is not theoretically valid particularly under advective conditions over wet surfaces. To accurately estimate ET even if the DIF assumption breaks down, we propose the Radiation Advection Diffusivity-independent Evapotranspiration (RADET) model, which conditionally incorporates Penman's aerodynamic term (Penman, 1948).

$$ET_{RAD} = ET_{DIF} + \delta_{LC}\delta_{WET}\frac{\gamma f(u) VPD_a}{\Delta + \gamma} \qquad (4)$$

where δ_{LC} is a nondimensional parameter, which is an advection switch based on land cover types. δ_{WET} is a parameter identifying a wet surface. The product of these two δ parameters is Penman's aerodynamic term, where *f(u)* is the empirical wind function and VPD_a is the vapor pressure deficit at the reference height (kPa).

Because Penman's aerodynamic term is commonly interpreted as representing regional-scale advection (de Bruin et al., 2016), we add this term to correct ET_{DIF} in situations where the DIF assumption is violated due to advection. Land cover information is used to identify conditions conducive to advective enhancement, and δ_{WET} is used to detect wet surfaces. Further details on the δ parameters and the wind function are provided in Section 2.4.7.

3.4. Satellite derived parameters for RADET

In this section, we describe how medium-resolution satellite remote-sensing observations, combined with gridded meteorological data, are used to compute RADET. Our implementation focuses on Landsat observations and the gridMET meteorological dataset, although the same principles can be applied to other satellite sensors and meteorological products.

3.4.1. Daily land surface temperature

The instantaneous land surface temperature observed by the Landsat satellite and the daily minimum air temperature ($T_{a,min}$) from gridMET are used to estimate the daily mean land surface temperature (LST_{daily}). We first assume that the minimum land surface temperature (LST_{min}) is slightly lower than $T_{a,min}$, as commonly observed across various environments (Good, 2016).

$$LST_{min} \approx T_{a,min} - offset \tag{5}$$

We set offset as 1 K. Next, the maximum land surface temperature (LST_{max}) is estimated using a cosine function (Göttsche & Olesen, 2001).

$$LST_{max} = LST_{min} + \frac{LST_{10am} - LST_{min}}{\cos\left(\frac{\pi}{2} \cdot \frac{10 - t_{max}}{t_{max} - t_{min}}\right)} \tag{6}$$

where LST_{10am} is Landsat satellite observed land surface temperature around 10:00; t_{max} is the peak time of land surface temperature, which is assumed as 12:30; t_{min} is the local sunrise time (i.e., time corresponding to LST_{min}).

The daily mean land surface temperature is then calculated as:

$$LST_{daily} = \frac{LST_{min} + LST_{max}}{2} \quad (7)$$

When the estimated LST_{daily} from Equation (7) is lower than the griMET daily mean air temperature ($T_{a,daily}$), we set $LST_{daily} = T_{a,daily}$ to prevent unrealistic underestimation of land surface temperature.

The daily outgoing longwave radiation (LW_{out}, MJ m^{-2} d^{-1}) is computed using the Stefan-Boltzmann law:

$$LW_{out} = \varepsilon\sigma {LST_{daily}}^4 \quad (8)$$

Here, LST_{daily} is in Kelvin.

This approach was evaluated against in-situ outgoing longwave radiation measurements from flux tower sites (Figure S1). The results show that the coefficient of determination (R^2) exceeds 0.9 across all land cover types, with slopes close to 1, suggesting high accuracy of the proposed approach when applied to Landsat.

3.4.2. Daily canopy and soil surface temperature

We estimate the daily mean canopy surface temperature ($T_{c,daily}$) and soil surface temperatures ($T_{s,daily}$) from LST_{daily}. In the two-source energy balance (TSEB) framework, these temperatures at an instantaneous satellite overpass are related through the fractional vegetation cover observed at the sensor's view angle (Norman et al., 1995). However, because our analysis is based on daily averaged LST, which represents the hemispheric outgoing longwave temperature, we formulated this relationship using the daily longwave transmissivity (τ_L). Under the assumption of equal emissivity for canopy and soil surfaces, the daily mean radiometric temperature can be expressed as the sum of the outgoing longwave radiation from the two components:

$${LST_{daily}}^4 = (1 - \tau_L){T_{c,daily}}^4 + \tau_L {T_{s,daily}}^4 \quad (9a)$$

$$\tau_L = \exp(-\kappa_L LAI) \quad (9b)$$

where LAI is leaf area index, and κ_L is the extinction coefficient for longwave, setting 0.95, which is equivalent to the extinction coefficient for diffuse radiation (Kustas & Norman, 1999).

In Equations (9a) and (9b), both LST_{daily} and LAI can be derived from Landsat optical and thermal observations (details in sections 2.4.1 and 2.4.5). However, $T_{c,daily}$ and $T_{s,daily}$ remain unknown unless an additional constraint is introduced. To address this, we introduce a constraint derived from a simplified form of the ET_{DIF} (see Appendix C), which links canopy surface temperature to LST and air temperature. This additional constraint is expressed as follows:

$$T_{c,daily} = T_{a,daily} + \beta(LST_{daily} - T_{a,daily}) \quad (10a)$$

$$\beta = \frac{f_c}{f_c + \frac{\Delta + \gamma}{RH_a \Delta + \gamma}(1 - f_c)} \quad (10b)$$

$$f_c = 1 - \exp(-0.4LAI) \quad (10c)$$

where β is a parameter that controls the degree to which canopy surface temperature departs from *LST*, and f_c is the fraction of net radiation absorbed by the canopy, estimated as in Equation (10c) (Norman et al., 1995). The parameter β acts as a weighting factor that adjust canopy temperature. When β approaches 1, the canopy surface temperature remains close to *LST*. Conversely, when β approaches 0, the canopy surface temperature converges to the overlying air temperature.

We first estimate $T_{c,daily}$ using Equation (10a) and then substitute the result into Equation (9a) to obtain $T_{s,daily}$. However, the resulting $T_{s,daily}$ can occasionally become unrealistically high. To avoid this issue, we compute an upper bound for $T_{s,daily}$ by assuming that the net radiation at the soil surface cannot be negative:

$$\varepsilon\sigma T_{s,daily}{}^4 \leq \tau_S SW_n + \tau_L LW_{atm} + (1 - \tau_L)\varepsilon\sigma T_{c,daily}{}^4 \quad (11)$$

where τ_S is the daily shortwave transmissivity, SW_n is the daily net shortwave radiation (MJ m^{-2} d^{-1}) and LW_{atm} is incoming longwave radiation MJ m^{-2} d^{-1}.

If estimated $T_{s,daily}$ violates Inequality (11), we set $T_{s,daily}$ to its upper limit based on the right-hand side of Inequality (11).

3.4.3. Daily net radiation

We calculate broadband shortwave albedo from Landsat surface reflectance following Liang (2001). Assuming that the diurnal variation in albedo is negligible, the daily net shortwave radiation (SW_n) is estimated as:

$$SW_n = SW_{in}(1 - \alpha) \quad (12)$$

where SW_{in} is the gridMET daily incoming solar radiation (MJ m^{-2} d^{-1}), and α is the Landsat-derived broadband albedo.

The daily effective shortwave transmissivity is estimated using Beer's law as

$$\tau_S = \exp(-\kappa_S LAI) \quad (13)$$

where κ_S is the extinction coefficient for shortwave. We set $\kappa_S = 0.56$, based on a meta-analysis of canopy light extinction coefficients across diverse ecosystems (Zhang et al., 2014).

For incoming longwave radiation (LW_{atm}), we apply the ASCE PM formulation (Allen et al., 2005):

$$LW_{atm} = \varepsilon\left[1 - \left(1.35\frac{SW_{in}}{R_{so}} - 0.35\right)\left(0.34 - 0.14\sqrt{e_a}\right)\right]\sigma {T_{a,daily}}^4 \tag{14}$$

where R_{so} is calculated clear-sky radiation (MJ m^{-2} d^{-1}) based on the ASCE PM approach, and $T_{a,daily}$ is in Kelvin. It should be noted that, although the original ASCE PM method uses minimum and maximum air temperatures, we instead use the daily mean air temperature to maintain consistency with our definition of LW_{out} in Equation (8), where we use the daily mean LST.

Next, the net radiations at the canopy and soil are estimated as follows under the assumption of equal emissivity and albedo for both surfaces:

$$R_{nc} = (1 - \tau_S)SW_n + (1 - \tau_L)\left[LW_{atm} + \varepsilon\sigma {T_{s,daily}}^4 - 2\varepsilon\sigma {T_{c,daily}}^4\right] \tag{15a}$$

$$R_{ns} = \tau_S SW_n + \tau_L LW_{atm} + (1 - \tau_L)\varepsilon\sigma {T_{c,daily}}^4 - \varepsilon\sigma {T_{s,daily}}^4 \tag{15b}$$

$$R_n = R_{nc} + R_{ns} \tag{15c}$$

where R_n is net radiation (MJ m^{-2} d^{-1}).

In Figure S2, we present the evaluation of daily net radiation estimated from Landsat and gridMET data against in-situ observations from flux-tower sites. Overall, the performance of R_n estimation is lower than that of outgoing longwave radiation, likely due to uncertainties in the incoming radiations. Nevertheless, the results demonstrate that the proposed approach provides a reasonable and reliable estimation of daily net radiation.

3.4.4. Daily soil heat flux

Daytime soil heat flux is typically estimated as a fraction of the soil net radiation, while nighttime soil heat flux is generally negative due to heat release from the ground. Accordingly, we propose the following formulation to represent the daily mean soil heat flux (G, MJ m^{-2} d^{-1}):

$$G = 0.35R_{ns} - 1.5 \tag{16}$$

Here, the first term on the right-hand side of Equation (16) represents the daytime soil heat flux following Norman et al. (1995), while the second term accounts for upward nighttime soil heat flux from the subsurface. The magnitude of the second term is empirically set such that the median daily soil heat flux across all data is approximately zero.

3.4.5. Leaf Area Index

In this study, LAI is primarily estimated using the Landsat derived two-band Enhanced Vegetation Index (EVI2) (Jiang et al., 2008). This approach is adopted because empirical relationships based on EVI2 show better agreement with in situ LAI observations (Kang et al., 2016; Mourad et al., 2020), and EVI2-derived LAI has been successfully applied in satellite-based ET models (Jaafar et al., 2022). The formulation follows the empirical equation proposed by Kang et al. (2016)

$$LAI_{EVI2} = (2.92\sqrt{EVI_2} - 0.43)^2 \qquad (17)$$

where LAI_{EVI2} is EVI2 driven LAI, which is limited within [0,8] (Jaafar et al., 2022).

We found that, although this approach generally produces reasonable results, LAI estimates derived from vegetation indices exhibit limitations over green-painted roofs, which are artificially interpreted as having high LAI. To address this issue, we additionally employ the normalized difference moisture index (NDMI) proposed by Gao (1996). NDMI is computed from the difference between near-infrared (NIR) and shortwave-infrared (SWIR) reflectance and is sensitive to vegetation water content. Because artificial green surfaces typically exhibit negative NDMI values, we reduce LAI when NDMI becomes negative, as follows:

$$LAI = LAI_{EVI2} NDMI_{scaled} \qquad (18a)$$

$$NDMI_{scaled} = \frac{NDMI - NDMI_{min}}{0 - NDMI_{min}} \qquad (18b)$$

Here, $NDMI_{scaled}$ is constrained (clamped) within [0,1]. Based on the typical NDMI range, we set $NDMI_{min} = -0.3$. For actively transpiring vegetation, NDMI is generally positive, such that $NDMI_{scaled} = 1$ and *LAI* remains unchanged. In contrast, for artificial or non-vegetated green surfaces characterized by negative NDMI values, $NDMI_{scaled}$ decreases toward zero, thereby reducing spuriously high LAI estimates derived from vegetation indices.

3.4.6. Soil surface relative humidity

Soil surface relative humidity (RH_s) is estimated as follows:

$$RH_s = RH_a NDMI_{scaled} + \frac{e_a}{e^*(T_s)}(1 - NDMI_{scaled}) \qquad (19)$$

At the daily timescale, soil surface relative humidity is assumed to be close to air relative humidity, consistent with surface flux equilibrium theory (Kim et al., 2021; McColl et al., 2019). When NDMI is negative, as represented by reduced values of defined in Equation (18b), RH_s is adjusted toward a lower bound corresponding to dry soil surfaces. This lower bound is defined as the ratio of atmospheric water vapor pressure (e_a) to the saturation vapor pressure at the soil surface temperature $e^*(T_s)$.

The estimated RH_s from Equation (19) is applied to all land cover types, except open water, where RH_s is set to 1.

3.4.7. Conductive exchange coefficient

The effective conductive exchange coefficient ($\frac{k_g}{d_g}$, MJ m^{-2} K^{-1} d^{-1}) is used to estimate μ_s in Eq. (3b). Here, d_g is defined as the depth below which temperature is not directly influenced by aerodynamic exchange with the atmosphere at the daily time scale (details in Appendix B). Although this definition is physically intuitive, the corresponding soil storage length scale is difficult to derive rigorously from first principles, owing to the continuous nature of subsurface heat conduction and its dependence on soil thermal properties (Kim et al., 2023).

To constrain d_g in a physically consistent yet parsimonious manner, we adopt a steady-state force–restore framework (Bhumralkar, 1975), under which d_g can be interpreted as a damping depth associated with surface temperature forcing. Aerodynamic exchange induces relatively high-frequency variations in soil surface temperature, whose downward propagation is progressively attenuated by thermal conduction. Accordingly, the depth below which temperature is no longer directly influenced by aerodynamic forcing can be represented by a thermal damping depth at the daily time scale.

By introducing soil thermal inertia, the ratio of soil thermal conductivity to damping depth can be further simplified as follows (Huang & Wang, 2016):

$$\frac{k_g}{d_g} = I_s\sqrt{\frac{\omega}{2}}\frac{86400}{10^6} \tag{20}$$

Where I_s is the thermal inertia of the soil (J m^{-2} K^{-1} s$^{-1/2}$), and ω is the fundamental diurnal angular frequency ($\omega = 2\pi/86400\ s^{-1}$).

Typically, I_s lies within a relatively narrow range, on the order of 1000 J m^{-2} K^{-1} s$^{-1/2}$ (Bennett et al., 2008), with values around 800 for dry soils and up to 1500 for pure water (Huang & Wang, 2016). Sensitivity tests conducted over an I_s range of 800-1500 indicate only moderate impacts on the resulting ET estimates. Accordingly, we adopt a constant value of $I_s = 1000$ J m^{-2} K^{-1} s$^{-1/2}$ for parsimonious estimation.

3.4.8. Parameters for the aerodynamic term

The δ_{LC} parameter in Equation (4) is defined as follows:

$$\delta_{LC} = \begin{cases} 1, & LC \in \{\text{curtivated, open water, wetland, woody wetland with LAI<1}\} \\ 0, & LC \notin \{\text{curtivated, open water, wetland, woody wetland with LAI<1}\} \end{cases} \quad (21)$$

δ_{LC} is defined based on USGS NLCD land cover types where advective effects are likely to occur.

The δ_{wet} parameter in Equation (4) is defined as follows:

$$\delta_{WET} = f_c + f_{sm} f_{sT}(1 - f_c) \quad (22a)$$

$$f_{sm} = {RH_s}^{VPD_s} \quad (22b)$$

$$f_{sT} = \frac{1}{1 + e^{10 - LST_{soil}}} \quad (22c)$$

where f_{sm} and f_{sT} represent soil moisture and temperature constrain, respectively.

The parameter δ_{wet} increases with increasing vegetation cover represented by f_c. Because LAI is constrained using NDMI in Equation (18), which directly affects f_c, an increase in f_c reflects a larger fraction of actively transpiring vegetation. For non-vegetated surfaces (1-f_c), wetness is regulated independently through soil moisture and temperature constraints. Specifically, f_{sm} is estimated using soil surface relative humidity (RH_s) and vapor pressure deficit (VPD_s) following Fisher et al. (2008). Although f_{sm} effectively captures moisture limitation under most conditions, it tends to approach unity under cold conditions because RH_s is typically close to saturation at low temperatures. This behavior can lead to an overestimation of ET during winter. To mitigate this effect, we introduce the temperature constraint f_{sT}, defined as a sigmoidal function of soil surface temperature, which reduces δ_{wet} under cold conditions and suppresses unrealistically high wintertime ET.

For the wind function, we employed Penman's empirical wind function, which is widely used for the advection-aridity model (Comini de Andrade et al., 2025).

$$f(u) = 2.6(1 + 0.54u_2) \quad (23)$$

where u_2 is windspeed at 2m reference height (m s^{-1}).

3.4.9. Elevation effect

To account for the influence of topography on both air temperature and incoming solar radiation, elevation-based corrections were applied to the meteorological forcings used in RADET. Minimum and maximum air temperature fields from the gridMET dataset were first adjusted to the local terrain height following a dry adiabatic lapse rate of -6.5 K km^{-1}. For each gridMET pixel, the gridMET elevation was compared to the 30 m SRTM elevation (Farr et al., 2007), and the elevation difference was multiplied by the lapse rate to obtain the correction. The corrected minimum and maximum air temperature were used to estimate daily mean LST, T_c, T_s, incoming long wave radiation, and saturation vapor pressure and its slope (as detailed in previous sections).

In addition, the effect of terrain on surface shortwave radiation was incorporated to account for slope and aspect. Specifically, we applied the analytical, integrated formulations for daily solar radiation on sloping surfaces introduced by Allen et al. (2006). We estimated ratio of global radiation on a sloped surface to that on a horizontal surface by considering direct beam, diffuse, and reflected components. One minor deviation from Allen et al. (2006) is that we ignore differences in direct-beam transmissivity between sloped and horizontal surfaces.

These corrections ensure that both temperature and solar radiation forcings more accurately represent the micro-meteorological conditions over complex terrain. However, it should be noted that neighborhood shadowing from adjacent terrain features and the shading effect on local air temperature are not considered in this resampling procedure.

3.5. Temporal interpolation for monthly RADET

Since the RADET model directly estimates daily ET, it does not require temporal upscaling from instantaneous to daily ET as commonly needed in other remote sensing approaches. However, RADET outputs are available only on Landsat overpass days, which occur every 8 days when two satellites are available or every 16 days when only one satellite operates. The gap can be even longer when cloud cover prevents satellite observations. Therefore, a temporal interpolation is required to estimate monthly aggregated ET.

In OpenET, five of the six models interpolate daily EToF (the ratio between ET and ETo) using piecewise linear interpolation and then multiply by ETo to obtain daily ET. The ALEXI/DisALEXI models use a similar approach but replace ETo with incoming shortwave radiation. The ETo-based approach is suitable for advective conditions over wet surfaces such as cropland. However, at regional scales, ET and ETo often show opposite behavior due to the complementary relationship between ET and atmospheric demand (Bouchet, 1963). To address this, RADET applies the ALEXI/DisALEXI-style interpolation scheme, which uses the ratio between ET and incoming shortwave radiation. This approach has been shown to perform comparably to schemes based on ETo and other methods (Brutsaert & Sugita, 1992; Cammalleri et al., 2014).

We also tested other interpolation variables, including fractions of ETo, shortwave radiation, potential shortwave radiation, net radiation, and equilibrium ET (Alfieri et al., 2017). We found that the differences in interpolated daily ET were notable, but monthly aggregated ET showed only marginal differences because daily biases tended to cancel out when averaged over the month. For operational scalability, we use readily available incoming shortwave radiation to reduce computational cost, noting that the interpolation can be further optimized in future implementations.

4. Methods

4.1. RADET data inputs

Primary input to the RADET model, and relevant model parameters are summarized in Table 1. Specifically, the study period spans from 2000 to the end of 2020. During this period, we used Landsat 5,7, and 8 optical and thermal imagery (Wulder et al., 2019). Albedo, EVI2, and NDMI for each Landsat scene were computed on the Google Earth Engine (GEE) cloud platform (Gorelick et al., 2017). Required variables, including land surface temperature, emissivity, albedo, EVI2, and NDMI were then extracted from GEE by spatially averaging a 7×7 pixel window centered on each flux tower footprint. Further details on the flux footprint estimation are provided in Volk, Huntington, Melton, Allen, et al. (2023).

Meteorological variables at a daily scale were obtained from the gridMET dataset for each flux tower location (Abatzoglou, 2013). The required variables include specific humidity, minimum and maximum air temperature, surface downward shortwave radiation, and wind speed at 10 m height. Air pressure is also required to convert specific humidity to vapor pressure. However, since gridMET does not provide air pressure, it was estimated from SRTM elevation (Farr et al., 2007), following the ASCE PM formulation (Allen et al., 2005).

Land cover information was retrieved from the annually updated USGS NLCD dataset (US Geological Survey, 2024), accessed through the Awesome GEE Community Catalog (Roy et al., 2025). We extracted NLCD data from GEE for each flux tower site.

Table 1 Primary inputs to the RADET model.

Data (sources)	Native spatial resolution (temporal scale)	Primary usage
Land surface temperature (Landsat-5, 7 & 8)	60 – 120 m (instantaneous)	Canopy and soil surface temperature
Surface reflectance (Landsat-5, 7 & 8)	30 m (instantaneous)	Albedo, EVI2, and NDMI
Solar radiation, specific humidity, minimum and maximum air temperature, wind speed (gridMET)	4 km (daily average)	Meteorological forcing for the RADET model
Elevation (SRTM)	30m (constant)	Estimating air pressure, resampling air temperature and solar radiation
Land cover (USGS NLCD)	30 m (annually updated constant)	Identifying advective conditions

4.2. OpenET data

We used OpenET data (Melton et al., 2022) to compare the performance of the proposed RADET model against the six well-established OpenET models and their ensemble average. Specifically, we obtained time series data of OpenET estimates at both daily and monthly scales, extracted for the same flux tower locations and footprints (7×7-pixel windows) used in our analysis. This dataset was originally used for OpenET accuracy evaluation study (Volk et al., 2024). It should be noted that we download time series data for each site from the Zenodo repository (https://doi.org/10.5281/zenodo.10119477), which was used for the accuracy evaluation study.

4.3. MODIS based ET products

We further compared RADET with evapotranspiration products derived from the Moderate Resolution Imaging Spectroradiometer (MODIS), whose spatial resolution is coarse but whose temporal revisit frequency is high. Specifically, we used the MOD16 ET Collection 6.1 product, MOD16A2GF v6.1, (Running et al., 2021) and the PML-V2 v0.1.8 ET dataset (Zhang et al., 2019). Both datasets were extracted for the central pixel of each flux-tower footprint using GEE. The 8-day ET values were then converted to monthly values by distributing each composite period evenly across individual days and aggregating to calendar months.

A recent study by Endsley et al. (2025) introduced an updated and recalibrated version of MOD16. This updated version is expected to be released with MODIS Collection 7, but is not yet publicly available. We obtained the updated MOD16 product directly from the authors and note that the current implementation is processed using MODIS FPAR/LAI from Collection 6.1 (rather than Collection 7). To ensure consistency and avoid calibration bias, we adopt the same set of 61 flux-tower sites used by Endsley et al. (2025), excluding sites that were involved in MOD16 calibration or validation.

4.4. In-situ ET data

To evaluate the performance of the proposed RADET model, we used in situ flux measurements as a benchmark. Specifically, we employed the dataset compiled by Volk, Huntington, Melton, Minor, et al. (2023), which aggregates ET measurements across the conterminous United States from multiple sources, including AmeriFlux, USDA-ARS, and USGS NWSC. This dataset was used for OpenET performance assessment (Volk et al., 2024).

Most of the sites use the eddy covariance method, while a smaller number rely on Bowen ratio systems or weighing lysimeters. After excluding sites with fewer than five paired ET observations (daily RADET and in-situ ET overlaps) during the study period, 145 sites remained for analysis. These comprise 54 cropland, 16 evergreen forest, 27 grassland, 13 mixed forest, 26 shrubland, and 9 wetland/riparian sites (Figure 2).

The eddy covariance method is subject to a systematic uncertainty known as the energy balance imbalance, wherein the sum of turbulent heat fluxes is typically lower than the available energy (Mauder et al., 2020; Wilson et al., 2002). For model evaluation, we used both energy balance ratio (EBR)–corrected data (results presented in the main text) and EBR–uncorrected data (results provided in the Supplementary Information). The EBR correction was applied using the Bowen ratio preservation method (Twine et al., 2000; Volk, Huntington, Melton, Allen, et al., 2023).

For daily-scale performance assessments, we used quality-controlled, gap-free daily ET observations. Specifically, only satellite overpass days were considered, and gap-filled or negative in situ ET values were excluded. To ensure consistency with OpenET models, we included only paired records where RADET estimates, in situ ET observations, and OpenET values were all available for the same day.

For monthly-scale assessments, gap-filled in situ ET data were included. Specifically, monthly data were used only when the number of gap-filled days did not exceed five (Volk et al., 2024). While this strict criterion ensures consistent comparison with OpenET, it can exclude many records during rainy months, periods that typically exhibit high ET in water-limited ecosystems such as shrublands. Therefore, as a secondary monthly benchmark, we applied a relaxed criterion requiring at least five observed days per month. This benchmark was used solely to evaluate RADET performance, not for direct comparison with OpenET models.

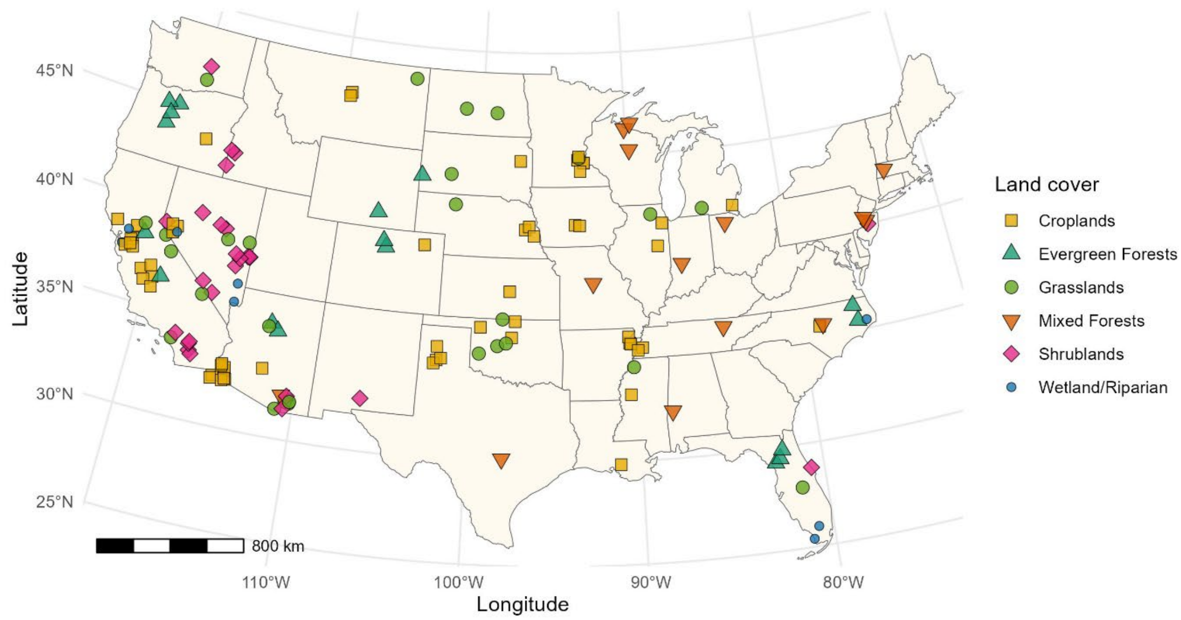

Figure 2 Map of in situ ET measurement sites. Point shapes indicate their land cover type. The exact site locations are slightly jittered to reduce overlap among closely spaced points.

4.5. Model evaluations

We evaluated the RADET model in a hierarchical manner. First, we compared the proposed ET formulation with the surface flux equilibrium model (McColl et al., 2019), to examine how the two-source implementation of the DIF constraint enhances ET estimation and how the inclusion of Penman's aerodynamic term further improves performance. Building on this theoretical comparison, we assessed the model's performance at both daily and monthly timescales using flux-tower observations. In particular, we compared RADET performance with the OpenET models and their ensemble to determine whether the proposed model improves medium-resolution ET estimation accuracy. Finally, we compared RADET with the operational MOD16 product.

We employed several statistical metrics, including Kling-Gupta Efficiency (KGE), Nash–Sutcliffe Efficiency (NSE), Root Mean Square Error (RMSE), Mean Absolute Error (MAE), and Mean Bias Error (MBE). In the one-to-one comparison plots between modeled and observed ET, we also present the coefficient of determination (R^2), calculated as the square of the Pearson correlation coefficient, along with the least-squares regression slope constrained through the origin.

To transparently evaluate model performance, we follow the OpenET accuracy assessment (Volk et al., 2024). Specifically, daily accuracy statistics were calculated without using any gap-filled station ET data, while monthly statistics included only stations with five or fewer gap-filled days per month. For land cover–based grouping of statistical metrics, we used the flux site metadata classification rather than the USGS NLCD.

For each flux station, RMSE, MAE, MBE, and NSE were computed individually and then aggregated using a weighted mean. To prevent a single site with extremely low KGE and NSE from disproportionately influencing the results, individual-site KGE and NSE values were constrained (clamped) within the range of [–1, 1]. KGE and NSE were calculated only for sites that had a minimum of five paired data points. Group-level statistics were weighted by the square root of the number of paired observations per station to balance the influence of stations, by preventing those with very long records from dominating the results while avoiding equal weighting of stations with short records (Volk et al., 2024).

For comparison with MOD16, we followed the approach of Endsley et al. (2025) to reproduce performance metrics consistent with their analysis. Specifically, we restricted the evaluation to the same 61 flux-tower sites used in their MOD16–OpenET intercomparison and did not compute site-specific metrics or apply site-level weighting. Instead, we grouped the records into cropland and non-cropland categories and computed performance statistics directly from the pooled paired observations, consistent with the methodology applied in Endsley et al. (2025).

5. Results

5.1. Theoretical evaluation of RADET

We first evaluated the performance of the proposed ET_{DIF} formulation (Equation 2) and the RADET model (Equation 4) at the daily timescale. To better understand how these formulations operate, we compared their performance with the surface flux equilibrium (SFE) model ($ET = \frac{1}{L_v}\frac{RH\Delta(R_n - G)}{RH\Delta + \gamma}$) using identical available-energy and meteorological inputs (Figure 3 for EBR-corrected evaluations and Figure S3 for EBR-uncorrected evaluations). The SFE model is a simple equilibrium-based ET formulation that relies solely on meteorological variables and available energy (McColl et al., 2019). Despite its simplicity, SFE often performs comparably to, or even better than, more complex satellite-based ET models (Thakur et al., 2025).

Figure 3 shows that ET_{DIF} outperforms the SFE model, even though the two share similarities in their formulations. The SFE model typically underestimates ET under high-ET conditions and overestimates ET when ET is low (Kim et al., 2023). ET_{DIF} effectively addresses these issues, particularly for land cover types where advection is not expected ($\delta_{LC} = 0$). This is because the μ terms reduce ET below equilibrium when LST exceeds air temperature, mitigating positive biases at low ET, while the two-source treatment increases ET with increasing vegetation cover, reflecting the higher equilibrium evaporative fraction of canopy relative to soil.

However, ET_{DIF} still exhibits substantial biases when $\delta_{LC} = 1$, where strong advection can violate the DIF hypothesis. This limitation is effectively resolved in RADET model, which builds on ET_{DIF} but conditionally incorporates Penman's aerodynamic term when advective enhancement is expected. This hierarchical improvement from the simple SFE model to ET_{DIF}, and finally to RADET, is consistent regardless of whether the in situ benchmark data are energy-balance-uncorrected (Figure S3). These findings together demonstrate the theoretical robustness of ET_{DIF} relative to the well-established SFE theory, as well as the clear advantage of incorporating aerodynamic term in the proposed RADET model.

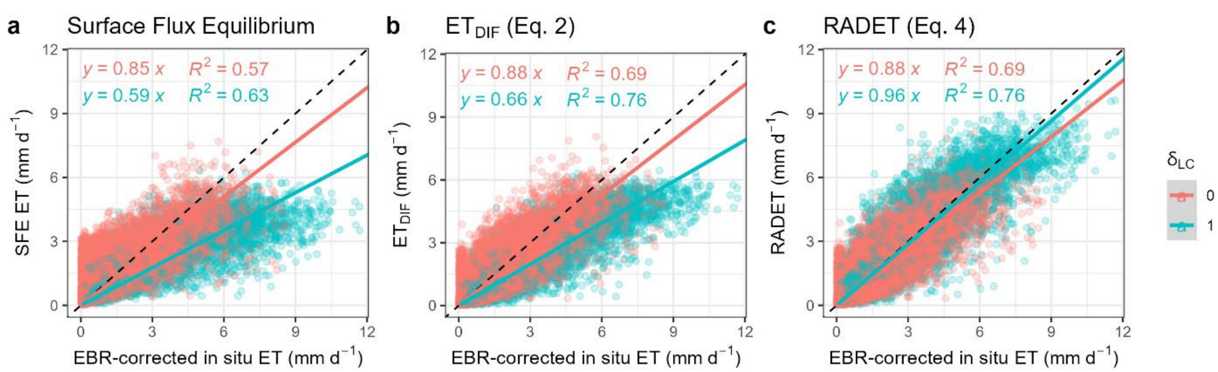

Figure 3 In situ ET observations versus estimated daily ET using the SFE (a), ET_{DIF} (b) and RADET (c) models. Observed ET represents energy balance ratio (EBR) corrected data. The dashed line indicates the 1:1 line, and point colors differentiate $\delta_{LC} = 0$ and $\delta_{LC} = 1$. R^2 and the least-squares linear regression forced through the origin are shown (solid line).

5.2. Daily RADET evaluation

We first evaluate the performance of the RADET model for satellite overpass days. Only paired data where both RADET estimates and in-situ ET observations are available were included in the analysis (see details in Method section). One-to-one comparisons between

RADET and in situ ET are presented in Figure 4 (EBR–corrected benchmark) and Figure S4 (EBR–uncorrected benchmark).

Across all land cover types, R^2 exceeded 0.62 and the regression slopes were slightly below unity when evaluated against the EBR-corrected benchmark. When using the EBR-uncorrected benchmark, R^2 values decreased modestly and the regression slopes generally exceeded unity, except for the Wetland/Riparian group. Performance is strongest over croplands and mixed forests (slopes of 0.96 and 0.97; R^2 = 0.76 and 0.80), consistent with OpenET models, which also perform well in these land covers (Volk et al., 2024). Evergreen forests, grasslands, and shrublands also show strong correspondence (slopes of 0.9–0.93; R^2 = 0.62–0.66), a notable result given that medium-resolution ET models often struggle over these ecosystems (Volk et al., 2024). Wetland/riparian sites retain relatively high explanatory power (R^2 = 0.68) but exhibit the lowest slope (0.79).

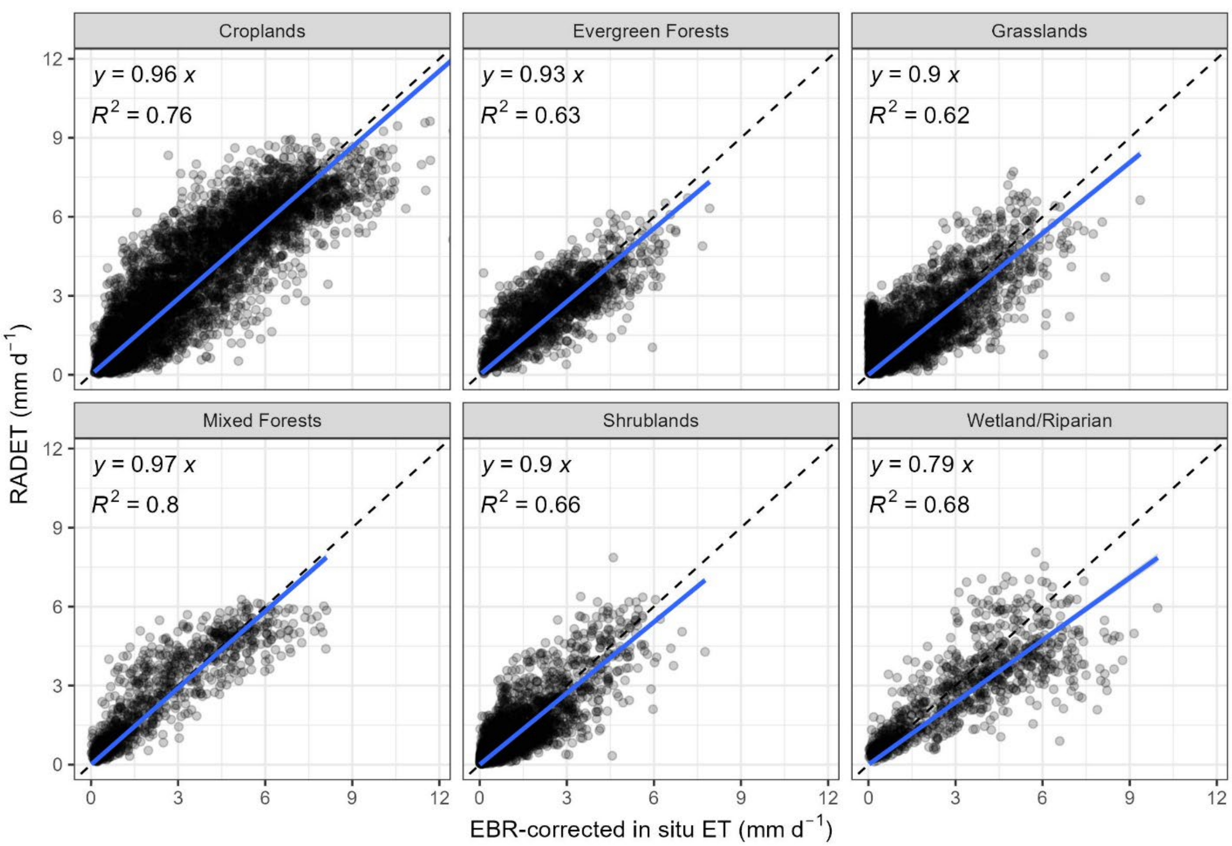

Figure 4 Daily RADET versus in-situ ET observations grouped by land cover type. Observed ET represents energy balance ratio corrected data. For each land cover group, R^2 and the least-squares linear regression forced through the origin are shown.

Next, we further compare the performance of RADET with the individual OpenET models and their ensemble mean. For the daily-scale analysis, the SIMS model from OpenET was excluded because it does not account for soil evaporation (Melton et al., 2022; Volk et al., 2024). Figure 5 summarizes the error statistics of RADET and OpenET models using EBR–corrected in situ ET as the benchmark, while Figure S5 presents the same statistics using EBR–uncorrected data. Overall, RADET outperforms or performs comparably to the OpenET models and their ensemble across all land cover types under both benchmarks.

In croplands, RADET shows similar performance to the best OpenET model when using the EBR–corrected benchmark. In particular, the negative bias commonly observed in OpenET models over croplands is substantially reduced by RADET. A further breakdown of cropland subtypes (Figure S6) shows that RADET performs particularly well in annual crops and orchards. In vineyards, however, RADET tends to overestimate in situ ET, whereas previous studies have reported that OpenET performs especially well in vineyards (Volk et al., 2024).

When the EBR–uncorrected benchmark is used, RADET's performance becomes similar to that of the OpenET models in croplands, primarily due to a larger positive bias. However, it is important to note that the eddy covariance technique does not capture horizontal advection (Mauder et al., 2020), which increase surface energy imbalance particularly over irrigated croplands and potentially introduce bias in in-situ ET when EBR correction is not applied (Volk, Huntington, Melton, Allen, et al., 2023).

For evergreen forests, mixed forests, grasslands, and shrublands, RADET consistently outperforms all OpenET models and their ensemble across statistical metrics. This result is consistent for both EBR–corrected and uncorrected benchmarks. Notably, substantial improvements were observed over evergreen forests and shrublands, where OpenET models exhibited negative NSE values (indicating performance lower than the observed mean), whereas RADET maintained positive NSE. Furthermore, OpenET models show a pronounced positive bias in evergreen forests, which has been linked to systematic overestimation of ET in forested watersheds in recent studies (Nassar et al., 2025). This bias is substantially reduced by the RADET model.

For the Wetland/Riparian group, RADET performs comparably to the OpenET models when evaluated against the EBR-corrected benchmark. The lack of a large performance improvement is primarily linked to RADET's negative bias in this group. As shown in Figure S6, RADET underestimates in-situ ET at most riparian sites, whereas this bias is not evident in wetland sites. This discrepancy arises because the advection term is not applied to riparian sites, which are not classified as wetlands in the USGS NLCD land cover dataset.

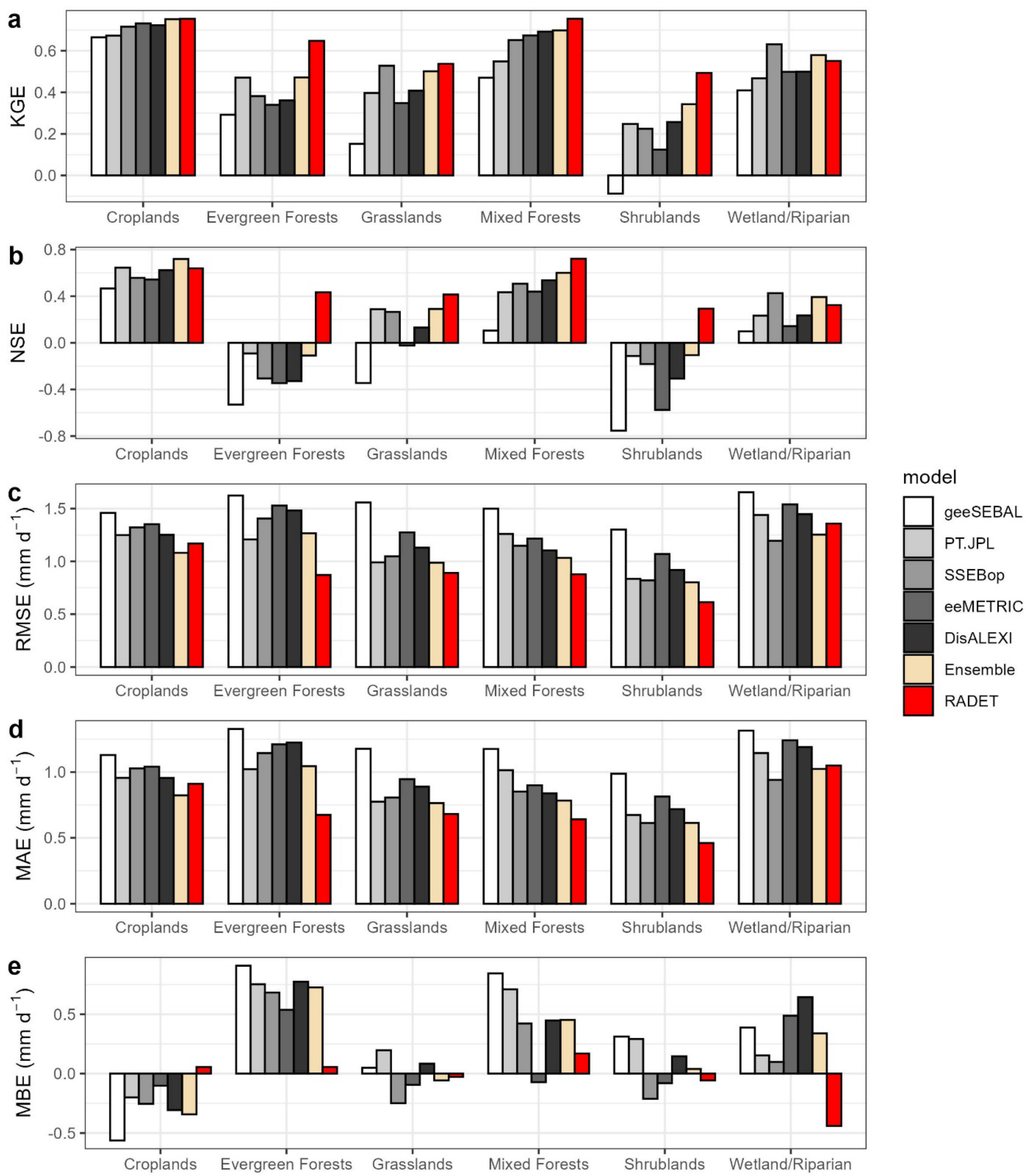

Figure 5 Comparison of daily error statistics between RADET and OpenET models, grouped by land cover type. Model evaluations were performed using EBR–corrected in situ ET as the benchmark.

As RADET showed improved performance particularly over evergreen forests and shrublands, we selected two representative Landsat scenes: one containing four in situ flux sites located in evergreen forests in Oregon (Figure 6), and another containing two shrubland sites and one grassland site in Nevada (Figure 7).

The evergreen forest scene (Landsat 8; July 26, 2024) covers an area near the Metolius River in Oregon (Figure 6). This region exhibits a pronounced gradient from evergreen forest to shrubland (left to right), with several forest-clearing patches on the western side of the scene and cropland patches near the river on the eastern side. The scene also includes four flux tower sites (US-Me1, US-Me2, US-Me5, US-Me6). Both RADET (Figure 6a) and the OpenET ensemble (Figure 6b) capture these land cover transitions at 30 m resolution, though the strength of the spatial contrast differs between the two. Specifically, OpenET generally produces higher ET than RADET over evergreen forests. In situ ET measurements from the four flux sites indicate that RADET agrees more closely with observations across this region (e.g., KGE = 0.65 for RADET vs. 0.32 for the OpenET ensemble; Figure S7a), primarily due to RADET reducing the positive bias present in the OpenET ensemble.

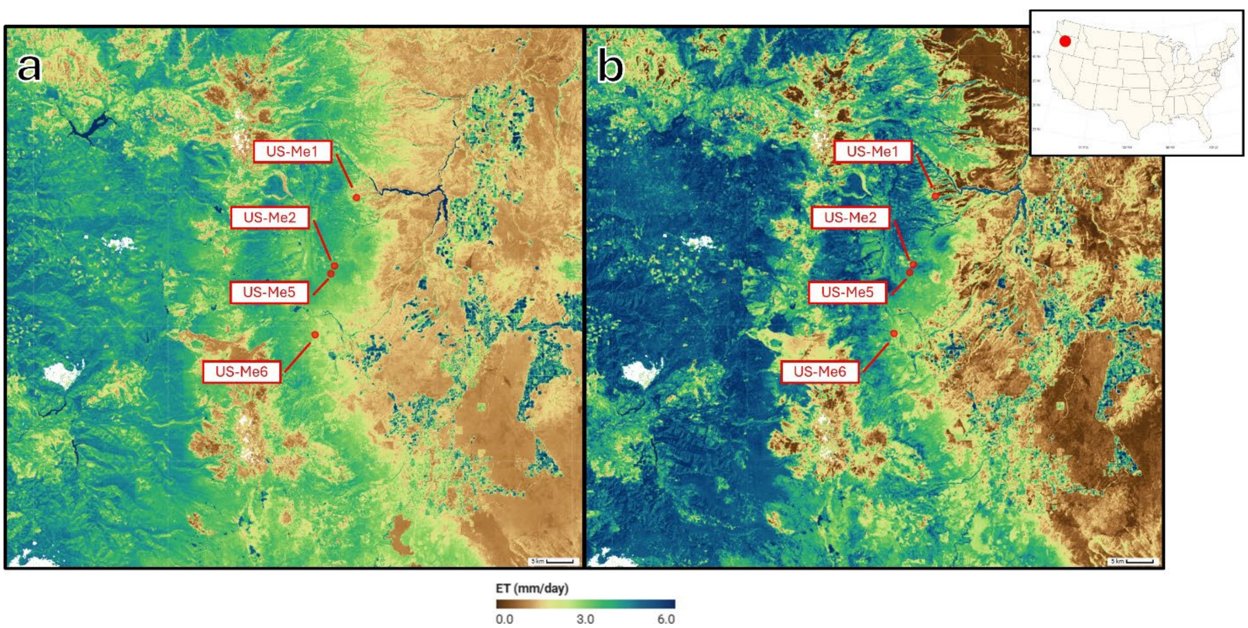

Figure 6 Comparison of daily ET between (a) RADET and (b) the OpenET ensemble for a single Landsat 8 scene acquired on July 26, 2024, over central Oregon near the Metolius River. The four red points mark flux tower sites located in evergreen forest: US-Me1, US-Me2, US-Me5, and US-Me6. The satellite image covers primarily evergreen forest (left) and shrubland (right), with several forest-clearing patches on the western side of the scene and croplands on the eastern side. White spots result from cloud masking.

The second scene (Landsat 8; July 14, 2023) covers a dry, semi-arid region of Spring Valley in eastern Nevada (Figure 7). The scene includes mountain ranges on the western and eastern sides and a broad valley in the center, where three flux tower sites are located (SV-5, SV-6, SPV-3). The valley is primarily classified as shrubland, with a few cropland patches. Across the extensive shrubland areas, the OpenET ensemble produces ET values that are close to zero, whereas RADET yields noticeably higher estimates. In situ ET observations from the three flux sites show that RADET substantially improves agreement with measurements by reducing the underestimation error of the OpenET ensemble (e.g., KGE = 0.71 for RADET vs. 0.43 for the OpenET ensemble; Figure S7b).

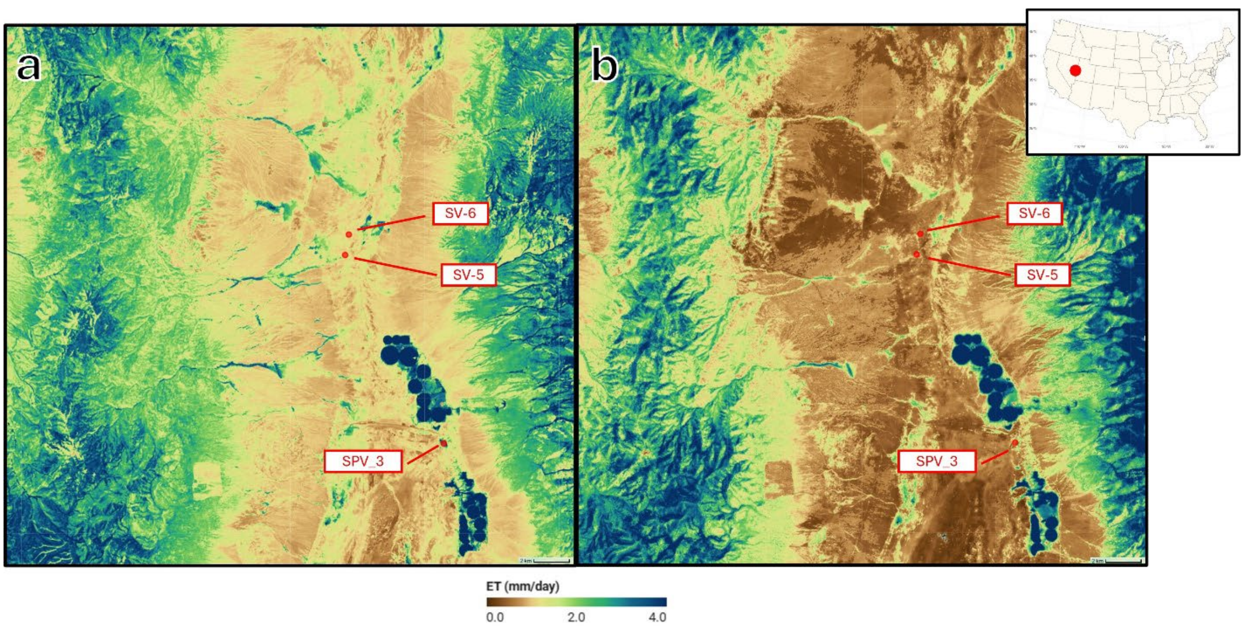

Figure 7 Comparison of daily ET between (a) RADET and (b) the OpenET ensemble for a single Landsat 8 scene acquired on July 14, 2023, over the Spring Valley in Nevada. The three red points mark flux tower sites located in shrublands: SV-5, SV-6, and a grassland: SPV_3. The satellite image covers primarily shrubland, with a few cropland areas in the right-bottom portion of the scene.

5.3. Monthly RADET evaluation

We evaluated the performance of the monthly RADET model using one-to-one comparisons between RADET estimates and in situ ET observations (Figure 8: EBR–corrected benchmark; Figure S8: EBR–uncorrected benchmark). In Figure 8, two benchmark criteria were applied: a strict quality-control criterion (≤ 5 gap-filled days) and a relaxed criterion (≥ 5 observed days). For the EBR–uncorrected comparison shown in Figure

S8, only the strict criterion was used, as the gap-filling scheme of (Volk, Huntington, Melton, Allen, et al., 2023) applies exclusively to EBR–corrected ET data.

For the EBR–corrected benchmark under the relaxed criterion, RADET achieved R^2 values exceeding 0.7 across all land cover types, with regression slopes close to unity. While croplands showed slightly improved performance under the strict criterion, some dry land covers, such as shrublands, exhibited the opposite pattern. In particular, shrubland R^2 decreased from 0.76 under the relaxed criterion to 0.68 under the strict criterion. This likely reflects the exclusion of high monthly ET values associated with precipitation events under the strict criterion, which were retained in the relaxed benchmark and well captured by RADET. The EBR–uncorrected benchmark showed comparable R^2 values but generally higher regression slopes.

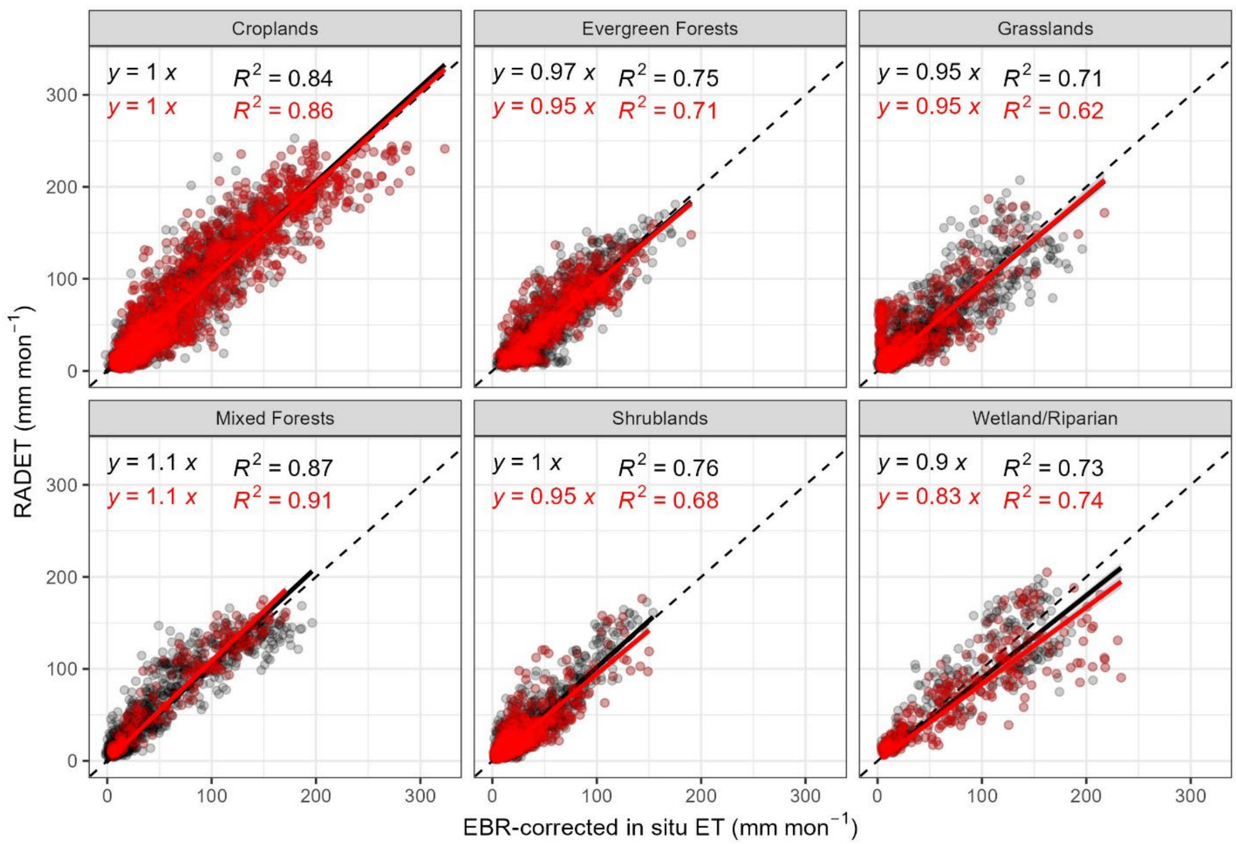

Figure 8 Monthly RADET versus in-situ ET observations grouped by land cover type. Observed ET represents EBR corrected data. Red points indicate results under the strict benchmark criterion (≤5 gap-filled days), while black points indicate the relaxed benchmark criterion (≥5 observed days). For each land cover group, R^2 and the least-squares linear regression forced through the origin are shown.

We then compared the performance of RADET with the individual OpenET models and their ensemble mean at the monthly scale. Figure 9 summarizes the error statistics of RADET and the OpenET models using EBR–corrected in situ ET as the benchmark, while Figure S9 presents the same statistics using EBR-uncorrected data. We also present one-to-one comparison plots of in-situ ET versus the individual OpenET models, the OpenET ensemble, and RADET in Figures S10–S15. Overall, RADET outperforms or performs comparably to the OpenET models and their ensemble across all land cover types under both benchmarks, consistent with the results at the daily scale.

For croplands, RADET performs similar to the best OpenET model under the EBR-corrected benchmark, but shows reduced performance with the EBR-uncorrected benchmark. As discussed in the daily-scale analysis, this difference reflects the large surface energy-balance closure errors that occur under advective conditions in irrigated croplands.

Across other land cover types, including evergreen forests, mixed forests, grasslands, and shrublands, RADET consistently shows the best performance for all statistical metrics, regardless of the benchmark dataset. Consistent with the daily-scale evaluation, notable improvements were observed for evergreen forests and shrublands. In shrublands, monthly NSE values were generally negative for all models, primarily because observed ET exhibits very low temporal variability, causing NSE to penalize even small absolute errors. Nevertheless, RADET still produces positive NSE values, indicating comparatively superior skill in capturing the subtle month-to-month variations in shrubland ET. When evaluated using EBR-uncorrected data, NSE values for the OpenET models remain mostly negative across all natural land cover types, whereas RADET maintains positive NSE.

To examine the spatial pattern of these improvements, Figure 10 illustrates the difference in KGE between the RADET model and the OpenET ensemble at the monthly scale. Although the OpenET ensemble is not necessarily the best model at every site, it generally performs better than individual models and thus provides a representative reference. The proposed RADET model generally performs better than the OpenET ensemble, with substantial improvements observed at sites located in natural ecosystems, whereas slight performance degradation is occasionally observed in croplands. Notably, RADET shows marked performance gains across the western United States.

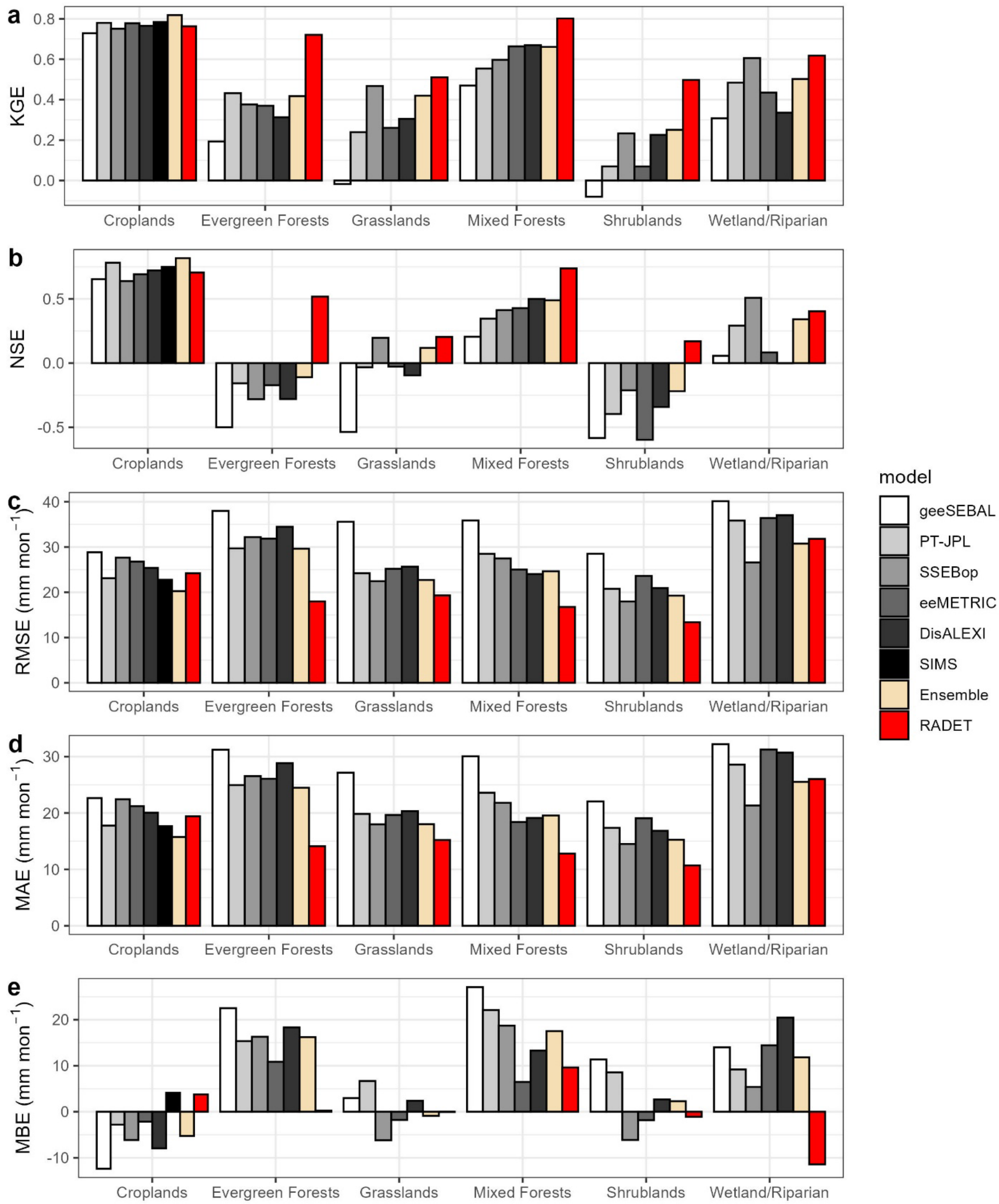

Figure 9 Comparison of monthly error statistics between RADET and OpenET models, grouped by land cover type. Model evaluations were performed using EBR–corrected in situ ET with strict QA criterion (≤5 gap-filled days) as the benchmark.

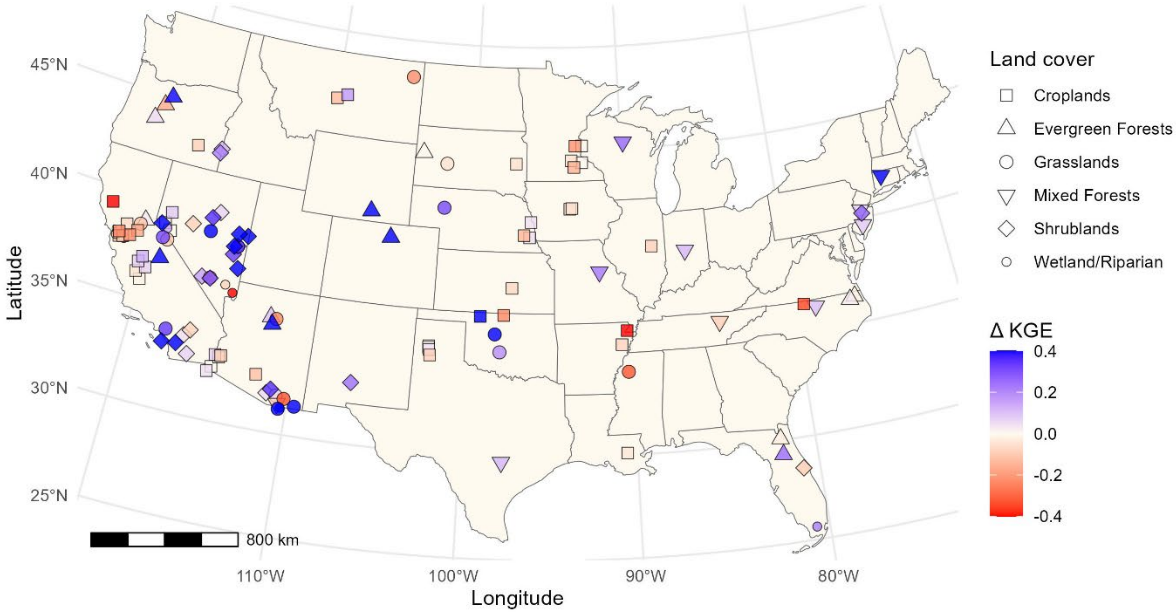

Figure 10 Spatial distribution of the difference in the Kling–Gupta Efficiency (KGE) between the RADET model and the OpenET ensemble at the monthly scale. Blue indicates improvement, whereas red indicates degradation in RADET performance relative to the OpenET ensemble. Absolute KGE differences greater than 0.4 were limited to ±0.4 to constrain the color range. Point shapes denote land cover types. Exact site locations were slightly jittered to reduce overlap among closely spaced points.

5.4. Intercomparison with MODIS-based models

We evaluated the monthly performance of RADET against the PML-V2 product, the current operational MOD16 Collection 6.1 ET product, and the recently updated MOD16 version (expected for release in MODIS Collection 7) (Table 2). Following the MOD16–OpenET intercomparison framework of Endsley et al. (2025), we used the same set of 61 flux-tower sites (none of which are used for parameter calibration in MOD16) and computed performance metrics directly from pooled cropland and non-cropland records, without applying site-level weighting or aggregation. It is worth noting that our reproduction of the Endsley et al. (2025) statistics showed minor discrepancies, likely due to differences in data filtering arising from the inclusion of additional ET products (e.g., RADET and PML-V2).

Among the MODIS-based products, PML-V2 and the updated MOD16 version both performed substantially better than the current operational MOD16 Collection 6.1 for croplands as well as non-croplands. This pattern is consistent with previous studies reporting improved skill in PML-V2 and the updated MOD16 relative to the current MOD16 Collection 6.1 (Endsley et al., 2025; Zhang et al., 2019). Despite these improvements in the recent MODIS products, RADET still demonstrated superior performance. Over croplands, RADET outperformed all MODIS-based products by a wide margin, and over non-cropland sites RADET exhibited either clearly better or at least comparable performance relative to the more advanced MODIS products.

Table 2 Performance metrics for monthly RADET, the PML-V2 product, the current MOD16 Collection 6.1 (C6.1), and the updated MOD16 version expected to be released with Collection 7 (C7). Metrics are calculated using the 61 flux-tower sites following Endsley et al. (2025). Performance is summarized separately for croplands and for all non-cropland sites.

	Model	RMSE (mm mon^{-1})	MBE (mm mon^{-1})	Correlation	KGE
Croplands	RADET	25.2	+4.2	0.93	0.87
	OpenET Ensemble	19.1	-6.9	0.96	0.90
	PML-V2	36.0	-16.2	0.86	0.53
	C6.1 MOD16	51.6	-29.9	0.76	-0.08
	C7 MOD16	34.2	-13.0	0.86	0.61
Non-crop	RADET	19.0	+4.3	0.92	0.84
	OpenET Ensemble	28.2	+8.7	0.84	0.70
	PML-V2	24.2	-0.52	0.84	0.84
	C6.1 MOD16	26.3	-8.23	0.81	0.68
	C7 MOD16	24.6	+3.1	0.83	0.81

6. Discussion

6.1. As simple as possible, but not simpler

The proposed RADET model is substantially simpler than many surface energy balance models used for satellite-based ET estimation. Because RADET is grounded in the equilibrium framework implied by the DIF hypothesis (Raupach, 2001), it does not require aerodynamic conductance or surface conductance parameterizations. These parameters typically rely on semi-empirical formulations, land cover-specific calibration, and canopy-height-dependent coefficients, and they are a major source of uncertainty in satellite-based ET estimation (Mallick et al., 2022; Polhamus et al., 2013; Trebs et al., 2021). By avoiding this dependency through a distinct theoretical assumption, RADET retains a compact analytical form without any site-specific calibration. The computational cost is also low, because the model does not require the iterative solution of the surface energy balance used in TSEB-type models (Anderson et al., 2012; Anderson et al., 2007; Norman et al., 1995), nor the simultaneous iterative solving of aerodynamic and surface conductances as in the STIC model (Mallick et al., 2014).

Thus, RADET remains simple but not at the expense of essential processes. Its two-source formulation informed by optical remote sensing, the radiatively coupled equilibrium solution derived from thermal remote sensing, and the conditional incorporation of Penman's aerodynamic term under advective conditions collectively distinguish it from simpler SFE-based approaches (Figure 3). Together, these components allow RADET to capture the key drivers of ET variability, make effective use of satellite-derived information, and achieve strong performance across diverse land cover types.

6.2. Overcoming spatial-temporal resolution constraints

Remote sensing–based ET estimation involves a well-known trade-off between spatial resolution and revisit frequency. Medium-resolution sensors (10–100 m; e.g., Landsat, Sentinel-2) provide the spatial detail, whereas moderate-resolution sensors (250 m–1 km; e.g., MODIS, VIIRS) offer more frequent observations but at the cost of spatial aggregation. Because irrigated croplands typically exhibit strong contrasts with adjacent non-irrigated areas, medium-resolution thermal and optical data are especially effective at capturing field-level heterogeneity (Radeloff et al., 2024). As a result, medium-resolution energy-balance models consistently outperform coarse-resolution products in croplands (Endsley et al., 2025).

In contrast, moderate-resolution ET models generally perform well over spatially homogeneous natural ecosystems, where ET is driven by large-scale canopy and atmospheric controls rather than subfield variability (Chen & Liu, 2020). Their higher revisit frequency allows them to capture day-to-day variability and reduces temporal sampling errors, providing an advantage in forests, grasslands, and shrublands when surface conditions vary smoothly in space.

The performance of RADET challenges this conventional expectation. Despite relying solely on Landsat, with revisit intervals of 8 days (or 16 days when only one satellite is operational), RADET produces ET estimates that (i) match the performance of the best OpenET models in croplands, and (ii) exceed the accuracy of state-of-the-art MODIS-based products across natural ecosystems at monthly timescales. This is notable because RADET operates with far fewer temporal observations, whereas MODIS-based products benefit from near-continuous temporal coverage. The results demonstrate that accurate representation of key physical processes, rather than temporal density of observations alone, can substantially improve ET estimates even in natural ecosystems.

Moreover, higher spatial resolution offers important advantages beyond croplands. Medium-resolution ET allows detection of fine-scale disturbances, characterization of heterogeneous or patchy vegetation, delineation of small watershed boundaries, and improved representation of riparian corridors and land-use edges (e.g., Figures 6 and 7). These benefits can only be realized if the medium-resolution ET itself is reliable across diverse land cover types (Radeloff et al., 2024). RADET provides this capability by delivering high-accuracy ET at 30-m resolution across both agricultural and natural landscapes, thereby opening new opportunities for water-resources applications that require spatial detail, high accuracy, and physical realism.

6.3. Room for Improvement

Although RADET demonstrates a robust theoretical foundation and strong performance across diverse land cover types, several limitations warrant further investigation and refinement.

First, the current implementation relies on land cover classification and NDMI to determine whether advective conditions are present, thereby dictating when Penman's aerodynamic term should be activated. This rule-based approach performed reasonably well overall but showed limitations in specific contexts. For instance, several riparian sites were not labeled as wetlands in the NLCD database, resulting in the aerodynamic term not being applied and leading to ET underestimation (Figure S6). Conversely, RADET tended to overestimate ET at vineyard sites, likely because deficit irrigation reduces ET (Volk et al., 2024), while the model assumes strong advection based on crop type alone (Figure S6). Future work could improve this component by (i) incorporating irrigation-status information (e.g., Ketchum et al., 2020), (ii) explicitly identifying riparian zones (e.g., Albano et al., 2020), or (iii) developing a physically based indicator of local advection derived from thermal imagery (e.g., spatial temperature gradients or relative pixel coolness).

Second, because RADET relies on Landsat's relatively infrequent revisit interval, monthly ET estimation requires temporal interpolation. Although we tested several interpolation strategies (e.g., based on shortwave radiation or reference ET) and found only modest differences among them, the interpolation step remains a key component of the workflow. This is especially important for extending RADET to periods before 2000, when only a single Landsat satellite was available. A more rigorous evaluation, such as a theoretical assessment of temporal sampling error and testing interpolation approaches grounded in physical models (Riba et al., 2025), could further improve RADET's accuracy on days without satellite observations.

Third, RADET has thus far been evaluated only within CONUS. Applying the model across broader climatic and ecological gradients is an important next step. In particular, its performance in tropical forests, with and without advective enhancement, remains uncertain, as does its behavior on islands or coastal environments where oceanic humidity transport may violate the DIF assumptions. Extending RADET to global settings will require testing across diverse biomes, assessing its validity under conditions of both strong and weak advection, and identifying where model structural refinements are needed.

6.4. Future applications

This study demonstrates the operational potential of RADET by showing that the model achieves high accuracy with a relatively simple formulation and minimal computational cost. Preliminary benchmark tests on Google Earth Engine indicate that the computational demand of RADET is similar to models in OpenET that require low computation, such as SIMS and PTJPL. By providing a Python processing pipeline that follows the structure of the current OpenET code and makes use of OpenET core functions, RADET has clear potential for wider applications beyond the present study area. For instance, the model can be applied to regions in other parts of the world or used to generate operational ET products through open-source workflows.

Although RADET is demonstrated here with Landsat data, the formulation is not limited to a specific sensor and can be extended to satellites with different spatial, spectral, and temporal characteristics. Integrating RADET with the Harmonized Landsat and Sentinel product, similar to the HSEB approach described by Jaafar et al. (2022), would maintain medium spatial resolution while greatly improving revisit frequency. Applying RADET to missions with finer thermal resolution such as ECOSTRESS or Hydrosat also represents a promising direction. These extensions are expected to further improve ET estimation, especially considering that RADET already shows strong performance using only Landsat observations.

In practical terms, RADET can be used not only to investigate agricultural water use but also to estimate water yield, groundwater recharge, and overall water availability. These applications are possible because RADET provides high spatial detail and small bias across a wide range of land cover types. For example, RADET shows substantial improvements around the Great Basin (Figure 10), highlighting its potential for regional water-availability assessments. To support such uses, future studies should include water balance evaluations to assess RADET from a practical and hydrologic perspective. Advancing RADET toward broader real-world application will require exploring how to make the best use of its strengths, which include high spatial detail and consistently high accuracy across many environments, capabilities not previously achieved by other ET models based on satellite data.

7. Conclusion

Medium resolution remote sensing for ET estimation has advanced rapidly, and several practical products have emerged in recent years. However, as highlighted by Radeloff et al. (2024), a major remaining challenge is the need for ET estimates that remain reliable across all land cover types. Conventional approaches generally do not meet this requirement. This study introduces RADET, a medium resolution ET model designed to address this gap by providing accurate ET estimates across diverse environments.

RADET is grounded in an equilibrium theory and applies an aerodynamic term only when the equilibrium assumption is expected to be violated. The model demonstrates superior accuracy compared with existing medium resolution models that rely on Landsat data and with moderate resolution products based on MODIS that benefit from more frequent revisit intervals. This performance is achieved without any land cover specific calibration and without the iterative computations that are common in many surface energy balance models and that require substantial computational resources.

Several directions remain for future work. These include addressing known limitations of the model, extending RADET beyond the CONUS, applying the formulation to additional satellite sensors, and generating fully operational products. At the same time, future studies should explore the practical advantages of RADET. By providing consistently accurate evapotranspiration estimates at fine spatial resolution, RADET enables forms of analysis that are not feasible with existing models, including improved water resources assessment and management. Advancing RADET toward broader real-world application will require efforts to fully utilize this capability and to demonstrate the value of high resolution and physically transparent evapotranspiration estimation in practice.

Author contributions: CRediT

Yeonuk Kim: Conceptualization, Data curation, Formal analysis, Investigation, Methodology, Validation, Visualization, Writing-original draft; **Justin L Huntington**: Conceptualization, Funding acquisition, Methodology, Investigation, Resources, Supervision, Writing-review & editing; **Bruno Comini de Andrade:** Data curation, Formal analysis, Investigation, Methodology, Software, Writing-review & editing; **Mark S Johnson:** Conceptualization, Methodology, Supervision, Writing-review & editing; **John M Volk**: Data curation, Investigation, Writing-review & editing; **Sayantan Majumdar**: Investigation, Writing-review & editing; **Charles Morton:** Data curation, Software, Writing-review & editing; **Peter ReVelle**: Investigation, Writing-review & editing

Declaration of competing interest

The authors declare that they have no known competing financial interests or personal relationships that could have appeared to influence the work reported in this paper.

Data availability

The open-source Python implementation of the RADET model will be released in a subsequent version of the preprint, expected around the time we submit the manuscript to a journal in February 2026. All input data used for RADET are publicly available through the Google Earth Engine Data Catalog (https://developers.google.com/earth-engine/datasets/catalog) or the Awesome GEE Community Catalog (https://gee-community-catalog.org/). The resulting RADET data for the flux-tower site locations are available at https://doi.org/10.5281/zenodo.18225226. The post-processed in situ flux data are available at https://zenodo.org/record/7636781. OpenET data extracted for the flux-tower site locations are available at https://doi.org/10.5281/zenodo.10119477. MODIS-based evapotranspiration data are available through the Google Earth Engine Data Catalog or upon request (for the updated MOD16 product provided by Arthur Endsley).

Acknowledgements

We express our thanks to the data providers including in-situ site investigators and technicians. We also thank Maosheng Zhao and Arthur Endsley for sharing the updated MOD16 data. This work was supported by the Maki Postdoctoral Fellowship (Desert Research Institute Maki Endowment), and U.S. Geological Survey Water Resources Research Institute, OpenET Planning Phase II (Grant G22AC00584-00).

References

Abatzoglou, J. T. (2013). Development of gridded surface meteorological data for ecological applications and modelling. *International Journal of Climatology*, *33*(1), 121-131. https://doi.org/10.1002/joc.3413

Albano, C. M., McGwire, K. C., Hausner, M. B., McEvoy, D. J., Morton, C. G., & Huntington, J. L. (2020). Drought Sensitivity and Trends of Riparian Vegetation Vigor in Nevada, USA (1985–2018). *Remote Sensing*, *12*(9), 1362. https://www.mdpi.com/2072-4292/12/9/1362

Alfieri, J. G., Anderson, M. C., Kustas, W. P., & Cammalleri, C. (2017). Effect of the revisit interval and temporal upscaling methods on the accuracy of remotely sensed evapotranspiration estimates. *Hydrology and Earth System Sciences*, *21*(1), 83-98. https://doi.org/10.5194/hess-21-83-2017

Allen, R. G., Tasumi, M., & Trezza, R. (2007). Satellite-Based Energy Balance for Mapping Evapotranspiration with Internalized Calibration (METRIC)—Model. *Journal of Irrigation and Drainage Engineering*, *133*(4), 380-394. https://doi.org/10.1061/(asce)0733-9437(2007)133:4(380)

Allen, R. G., Trezza, R., & Tasumi, M. (2006). Analytical integrated functions for daily solar radiation on slopes. *Agricultural and Forest Meteorology*, *139*(1), 55-73. https://doi.org/10.1016/j.agrformet.2006.05.012

Allen, R. G., Walter, I. A., Elliott, R., Howell, T. A., Itenfisu, D., & Jensen, M. E. (2005). *The ASCE standardized reference evapotranspiration equation* American Society of Civil Engineers, Reston, VA.

Anderson, M. C., Kustas, W. P., Alfieri, J. G., Gao, F., Hain, C., Prueger, J. H., Evett, S., Colaizzi, P., Howell, T., & Chávez, J. L. (2012). Mapping daily evapotranspiration at Landsat spatial scales during the BEAREX'08 field campaign. *Advances in Water Resources*, *50*, 162-177. https://doi.org/10.1016/j.advwatres.2012.06.005

Anderson, M. C., Norman, J. M., Mecikalski, J. R., Otkin, J. A., & Kustas, W. P. (2007). A climatological study of evapotranspiration and moisture stress across the continental United States based on thermal remote sensing: 1. Model formulation. *Journal of Geophysical Research: Atmospheres*, *112*(D10). https://doi.org/10.1029/2006JD007506

Bastiaanssen, W. G. M., Menenti, M., Feddes, R. A., & Holtslag, A. A. M. (1998). A remote sensing surface energy balance algorithm for land (SEBAL). 1. Formulation. *Journal of Hydrology*, *212-213*, 198-212. https://doi.org/10.1016/S0022-1694(98)00253-4

Beer, C., Ciais, P., Reichstein, M., Baldocchi, D., Law, B. E., Papale, D., Soussana, J.-F., Ammann, C., Buchmann, N., Frank, D., Gianelle, D., Janssens, I. A., Knohl, A., Köstner, B., Moors, E., Roupsard, O., Verbeeck, H., Vesala, T., Williams, C. A., & Wohlfahrt, G. (2009). Temporal and among-site variability of inherent water use efficiency at the ecosystem level. *Global Biogeochemical Cycles*, *23*(2). https://doi.org/10.1029/2008gb003233

Bennett, W. B., Wang, J., & Bras, R. L. (2008). Estimation of Global Ground Heat Flux. *Journal of Hydrometeorology*, *9*(4), 744-759. https://doi.org/10.1175/2008JHM940.1

Bhumralkar, C. M. (1975). Numerical experiments on the computation of ground surface temperature in an atmospheric general circulation model. *Journal of Applied Meteorology and Climatology*, *14*, 1246–1258. https://doi.org/10.1175/1520-0450(1975)014%3C1246:NEOTCO%3E2.0.CO;2

Bouchet, R. J. (1963). Evapotranspiration réelle et potentielle, signification climatique. *Int. Assoc. Sci. Hydro. Pub.*, *62*, 134-142.

Brutsaert, W., & Stricker, H. (1979). An advection-aridity approach to estimate actual regional evapotranspiration. *Water Resources Research*, *15*(2), 443-450. https://doi.org/10.1029/WR015i002p00443

Brutsaert, W., & Sugita, M. (1992). Application of self-preservation in the diurnal evolution of the surface energy budget to determine daily evaporation. *Journal of Geophysical Research: Atmospheres*, *97*(D17), 18377-18382. https://doi.org/10.1029/92JD00255

Cammalleri, C., Anderson, M. C., & Kustas, W. P. (2014). Upscaling of evapotranspiration fluxes from instantaneous to daytime scales for thermal remote sensing applications. *Hydrology and Earth System Sciences*, *18*(5), 1885-1894. https://doi.org/10.5194/hess-18-1885-2014

Chen, J. M., & Liu, J. (2020). Evolution of evapotranspiration models using thermal and shortwave remote sensing data. *Remote Sensing of Environment*, *237*, 111594. https://doi.org/10.1016/j.rse.2019.111594

Comini de Andrade, B., Huntington, J., Volk, J. M., Morton, C., Pearson, C., & Albano, C. M. (2025). Multi-Model Intercomparison of the Complementary Relationship of Evaporation Across Global Environmental Settings. *Water Resources Research*, *61*(9), e2024WR039740. https://doi.org/10.1029/2024WR039740

Crago, R., & Brutsaert, W. (1996). Daytime evaporation and the self-preservation of the evaporative fraction and the Bowen ratio. *Journal of Hydrology*, *178*(1), 241-255. https://doi.org/10.1016/0022-1694(95)02803-X

Davarzani, H., Smits, K., Tolene, R. M., & Illangasekare, T. (2014). Study of the effect of wind speed on evaporation from soil through integrated modeling of the atmospheric boundary layer and shallow subsurface. *Water Resources Research*, *50*(1), 661-680. https://doi.org/10.1002/2013WR013952

de Bruin, H. A. R., Trigo, I. F., Bosveld, F. C., & Meirink, J. F. (2016). A Thermodynamically Based Model for Actual Evapotranspiration of an Extensive Grass Field Close to FAO Reference, Suitable for Remote Sensing Application. *Journal of Hydrometeorology*, *17*(5), 1373-1382. https://doi.org/10.1175/jhm-d-15-0006.1

Endsley, K. A., Zhao, M., Kimball, J. S., Albrethsen, T., & Devadiga, S. (2025). Improved Global Estimates of Terrestrial Evapotranspiration Using the MODIS and VIIRS Sensors. *Journal of Hydrometeorology*, *26*(6), 817-833. https://doi.org/10.1175/jhm-d-24-0145.1

Farr, T. G., Rosen, P. A., Caro, E., Crippen, R., Duren, R., Hensley, S., Kobrick, M., Paller, M., Rodriguez, E., Roth, L., Seal, D., Shaffer, S., Shimada, J., Umland, J., Werner, M., Oskin, M., Burbank, D., & Alsdorf, D. (2007). The Shuttle Radar Topography Mission. *Reviews of Geophysics*, *45*(2). https://doi.org/10.1029/2005RG000183

Fisher, J. B., Lee, B., Purdy, A. J., Halverson, G. H., Dohlen, M. B., Cawse-Nicholson, K., Wang, A., Anderson, R. G., Aragon, B., Arain, M. A., Baldocchi, D. D., Baker, J. M., Barral, H., Bernacchi, C. J., Bernhofer, C., Biraud, S. C., Bohrer, G., Brunsell, N., Cappelaere, B.,...Hook, S. (2020). ECOSTRESS: NASA's Next Generation Mission to Measure Evapotranspiration From the International Space Station. *Water Resources Research*, *56*(4), e2019WR026058. https://doi.org/10.1029/2019wr026058

Fisher, J. B., Melton, F., Middleton, E., Hain, C., Anderson, M., Allen, R., McCabe, M. F., Hook, S., Baldocchi, D., Townsend, P. A., Kilic, A., Tu, K., Miralles, D. D., Perret, J., Lagouarde, J.-P., Waliser, D., Purdy, A. J., French, A., Schimel, D.,...Wood, E. F. (2017). The future of evapotranspiration: Global requirements for ecosystem functioning, carbon and climate feedbacks, agricultural management, and water resources. *Water Resources Research*, *53*(4), 2618-2626. https://doi.org/10.1002/2016WR020175

Fisher, J. B., Tu, K. P., & Baldocchi, D. D. (2008). Global estimates of the land–atmosphere water flux based on monthly AVHRR and ISLSCP-II data, validated at 16 FLUXNET sites. *Remote Sensing of Environment*, *112*(3), 901-919. https://doi.org/10.1016/j.rse.2007.06.025

Gao, B.-c. (1996). NDWI—A normalized difference water index for remote sensing of vegetation liquid water from space. *Remote Sensing of Environment*, *58*(3), 257-266. https://doi.org/10.1016/S0034-4257(96)00067-3

Gentine, P., Entekhabi, D., & Polcher, J. (2011). The diurnal behavior of evaporative fraction in the soil–vegetation–atmospheric boundary layer continuum. *Journal of Hydrometeorology*, *12*(6), 1530-1546. https://doi.org/10.1175/2011jhm1261.1

Gentine, P., Green, J. K., Guérin, M., Humphrey, V., Seneviratne, S. I., Zhang, Y., & Zhou, S. (2019). Coupling between the terrestrial carbon and water cycles—a review. *Environmental Research Letters*, *14*(8), 083003. https://doi.org/10.1088/1748-9326/ab22d6

Good, E. J. (2016). An in situ-based analysis of the relationship between land surface “skin” and screen-level air temperatures. *Journal of Geophysical Research: Atmospheres*, *121*(15), 8801-8819. https://doi.org/10.1002/2016JD025318

Gorelick, N., Hancher, M., Dixon, M., Ilyushchenko, S., Thau, D., & Moore, R. (2017). Google Earth Engine: Planetary-scale geospatial analysis for everyone. *Remote Sensing of Environment*, *202*, 18-27. https://doi.org/10.1016/j.rse.2017.06.031

Göttsche, F.-M., & Olesen, F. S. (2001). Modelling of diurnal cycles of brightness temperature extracted from METEOSAT data. *Remote Sensing of Environment*, *76*(3), 337-348. https://doi.org/10.1016/S0034-4257(00)00214-5

Huang, S.-Y., & Wang, J. (2016). A coupled force-restore model of surface temperature and soil moisture using the maximum entropy production model of heat fluxes. *Journal of Geophysical Research: Atmospheres*, *121*(13), 7528-7547. https://doi.org/10.1002/2015JD024586

Huntington, J., Minor, B., Bromley, M., Pearson, C., Beamer, J., Ingwersen, K., Carrara, K., Atkin, J., Brito, J., Morton, C., Dunkerly, C., Volk, J., Ott, T., ReVelle, P., Fellows, A., & Hoskinson, M. (2025). Crop evapotranspiration, consumptive use, and open water evaporation for Oregon. *Desert Research Institute Report*, *41306*. https://doi.org/10.82269/DRI-DHS-41306

Jaafar, H., Mourad, R., & Schull, M. (2022). A global 30-m ET model (HSEB) using harmonized Landsat and Sentinel-2, MODIS and VIIRS: Comparison to ECOSTRESS ET and LST. *Remote Sensing of Environment*, *274*, 112995. https://doi.org/10.1016/j.rse.2022.112995

Jiang, Z., Huete, A. R., Didan, K., & Miura, T. (2008). Development of a two-band enhanced vegetation index without a blue band. *Remote Sensing of Environment*, *112*(10), 3833-3845. https://doi.org/https://doi.org/10.1016/j.rse.2008.06.006

Jung, M., Koirala, S., Weber, U., Ichii, K., Gans, F., Camps-Valls, G., Papale, D., Schwalm, C., Tramontana, G., & Reichstein, M. (2019). The FLUXCOM ensemble of global land-atmosphere energy fluxes. *Scientific Data*, *6*(1), 74. https://doi.org/10.1038/s41597-019-0076-8

Kang, Y., Özdoğan, M., Zipper, S. C., Román, M. O., Walker, J., Hong, S. Y., Marshall, M., Magliulo, V., Moreno, J., Alonso, L., Miyata, A., Kimball, B., & Loheide, S. P. (2016). How Universal Is the Relationship between Remotely Sensed Vegetation Indices and Crop Leaf Area Index? A Global Assessment. *Remote Sensing*, *8*(7), 597. https://www.mdpi.com/2072-4292/8/7/597

Katul, G. G., Oren, R., Manzoni, S., Higgins, C., & Parlange, M. B. (2012). Evapotranspiration: A process driving mass transport and energy exchange in the soil-plant-atmosphere-climate system. *Reviews of Geophysics*, *50*(3). https://doi.org/10.1029/2011rg000366

Keenan, T. F., Hollinger, D. Y., Bohrer, G., Dragoni, D., Munger, J. W., Schmid, H. P., & Richardson, A. D. (2013). Increase in forest water-use efficiency as atmospheric carbon dioxide concentrations rise. *Nature*, *499*(7458), 324-327.

Ketchum, D., Jencso, K., Maneta, M. P., Melton, F., Jones, M. O., & Huntington, J. (2020). IrrMapper: A Machine Learning Approach for High Resolution Mapping of Irrigated Agriculture Across the Western U.S. *Remote Sensing*, *12*(14), 2328. https://www.mdpi.com/2072-4292/12/14/2328

Khand, K., Senay, G. B., Friedrichs, M., Yi, K., Fisher, J. B., Wang, L., Suvočarev, K., Ahmadi, A., Chu, H., Good, S., Mallick, K., Missik, J., Nelson, J. A., Reed, D. E., Wang, T., & Xiao, X. (2025). A novel approach to increase accuracy in remotely sensed evapotranspiration through basin water balance and flux tower constraints. *Journal of Hydrology*, *662*, 133824. https://doi.org/10.1016/j.jhydrol.2025.133824

Kim, Y., Garcia, M., Black, T. A., & Johnson, M. (2023). Assessing the complementary role of surface flux equilibrium (SFE) theory and maximum entropy production (MEP) principle in the estimation of actual evapotranspiration. *Journal of Advances in Modeling Earth Systems*, *15*(7), e2022MS003224. https://doi.org/10.1029/2022MS003224

Kim, Y., Garcia, M., Morillas, L., Weber, U., Black, T. A., & Johnson, M. S. (2021). Relative humidity gradients as a key constraint on terrestrial water and energy fluxes. *Hydrology and Earth System Sciences*, *25*(9), 5175-5191. https://doi.org/10.5194/hess-25-5175-2021

Kumar, B., Götzfried, P., Suresh, N., Schumacher, J., & Shaw, R. A. (2018). Scale Dependence of Cloud Microphysical Response to Turbulent Entrainment and

Mixing. *Journal of Advances in Modeling Earth Systems*, *10*(11), 2777-2785. https://doi.org/https://doi.org/10.1029/2018MS001487

Kumar, S., Imen, S., Sridharan, V. K., Gupta, A., McDonald, W., Ramirez-Avila, J. J., Abdul-Aziz, O. I., Talchabhadel, R., Gao, H., Quinn, N. W. T., Weiss, W. J., Poulose, T., Palmate, S. S., Lee, C. M., & Baskaran, L. (2024). Perceived barriers and advances in integrating earth observations with water resources modeling. *Remote Sensing Applications: Society and Environment*, *33*, 101119. https://doi.org/10.1016/j.rsase.2023.101119

Kustas, W. P., & Norman, J. M. (1999). Evaluation of soil and vegetation heat flux predictions using a simple two-source model with radiometric temperatures for partial canopy cover. *Agricultural and Forest Meteorology*, *94*(1), 13-29. https://doi.org/https://doi.org/10.1016/S0168-1923(99)00005-2

Liang, S. (2001). Narrowband to broadband conversions of land surface albedo I: Algorithms. *Remote Sensing of Environment*, *76*(2), 213-238. https://doi.org/https://doi.org/10.1016/S0034-4257(00)00205-4

Lindroth, A., Mölder, M., & Lagergren, F. (2010). Heat storage in forest biomass improves energy balance closure. *Biogeosciences*, *7*(1), 301-313. https://doi.org/10.5194/bg-7-301-2010

Liu, Y., Hiyama, T., Yasunari, T., & Tanaka, H. (2012). A nonparametric approach to estimating terrestrial evaporation: Validation in eddy covariance sites. *Agricultural and Forest Meteorology*, *157*, 49-59. https://doi.org/https://doi.org/10.1016/j.agrformet.2012.01.012

Liu, Z. (2021). The accuracy of temporal upscaling of instantaneous evapotranspiration to daily values with seven upscaling methods. *Hydrology and Earth System Sciences*, *25*(8), 4417-4433. https://doi.org/10.5194/hess-25-4417-2021

Loveland, T. R., Anderson, M. C., Huntington, J. L., Irons, J. R., Johnson, D. M., Rocchio, L. E., Woodcock, C. E., & Wulder, M. A. (2022). Seeing our planet anew: fifty years of landsat. *Photogrammetric Engineering & Remote Sensing*, *88*(7), 429-436.

Mallick, K., Baldocchi, D., Jarvis, A., Hu, T., Trebs, I., Sulis, M., Bhattarai, N., Bossung, C., Eid, Y., Cleverly, J., Beringer, J., Woodgate, W., Silberstein, R., Hinko-Najera, N., Meyer, W. S., Ghent, D., Szantoi, Z., Boulet, G., & Kustas, W. P. (2022). Insights Into the Aerodynamic Versus Radiometric Surface Temperature Debate in Thermal-Based Evaporation Modeling. *Geophysical Research Letters*, *49*(15), e2021GL097568. https://doi.org/https://doi.org/10.1029/2021GL097568

Mallick, K., Jarvis, A. J., Boegh, E., Fisher, J. B., Drewry, D. T., Tu, K. P., Hook, S. J., Hulley, G., Ardö, J., Beringer, J., Arain, A., & Niyogi, D. (2014). A Surface Temperature Initiated Closure (STIC) for surface energy balance fluxes. *Remote Sensing of Environment*, *141*, 243-261. https://doi.org/10.1016/j.rse.2013.10.022

Martin, D. J., Niswonger, R. G., Regan, R. S., Huntington, J. L., Ott, T., Morton, C., Senay, G. B., Friedrichs, M., Melton, F. S., Haynes, J., Henson, W., Read, A., Xie, Y., Lark, T., & Rush, M. (2025). Estimating irrigation consumptive use for the conterminous United States: coupling satellite-sourced estimates of actual evapotranspiration with a national hydrologic model. *Journal of Hydrology*, *662*, 133909. https://doi.org/10.1016/j.jhydrol.2025.133909

Martin, P. (1989). The significance of radiative coupling between vegetation and the atmosphere. *Agricultural and Forest Meteorology*, *49*(1), 45-53. https://doi.org/10.1016/0168-1923(89)90061-0

Mauder, M., Foken, T., & Cuxart, J. (2020). Surface-Energy-Balance Closure over Land: A Review. *Boundary-Layer Meteorology*, *177*(2-3), 395-426. https://doi.org/10.1007/s10546-020-00529-6

McCabe, M. F., & Wood, E. F. (2006). Scale influences on the remote estimation of evapotranspiration using multiple satellite sensors. *Remote Sensing of Environment*, *105*(4), 271-285. https://doi.org/https://doi.org/10.1016/j.rse.2006.07.006

McColl, K. A., & Rigden, A. J. (2020). Emergent Simplicity of Continental Evapotranspiration. *Geophysical Research Letters*, *47*(6), e2020GL087101. https://doi.org/10.1029/2020gl087101

McColl, K. A., Salvucci, G. D., & Gentine, P. (2019). Surface flux equilibrium theory explains an empirical estimate of water-limited daily evapotranspiration. *Journal of Advances in Modeling Earth Systems*, *11*(7), 2036-2049. https://doi.org/10.1029/2019ms001685

McNaughton, K. G. (1976). Evaporation and advection I: evaporation from extensive homogeneous surfaces. *Quarterly Journal of the Royal Meteorological Society*, *102*(431), 181-191. https://doi.org/10.1002/qj.49710243115

Melton, F. S., Huntington, J., Grimm, R., Herring, J., Hall, M., Rollison, D., Erickson, T., Allen, R., Anderson, M., Fisher, J. B., Kilic, A., Senay, G. B., Volk, J., Hain, C., Johnson, L., Ruhoff, A., Blankenau, P., Bromley, M., Carrara, W.,...Anderson, R. G. (2022). OpenET: Filling a Critical Data Gap in Water Management for the Western United States. *JAWRA Journal of the American Water Resources Association*, *58*(6), 971-994. https://doi.org/10.1111/1752-1688.12956

Melton, F. S., Johnson, L. F., Lund, C. P., Pierce, L. L., Michaelis, A. R., Hiatt, S. H., Guzman, A., Adhikari, D. D., Purdy, A. J., Rosevelt, C., Votava, P., Trout, T. J., Temesgen, B., Frame, K., Sheffner, E. J., & Nemani, R. R. (2012). Satellite Irrigation Management Support With the Terrestrial Observation and Prediction System: A Framework for Integration of Satellite and Surface Observations to Support Improvements in Agricultural Water Resource Management. *IEEE Journal of Selected Topics in Applied Earth Observations and Remote Sensing*, *5*(6), 1709-1721. https://doi.org/10.1109/JSTARS.2012.2214474

Miralles, D. G., Bonte, O., Koppa, A., Baez-Villanueva, O. M., Tronquo, E., Zhong, F., Beck, H. E., Hulsman, P., Dorigo, W., Verhoest, N. E. C., & Haghdoost, S. (2025). GLEAM4: global land evaporation and soil moisture dataset at 0.1° resolution from 1980 to near present. *Scientific Data*, *12*(1), 416. https://doi.org/10.1038/s41597-025-04610-y

Monteith, J. L. (1965). Evaporation and environment. Symposia of the society for experimental biology,

Monteith, J. L. (1981). Evaporation and surface temperature. *Quarterly Journal of the Royal Meteorological Society*, *107*(451), 1-27. https://doi.org/10.1002/qj.49710745102

Morton, F. I. (1969). Potential Evaporation as a Manifestation of Regional Evaporation. *Water Resources Research*, *5*(6), 1244-1255. https://doi.org/10.1029/WR005i006p01244

Mourad, R., Jaafar, H., Anderson, M., & Gao, F. (2020). Assessment of Leaf Area Index Models Using Harmonized Landsat and Sentinel-2 Surface Reflectance Data over a Semi-Arid Irrigated Landscape. *Remote Sensing*, *12*(19), 3121. https://www.mdpi.com/2072-4292/12/19/3121

Mu, Q., Zhao, M., & Running, S. W. (2011). Improvements to a MODIS global terrestrial evapotranspiration algorithm. *Remote Sensing of Environment*, *115*(8), 1781-1800. https://doi.org/10.1016/j.rse.2011.02.019

Nassar, A., Tarboton, D., Anderson, M., Yang, Y., Fisher, J. B., Purdy, A. J., Baig, F., He, C., Gochis, D., Melton, F., & Volk, J. (2025). Intercomparison of the U.S. National Water Model with OpenET over the Bear River Basin, U.S. *Journal of Hydrology*, *656*, 132826. https://doi.org/10.1016/j.jhydrol.2025.132826

Norman, J. M., Kustas, W. P., & Humes, K. S. (1995). Source approach for estimating soil and vegetation energy fluxes in observations of directional radiometric surface temperature. *Agricultural and Forest Meteorology*, *77*(3), 263-293. https://doi.org/https://doi.org/10.1016/0168-1923(95)02265-Y

Oki, T., & Kanae, S. (2006). Global hydrological cycles and world water resources. *Science*, *313*(5790), 1068-1072. https://doi.org/10.1126/science.1128845

Ott, T. J., Majumdar, S., Huntington, J. L., Pearson, C., Bromley, M., Minor, B. A., ReVelle, P., Morton, C. G., Sueki, S., Beamer, J. P., & Jasoni, R. L. (2024). Toward field-scale groundwater pumping and improved groundwater management using remote sensing and climate data. *Agricultural Water Management*, *302*, 109000. https://doi.org/10.1016/j.agwat.2024.109000

Pan, X., Yang, Z., Liu, Y., Yuan, J., Wang, Z., Liu, S., & Yang, Y. (2024). A non-parametric method combined with surface flux equilibrium for estimating terrestrial evapotranspiration: Validation at eddy covariance sites. *Journal of Hydrology*, *631*, 130682. https://doi.org/10.1016/j.jhydrol.2024.130682

Pearson, C., Minor, B., Morton, C., Volk, J., Dunkerly, C., Jensen, E., ReVelle, P., Kilic, A., Allen, R., & Huntington, J. L. (2024). Historical evapotranspiration and consumptive use of irrigated areas of the Upper Colorado River Basin. *Desert Research Institute Report No. 41304, prepared for the U.S. Bureau of Reclamation*. https://doi.org/10.13140/RG.2.2.31069.63206

Penman, H. L. (1948). Natural evaporation from open water, bare soil and grass. *Proceedings of the Royal Society of London. Series A. Mathematical and Physical Sciences*, *193*(1032), 120-145.

Pierrat, Z. A., Purdy, A. J., Halverson, G., Fisher, J. B., Mallick, K., Pascolini-Campbell, M., Ryu, Y., Anderson, M. C., Villanueva-Weeks, C., Johnson, M. C., Hatch, B., Davis, E., Yang, Y., & Cawse-Nicholson, K. (2025). Evaluation of ECOSTRESS Collection 2 Evapotranspiration Products: Strengths and Uncertainties for Evapotranspiration Modeling. *Water Resources Research*, *61*(6), e2024WR039404. https://doi.org/10.1029/2024WR039404

Polhamus, A., Fisher, J. B., & Tu, K. P. (2013). What controls the error structure in evapotranspiration models? *Agricultural and Forest Meteorology*, *169*, 12-24. https://doi.org/10.1016/j.agrformet.2012.10.002

Priestley, C. H. B., & Taylor, R. J. (1972). On the assessment of surface heat flux and evaporation using large-scale parameters. *Monthly Weather Review*, *100*(2), 81-92. https://doi.org/10.1175/1520-0493(1972)100<0081:otaosh>2.3.co;2

Radeloff, V. C., Roy, D. P., Wulder, M. A., Anderson, M., Cook, B., Crawford, C. J., Friedl, M., Gao, F., Gorelick, N., Hansen, M., Healey, S., Hostert, P., Hulley, G., Huntington, J. L., Johnson, D. M., Neigh, C., Lyapustin, A., Lymburner, L., Pahlevan, N.,...Zhu, Z. (2024). Need and vision for global medium-resolution Landsat and Sentinel-2 data products. *Remote Sensing of Environment*, *300*, 113918. https://doi.org/10.1016/j.rse.2023.113918

Rana, G., & Katerji, N. (2000). Measurement and estimation of actual evapotranspiration in the field under Mediterranean climate: a review. *European Journal of Agronomy*, *13*(2), 125-153. https://doi.org/10.1016/S1161-0301(00)00070-8

Raupach, M. R. (2001). Combination theory and equilibrium evaporation. *Quarterly Journal of the Royal Meteorological Society*, *127*(574), 1149-1181. https://doi.org/10.1002/qj.49712757402

Reitz, M., Volk, J. M., Ott, T., Anderson, M., Senay, G. B., Melton, F., Kilic, A., Allen, R., Fisher, J. B., Ruhoff, A., Purdy, A. J., & Huntington, J. (2025). Performance Mapping and Weighting for the Evapotranspiration Models of the OpenET Ensemble. *Water Resources Research*, *61*(8), e2024WR038899. https://doi.org/10.1029/2024WR038899

Riba, A., Garcia, M., Tarquís, A. M., Domingo, F., Antala, M., Feng, S., Liu, J., Johnson, M. S., Kim, Y., & Wang, S. (2025). Integrating Remotely Sensed Thermal Observations for Calibration of Process-Based Land-Surface Models: Accuracy, Revisit Windows, and Implications in a Dryland Ecosystem. *Remote Sensing*, *17*(21), 3630. https://doi.org/10.3390/rs17213630

Romera, D., & Silver, S. (2025). Technical Memorandum: Method for Determining Consumptive Use on Irrigated Acreage in the Lower Rio Grande, New Mexico. *Appendix C to the Groundwater Settlement Agreement between the United States and the State of New Mexico, Attachment B to Joint Motion to Dismiss, Texas v. New Mexico, No. 141, Original. U.S. Supreme Court*.

Roy, S., Jensen, E., Majumdar, S., & Saah, A. (2025). samapriya/awesome-gee-community-datasets: Community Catalog (3.8.0). In: Zenodo.

Running, S., Mu, Q., Zhao, M., & Moreno, A. (2021). *ODIS/Terra Net Evapotranspiration Gap-Filled 8-Day L4 Global 500m SIN Grid V061* (https://doi.org/10.5067/MODIS/MOD16A2GF.061

Salvucci, G. D., & Gentine, P. (2013). Emergent relation between surface vapor conductance and relative humidity profiles yields evaporation rates from weather data. *Proceedings of the National Academy of Sciences*, *110*(16), 6287-6291. https://doi.org/10.1073/pnas.1215844110

Seitzinger, S. P., Chuvieco, E., Di Giuseppe, F., Bombelli, A., Cagnazzo, C., Harris, S., & Tapper, N. (2026). Relevance of earth observations of essential climate variables in wildfire adaptation. *Remote Sensing of Environment*, *332*, 115082. https://doi.org/https://doi.org/10.1016/j.rse.2025.115082

Senay, G. B. (2018). Satellite Psychrometric Formulation of the Operational Simplified Surface Energy Balance (SSEBop) Model for Quantifying and Mapping Evapotranspiration. *Applied Engineering in Agriculture*, *34*(3), 555-566. https://doi.org/10.13031/aea.12614

Senay, G. B., Bohms, S., Singh, R. K., Gowda, P. H., Velpuri, N. M., Alemu, H., & Verdin, J. P. (2013). Operational Evapotranspiration Mapping Using Remote Sensing and Weather Datasets: A New Parameterization for the SSEB Approach. *JAWRA Journal of the American Water Resources Association*, *49*(3), 577-591. https://doi.org/10.1111/jawr.12057

Slatyer, R. O., & McIlroy, I. C. (1961). Practical microclimatology, with special reference to the water factor in soil-plant atmosphere relationships. *Practical microclimatology, with special reference to the water factor in soil-plant atmosphere relationships*.

Thakur, H., Raghav, P., Kumar, M., & Wolkeba, F. (2025). Surface Flux Equilibrium Theory-Derived Evapotranspiration Estimate Outperforms ECOSTRESS, MODIS, and SSEBop Products. *Geophysical Research Letters*, *52*(10), e2025GL114822. https://doi.org/10.1029/2025GL114822

Trebs, I., Mallick, K., Bhattarai, N., Sulis, M., Cleverly, J., Woodgate, W., Silberstein, R., Hinko-Najera, N., Beringer, J., Meyer, W. S., Su, Z., & Boulet, G. (2021). The role of aerodynamic resistance in thermal remote sensing-based evapotranspiration models. *Remote Sensing of Environment*, *264*, 112602. https://doi.org/10.1016/j.rse.2021.112602

Twine, T. E., Kustas, W. P., Norman, J. M., Cook, D. R., Houser, P. R., Meyers, T. P., Prueger, J. H., Starks, P. J., & Wesely, M. L. (2000). Correcting eddy-covariance flux underestimates over a grassland. *Agricultural and Forest Meteorology*, *103*(3), 279-300. https://doi.org/10.1016/S0168-1923(00)00123-4

US Geological Survey. (2024). Annual National Land Cover Database (NLCD) Collection 1 Products: U.S. Geological Survey data release. https://doi.org/10.5066/P94UXNTS

Volk, J. M., Huntington, J., Melton, F. S., Allen, R., Anderson, M. C., Fisher, J. B., Kilic, A., Senay, G., Halverson, G., Knipper, K., Minor, B., Pearson, C., Wang, T., Yang, Y., Evett, S., French, A. N., Jasoni, R., & Kustas, W. (2023). Development of a Benchmark Eddy Flux Evapotranspiration Dataset for Evaluation of Satellite-Driven Evapotranspiration Models Over the CONUS. *Agricultural and Forest Meteorology*, *331*, 109307. https://doi.org/10.1016/j.agrformet.2023.109307

Volk, J. M., Huntington, J. L., Melton, F., Minor, B., Wang, T., Anapalli, S., Anderson, R. G., Evett, S., French, A., Jasoni, R., Bambach, N., Kustas, W. P., Alfieri, J., Prueger, J., Hipps, L., McKee, L., Castro, S. J., Alsina, M. M., McElrone, A. J.,...Anderson, M. (2023). Post-processed data and graphical tools for a CONUS-wide eddy flux evapotranspiration dataset. *Data in Brief*, *48*, 109274. https://doi.org/10.1016/j.dib.2023.109274

Volk, J. M., Huntington, J. L., Melton, F. S., Allen, R., Anderson, M., Fisher, J. B., Kilic, A., Ruhoff, A., Senay, G. B., Minor, B., Morton, C., Ott, T., Johnson, L., Comini de Andrade, B., Carrara, W., Doherty, C. T., Dunkerly, C., Friedrichs, M., Guzman, A.,...Yang, Y. (2024). Assessing the accuracy of OpenET satellite-based evapotranspiration data to support water resource and land management applications. *Nature Water*, *2*(2), 193-205. https://doi.org/10.1038/s44221-023-00181-7

Wang, K., & Dickinson, R. E. (2012). A review of global terrestrial evapotranspiration: Observation, modeling, climatology, and climatic variability. *Reviews of Geophysics*, *50*(2). https://doi.org/10.1029/2011RG000373

Wilson, K., Goldstein, A., Falge, E., Aubinet, M., Baldocchi, D., Berbigier, P., Bernhofer, C., Ceulemans, R., Dolman, H., Field, C., Grelle, A., Ibrom, A., Law, B. E., Kowalski, A., Meyers, T., Moncrieff, J., Monson, R., Oechel, W., Tenhunen, J.,...Verma, S. (2002). Energy balance closure at FLUXNET sites. *Agricultural and Forest Meteorology*, *113*(1), 223-243. https://doi.org/10.1016/S0168-1923(02)00109-0

Wobus, C., Nash, C., Culp, P., Kelly, M., & Kennedy, K. (2025). Simplified agricultural water use accounting in the Colorado River Basin using OpenET. *Environmental Research Letters*, *20*(1), 014020. https://doi.org/10.1088/1748-9326/ad984b

Wulder, M. A., Loveland, T. R., Roy, D. P., Crawford, C. J., Masek, J. G., Woodcock, C. E., Allen, R. G., Anderson, M. C., Belward, A. S., Cohen, W. B., Dwyer, J., Erb, A., Gao, F., Griffiths, P., Helder, D., Hermosilla, T., Hipple, J. D., Hostert, P., Hughes, M. J.,...Zhu, Z. (2019). Current status of Landsat program, science, and applications. *Remote Sensing of Environment*, *225*, 127-147. https://doi.org/https://doi.org/10.1016/j.rse.2019.02.015

Zhang, L., Hu, Z., Fan, J., Zhou, D., & Tang, F. (2014). A meta-analysis of the canopy light extinction coefficient in terrestrial ecosystems. *Frontiers of Earth Science*, *8*(4), 599-609. https://doi.org/10.1007/s11707-014-0446-7

Zhang, Y., Kong, D., Gan, R., Chiew, F. H. S., McVicar, T. R., Zhang, Q., & Yang, Y. (2019). Coupled estimation of 500 m and 8-day resolution global evapotranspiration and gross primary production in 2002–2017. *Remote Sensing of Environment*, *222*, 165-182. https://doi.org/10.1016/j.rse.2018.12.031

Appendix A: Canopy ET under the DIF assumption

Canopy ET is primarily driven by transpiration through stomatal pores. Accordingly, we begin our derivation by expressing the canopy latent heat flux as a function of surface and aerodynamic conductances, following the bigleaf model formulation (Monteith, 1965). In contrast, the sensible heat flux is controlled solely by aerodynamic conductance.

$$LE_c = L_v \rho \frac{g_c g_{ac}}{g_c + g_{ac}} \frac{MW_r}{PA} [e^*(T_c) - e_a] \qquad (A1)$$

$$H_c = \rho c_p g_{ac} (T_c - T_a) \qquad (A2)$$

where LE_c is latent heat flux at the canopy, H_c is sensible heat flux at the canopy, L_v is latent heat of vaporization, c_p is specific heat of dry air at constant pressure, ρ is air density, PA is air pressure, MW_r is molecular weight ratio of water vapor versus dry air (0.622), g_c is canopy surface conductance, g_{ac} is aerodynamic conductance for heat between canopy surface to the reference height, $e^*(T_c)$ is saturation water vapor at the canopy surface temperature T_c, and q_a is reference height water vapor. Here, we assume that g_{ac} is identical for water vapor and heat transfer (Monin & Obukhov, 1954).

By linearizing the saturation vapor pressure curve, the sensible heat flux can be substituted into the latent heat flux equation as follows (Monteith, 1965):

$$LE_c = \frac{g_c}{g_c + g_{ac}} \frac{\Delta}{\gamma} H_c + L_v \rho \frac{g_c g_{ac}}{g_c + g_{ac}} \frac{MW_r}{PA} VPD_a \qquad (A3)$$

where Δ is the slope of the saturation vapor pressure curve with respect to air temperature (T_a); γ is the psychrometric constant; VPD_a is vapor pressure deficit at the reference height (i.e., $VPD_a = e^*(T_a) - e_a$).

Next, we express H_c using the canopy surface energy balance,

$$H_c = R_{nc} - LE_c \qquad (A4a)$$

$$R_{nc} = (1 - \tau_S) SW_n + (1 - \tau_L)(LW_{atm} + LW_{soil} - 2\varepsilon\sigma {T_c}^4) \qquad (A4b)$$

where SW_n is net shortwave radiation, τ_S and τ_L are shortwave and longwave transmissivity, respectively, LW_{atm} is long wave radiation from atmosphere, LW_{soil} is longwave radiation emitted from soil, ε is land surface emissivity, σ is Stefan-Boltzmann constant. In Equation (A4b), the last term on the right-hand side represents the bidirectional longwave radiation emitted from the canopy.

In order to eliminate dependency of R_{nc} on land surface temperature, we introduce the isothermal net radiation (R_{nci}), which is defined as R_{nc} if $T_c = T_a$ (Kim et al., 2023; Martin, 1989; McColl, 2020; Monteith, 1981; Raupach, 2001).

$$R_{nci} = R_{nc} + 8(1 - \tau_L)\varepsilon\sigma {T_a}^3 (T_c - T_a) \qquad (A5)$$

The last term on the right-hand side of Equation (A5) is a linearized correction accounting for the difference between R_{nc} and R_{nci} due to vertical temperature difference. This term can be expressed using sensible heat flux (Monteith, 1981):

$$8(1 - \tau_L)\varepsilon\sigma {T_a}^3 (T_c - T_a) = \frac{g_{Rc}}{g_{ac}} H_c \qquad (A6)$$

where $g_{Rc}(= \frac{8(1-\tau_c)\varepsilon\sigma {T_a}^3}{\rho c_p})$ is radiative conductance at canopy surface. Substituting Equations (A5) and (A6) into (A4) yields:

$$H_c = \frac{g_{ac}}{g_{ac} + g_{Rc}} (R_{nci} - LE_c) \qquad (A7)$$

Substituting Equation (A7) into Equation (A3) yields:

$$LE_c = \frac{g_c}{g_c + g_{ac}} \frac{\Delta}{\gamma} [\frac{g_{ac}}{g_{ac} + g_{Rc}} (R_{nci} - LE_c)] + L_v \rho \frac{g_c g_{ac}}{g_c + g_{ac}} \frac{MW_r}{PA} VPD_a \qquad (A8)$$

Equation (A8) excludes any meteorological variables at the canopy surface (e.g., surface temperature and humidity), whose values can vary with changes in g_{ac} (Figure 1). Thus, under the DIF assumption (i.e., $\frac{\partial LE_c}{\partial g_{ac}} = 0$), we can consider all variables in Equation (A8), including the flux term, to be independent of g_{ac}. By taking the partial derivative of Equation (A8) with respect to g_{ac} and performing some algebraic manipulation (i.e., multiplying both sides by $\frac{g_{ac}(g_c + g_{ac})}{g_c}$ and then substituting Equation A7), we obtain:

$$0 = [-\frac{g_{ac}}{g_c + g_{ac}} + \frac{g_{Rc}}{g_{ac} + g_{Rc}}] \frac{\Delta}{\gamma} H_c + L_v \rho \frac{g_c g_{ac}}{g_c + g_{ac}} \frac{MW_r}{PA} VPD_a \qquad (A9)$$

By subtracting Equation (A9) from Equation (A3), the last term on the right-hand side of Equation (A3) is canceled, yielding:

$$LE_c = \frac{g_{ac}}{g_{ac} + g_{Rc}} \frac{\Delta}{\gamma} H_c \qquad (A10)$$

By defining $\mu_c = \frac{g_{ac} + g_{Rc}}{g_{ac}}$ and substituting Equation (A4) (i.e., the canopy energy balance equation), Equation (A10) can be expressed as follows.

$$LE_c = \frac{\Delta}{\Delta + \mu_c\gamma} R_{nc} \tag{A11}$$

Equation (A11) is comparable to the equilibrium ET derivation from the DIF hypothesis by Raupach (2001), and it also represents the canopy component of Equation (2) in the main text. However, μ_c still includes the g_{ac} term, which we aim to eliminate. To address this, we performed additional algebraic manipulation by substituting Equation (A10) into Equations (A4) and (A7), respectively.

$$H_c = R_{nc} - \frac{1}{\mu_c}\frac{\Delta}{\gamma} H_c \tag{A12a}$$

$$H_c = \frac{1}{\mu_c}\left(R_{nci} - \frac{1}{\mu_c}\frac{\Delta}{\gamma} H_c\right) \tag{A12b}$$

Next, we rearranged Equations (A12a) and (A12b) with respect to H_c and substituted them into each other to eliminate H_c.

$$\frac{R_{nc}}{1 + \frac{1}{\mu_c}\frac{\Delta}{\gamma}} = \frac{\frac{1}{\mu_c} R_{nci}}{1 + \frac{1}{\mu_c{}^2}\frac{\Delta}{\gamma}} \tag{A13}$$

By performing some algebraic manipulation, we can write:

$$R_{nc}\mu_c{}^2 - R_{nci}\mu_c - \frac{\Delta}{\gamma}(R_{nci} - R_{nc}) = 0 \tag{A14}$$

By solving Equation (A14) with respect to positive μ_c, we obtain:

$$\mu_c = \frac{R_{nci} + \sqrt{R_{nci}{}^2 + 4\frac{\Delta}{\gamma} R_{nc}(R_{nci} - R_{nc})}}{2R_{nc}} \tag{A15}$$

At this stage, the expression for μ_c no longer depends on g_{ac}. We can also express Equation (A15) explicitly using vertical temperature difference by substituting Equation (A5) to eliminate R_{ni}, which yields:

$$\mu_c = \frac{R_{nc} + 8(1-\tau_L)\varepsilon\sigma T_a{}^3(T_c - T_a)}{2R_{nc}} + \frac{\sqrt{[R_{nc} + 8(1-\tau_L)\varepsilon\sigma T_a{}^3(T_c - T_a)]^2 + 32\frac{\Delta}{\gamma} R_{nc}(1-\tau_L)\varepsilon\sigma T_a{}^3(T_c - T_a)}}{2R_{nc}} \tag{A16}$$

Equation (A16) is equivalent to Equation (3a) in the main text.

Appendix B: Soil ET under the DIF assumption

The derivation of soil ET under the DIF assumption follows a similar procedure to that of the canopy component. Therefore, this section largely repeats the content of Appendix A. However, we provide a standalone Appendix B for the soil component to highlight several key differences. In particular, the parameterization of water stress and the inclusion of soil heat flux introduce slight variations in both the derivation and the resulting equations.

Unlike canopy evapotranspiration, which is primarily regulated by stomatal pores, soil evaporation is constrained by the soil surface water potential. This water potential can be represented by the relative humidity at the surface–air interface (Novak, 2019). Accordingly, we parameterize the latent heat flux at the soil surface as follows (Kim et al., 2021; Monteith, 1981):

$$LE_s = L_v \rho g_{as} \frac{MW_r}{PA} [RH_s e^*(T_s) - e_a] \qquad (B1)$$

$$H_s = \rho c_p g_{as} (T_s - T_a) \qquad (B2)$$

where LE_s is latent heat flux at the soil, H_s is sensible heat flux at the soil, g_{as} is aerodynamic conductance for heat and water vapor between soil surface to the reference height, RH_s is relative humidity at the soil surface, and T_s is soil surface temperature.

While g_c was assumed to be independent of g_{ac} in the canopy model, RH_s, representing water potential, is similarly assumed to be independent of g_{as} in the soil model. Also, we assume same land surface temperature for canopy and soil at daily time scale.

By linearizing the saturation vapor pressure curve, the sensible heat flux can be substituted into the latent heat flux equation as follows (Kim et al., 2021; Monteith, 1981):

$$LE_s = \frac{RH_s \Delta}{\gamma} H_s + L_v \rho g_{as} \frac{MW_r}{PA} [RH_s e^*(T_a) - e_a] \qquad (B3)$$

Next, we express H_s using the soil surface energy balance.

$$H_s = R_{ns} - G - LE_s \qquad (B4a)$$

$$R_{ns} = \tau_S SW_n + \tau_L LW_{atm} + (1 - \tau_L) LW_{canopy} - \varepsilon \sigma {T_s}^4 \qquad (B4b)$$

where R_{ns} is net radiation at soil surface, G is soil heat flux, LW_{canopy} is longwave radiation emitted from canopy. In Equation (B4b), the last term on the right-hand side represents longwave radiation emitted from the canopy.

As for soil heat flux, we express it using a “one-layer” model (McColl, 2020; Raupach, 2001):

$$G = \frac{k_g}{d_g}\left(T_s - T_g\right) \qquad (B5)$$

where k_g is the thermal conductivity of the soil, d_g is a soil storage length scale, and T_g is a specified bulk temperature for the thermal store, representing the subsurface temperature. Specifically, d_g and T_g are defined as the depth and corresponding temperature, respectively, below which temperature is not directly influenced by aerodynamic exchange at the daily time scale.

The isothermal available energy at the soil surface can be defined as follows model (McColl, 2020; Raupach, 2001):

$$\underbrace{R_{nsi} - G_i}_{AE_{si}} = \underbrace{R_{ns} - G}_{AE_s} + [4\varepsilon\sigma {T_a}^3 + \frac{k_g}{d_g}](T_s - T_a) \qquad (B6)$$

where $f_s(= 1 - f_v)$ is fraction of soil, AE_s is available energy at the soil surface, and AE_{si} represents isothermal available energy at the soil surface. The last term on the right-hand side of Equation (B6) is a linearized correction due to vertical temperature difference. This term can be expressed using sensible heat flux:

$$[4\varepsilon\sigma {T_a}^3 + \frac{k_g}{d_g}](T_s - T_a) = \frac{g_{Rs} + g_g}{g_{as}} H_s \qquad (B7)$$

where $g_{Rs}(= \frac{4\varepsilon\sigma {T_a}^3}{\rho c_p})$ is radiative conductance at soil surface, $g_g(= \frac{k_g/d_g}{\rho c_p})$ is storage conductance. Substituting Equations (B6) and (B7) into (B4) yields:

$$H_s = \frac{g_{as}}{g_{as} + g_{Rs} + g_g}(AE_{si} - LE_s) \qquad (B8)$$

Substituting Equation (B8) into Equation (B3) yields:

$$LE_s = \frac{RH_s\Delta}{\gamma}[\frac{g_{as}}{g_{as} + g_{Rs} + g_g}(AE_{si} - LE_s)] + L_v\rho g_{as}\frac{MW_r}{PA}[RH_s e^*(T_a) - e_a] \qquad (B9)$$

Equation (B9) excludes any meteorological variables at the soil surface (e.g., surface temperature and humidity), whose values can vary with changes in g_{as} (Figure 1). Thus, under the DIF assumption (i.e., $\frac{\partial LE_s}{\partial g_{as}} = 0$), we can consider all variables in Equation (B9), including the flux term, to be independent of g_{as}. By taking the partial derivative of Equation (B9) with respect to g_{as} and performing some algebraic manipulation (i.e., multiplying both sides by g_{as} and then substituting Equation B8), we obtain:

$$0 = \frac{g_{Rs} + g_g}{g_{as} + g_{Rs} + g_g}\frac{RH_s\Delta}{\gamma}H_s + L_v\rho g_{as}\frac{MW_r}{PA}[RH_s e^*(T_a) - e_a] \qquad (B10)$$

By subtracting Equation (B10) from Equation (B3), the last term on the right-hand side of Equation (B3) is canceled, yielding:

$$LE_s = \frac{g_{as}}{g_{as} + g_{Rs} + g_g} \frac{RH_s\Delta}{\gamma} H_s \qquad (B11)$$

By defining $\mu_s = \frac{g_{as}+g_{Rs}+g_g}{g_{as}}$ and substituting Equation (B4) (i.e., the soil surface energy balance equation), Equation (B11) can be expressed as follows.

$$LE_s = \frac{RH_s\Delta}{RH_s\Delta + \mu_s\gamma}(R_{ns} - G) \qquad (B12)$$

Equation (B12) represents the soil component of Equation (2) in the main text.

Next, we eliminate g_{as} from μ_s by performing additional algebraic manipulation. Substituting Equation (B11) into Equations (B4) and (B8), respectively.

$$H_s = AE_s - \frac{1}{\mu_s}\frac{RH_s\Delta}{\gamma}H_s \qquad (B13a)$$

$$H_s = \frac{1}{\mu_s}\left(AE_{si} - \frac{1}{\mu_s}\frac{RH_s\Delta}{\gamma}H_s\right) \qquad (B13b)$$

Rearranging Equations (B13a) and (B13b) with respect to H_s and substituted them into each other to eliminate H_s.

$$\frac{AE_s}{1 + \frac{1}{\mu_s}\frac{RH_s\Delta}{\gamma}} = \frac{\frac{1}{\mu_s}AE_{si}}{1 + \frac{1}{{\mu_s}^2}\frac{RH_s\Delta}{\gamma}} \qquad (B14)$$

By performing some algebraic manipulation, we can write:

$$AE_s{\mu_s}^2 - AE_{si}\mu_s - \frac{RH_s\Delta}{\gamma}(AE_{si} - AE_s) = 0 \qquad (B15)$$

By solving Equation (B15) with respect to positive μ_s, we obtain:

$$\mu_s = \frac{AE_{si} + \sqrt{{AE_{si}}^2 + 4\frac{RH_s\Delta}{\gamma}AE_s(AE_{si} - AE_s)}}{2AE_s} \qquad (B16)$$

At this stage, the expression for μ_s no longer depends on g_{as}. We can also express Equation (B16) explicitly using vertical temperature difference by substituting Equation (B6) to eliminate AE_{si}, which yields:

$$\mu_s = \frac{AE_s + (4\varepsilon\sigma {T_a}^3 + \frac{k_g}{d_g})(T_s - T_a)}{2AE_s} + \frac{\sqrt{[AE_s + (4\varepsilon\sigma {T_a}^3 + \frac{k_g}{d_g})(T_s - T_a)]^2 + 4\frac{RH_s\Delta}{\gamma}AE_s(4\varepsilon\sigma {T_a}^3 + \frac{k_g}{d_g})(T_s - T_a)}}{2AE_s} \qquad (B17)$$

Equation (B17) is equivalent to Equation (3b) in the main text.

Appendix C: Derivation of Equation 10

With given land surface temperature (*LST*), the daily total sensible heat flux can be written as:

$$H = \rho c_p g_{aH}(LST - T_a) \tag{C1}$$

where g_{aH} is the daily aerodynamic conductance for heat. All temperature variables in Equation (C1) represent daily average.

The ratio between the canopy sensible heat flux (Equation A2) and the total sensible heat flux (Equation C1) can then be expressed as:

$$\frac{H_c}{H} = \frac{\rho c_p g_{ac}(T_c - T_a)}{\rho c_p g_{aH}(LST - T_a)} \tag{C2}$$

From the single source perspective (e.g., bigleaf parameterization), the canopy surface can be considered to function aerodynamically as the land surface itself. In other words, *LST* is interpreted as the temperature at the displacement height, which is typically 60–70% of canopy height (Knauer et al., 2018). Under this interpretation, the aerodynamic conductance for the whole surface is reasonably approximated by the aerodynamic conductance of the canopy layer. Therefore, we can set $g_{aH} \approx g_{ac}$, and Equation (C2) simplifies to:

$$\frac{T_c - T_a}{LST - T_a} = \frac{H_c}{H} \tag{C3}$$

With the DIF constrain, total and canopy sensible heat fluxes can be written as:

$$H_c = \frac{\mu_c \gamma}{\Delta + \mu_c \gamma} R_{nc} \tag{C4a}$$

$$H = \frac{\mu_c \gamma}{\Delta + \mu_c \gamma} R_{nc} + \frac{\mu_s \gamma}{RH_s \Delta + \mu_s \gamma} (R_{ns} - G) \tag{C4b}$$

Substituting Equations (C4a) and (C4b) into Equation (C3) gives:

$$\frac{T_c - T_a}{LST - T_a} = \frac{\frac{\mu_c \gamma}{\Delta + \mu_c \gamma} R_{nc}}{\frac{\mu_c \gamma}{\Delta + \mu_c \gamma} R_{nc} + \frac{\mu_s \gamma}{RH_s \Delta + \mu_s \gamma} (R_{ns} - G)} \tag{C5}$$

Because several terms in (C5) require knowledge of T_s and T_c, further approximations are introduced to obtain a tractable expression without iteration.

First, we assume soil heat flux is negligible at the daily timescale for this derivation. Dividing both numerator and denominator of (C5) by net radiation yields:

$$\frac{T_c - T_a}{LST - T_a} = \frac{\frac{\mu_c \gamma}{\Delta + \mu_c \gamma} f_c}{\frac{\mu_c \gamma}{\Delta + \mu_c \gamma} f_c + \frac{\mu_s \gamma}{RH_s \Delta + \mu_s \gamma}(1 - f_c)} \quad (C6)$$

where f_c represents the fraction of net radiation absorbed by the canopy.

Second, we assume that the μ_c and μ_s terms are close to unity, implying small differences between surface and air temperatures. Thus, the expression simplifies to:

$$\frac{T_c - T_a}{LST - T_a} = \frac{f_c}{f_c + \frac{\Delta + \gamma}{RH_s \Delta + \gamma}(1 - f_c)} \quad (C7)$$

Third, we assume that the soil surface relative humidity is close to the atmospheric relative humidity at reference height ($RH_s = RH_a$) (Kim et al., 2021). This yields:

$$\frac{T_c - T_a}{LST - T_a} = \frac{f_c}{f_c + \frac{\Delta + \gamma}{RH_a \Delta + \gamma}(1 - f_c)} \quad (C8)$$

Rearranging Equation (C8) gives Equations (10a) and (10b) in the main text.

Appendix Reference

Kim, Y., Garcia, M., Black, T. A., & Johnson, M. (2023). Assessing the complementary role of surface flux equilibrium (SFE) theory and maximum entropy production (MEP) principle in the estimation of actual evapotranspiration. *Journal of Advances in Modeling Earth Systems*, *15*(7), e2022MS003224. https://doi.org/10.1029/2022MS003224

Kim, Y., Garcia, M., Morillas, L., Weber, U., Black, T. A., & Johnson, M. S. (2021). Relative humidity gradients as a key constraint on terrestrial water and energy fluxes. *Hydrology and Earth System Sciences*, *25*(9), 5175-5191. https://doi.org/10.5194/hess-25-5175-2021

Knauer, J., El-Madany, T. S., Zaehle, S., & Migliavacca, M. (2018). Bigleaf—An R package for the calculation of physical and physiological ecosystem properties from eddy covariance data. *PLOS ONE*, *13*(8), e0201114. https://doi.org/10.1371/journal.pone.0201114

Martin, P. (1989). The significance of radiative coupling between vegetation and the atmosphere. *Agricultural and Forest Meteorology*, *49*(1), 45-53. https://doi.org/10.1016/0168-1923(89)90061-0

McColl, K. A. (2020). Practical and theoretical benefits of an alternative to the Penman-Monteith evapotranspiration equation. *Water Resources Research*, *56*(6), e2020WR027106. https://doi.org/10.1029/2020wr027106

Monin, A. S., & Obukhov, A. M. (1954). Basic laws of turbulent mixing in the surface layer of the atmosphere. *Contrib. Geophys. Inst. Acad. Sci. USSR*, *151*(163), e187.

Monteith, J. L. (1965). Evaporation and environment. Symposia of the society for experimental biology,

Monteith, J. L. (1981). Evaporation and surface temperature. *Quarterly Journal of the Royal Meteorological Society*, *107*(451), 1-27. https://doi.org/10.1002/qj.49710745102

Novak, M. D. (2019). Validity of assuming equilibrium between liquid water and vapor for simulating evaporation. *Water Resources Research*, *55*(11), 9858-9872. https://doi.org/10.1029/2019WR025113

Raupach, M. R. (2001). Combination theory and equilibrium evaporation. *Quarterly Journal of the Royal Meteorological Society*, *127*(574), 1149-1181. https://doi.org/10.1002/qj.49712757402

Supplementary Materials

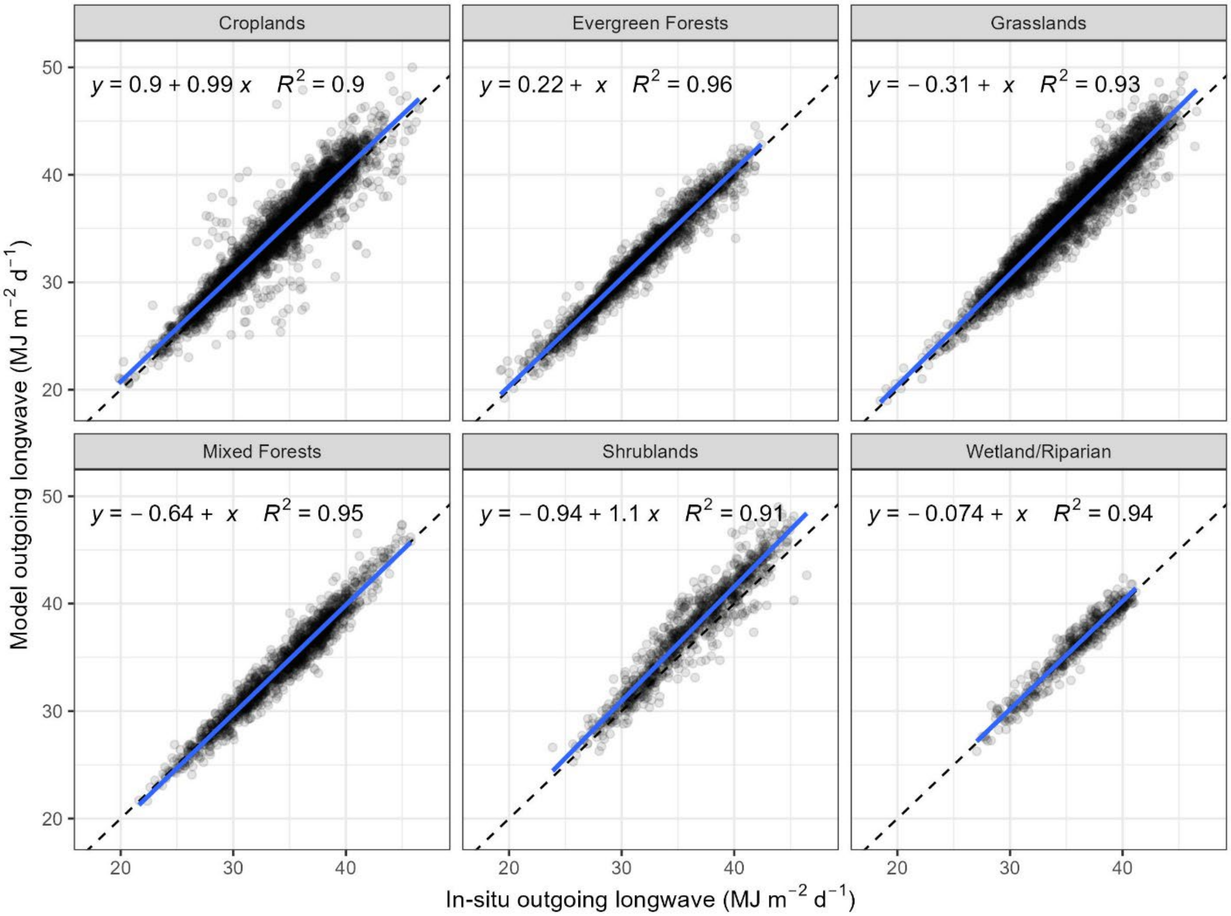

Figure S1 Evaluation of daily mean land-surface temperature (LST_{daily}) estimated from satellite observations. The x-axis represents the daily outgoing longwave radiation observed at flux tower sites, while the y-axis represents outgoing longwave radiation calculated from modeled LST_{daily}. Each panel corresponds to a different land cover type.

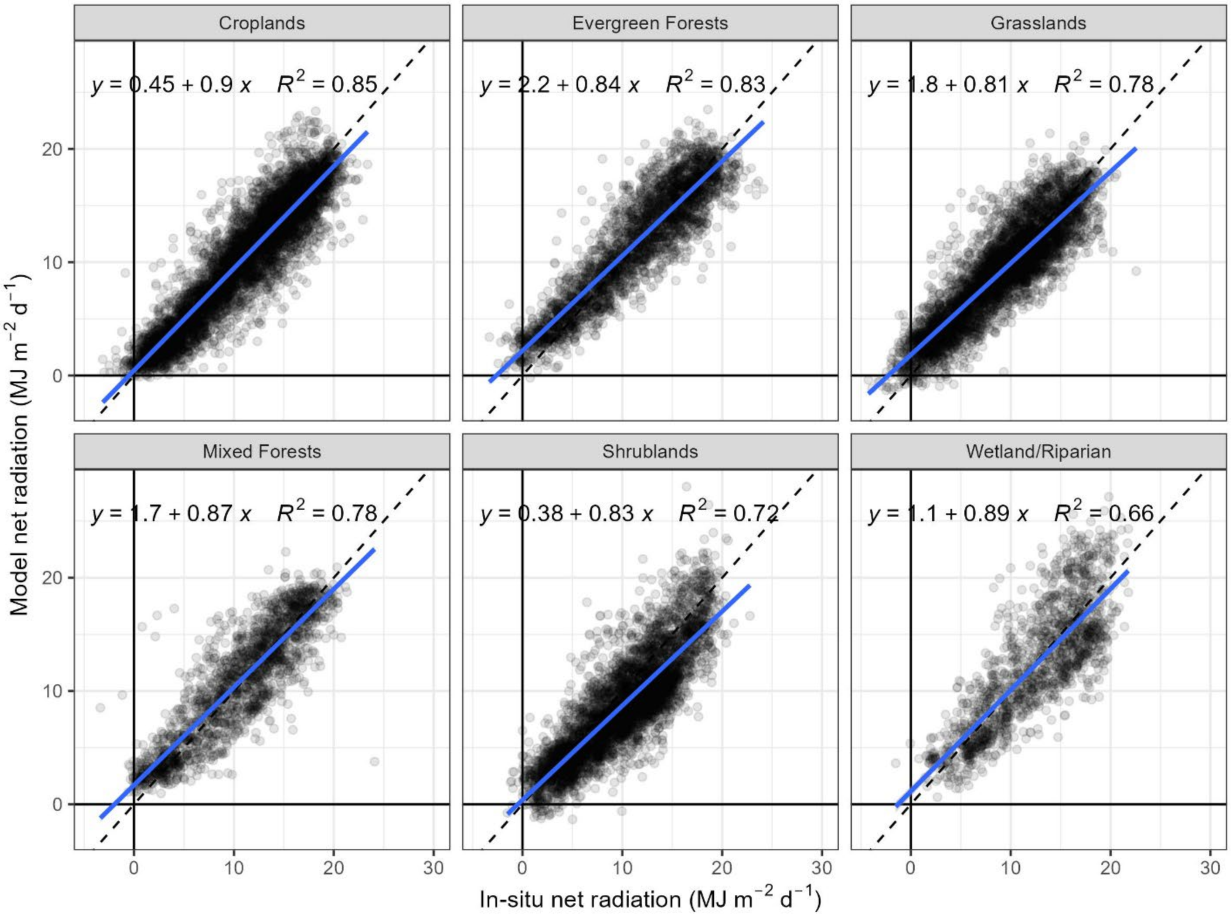

Figure S2 Evaluation of daily net radiation estimated from satellite observations and grid meteorological data. The x-axis represents the daily net radiation observed at flux tower sites, while the y-axis represents estimated daily net radiation based on Landsat scene and gridMET meteorological data. Each panel corresponds to a different land cover type.

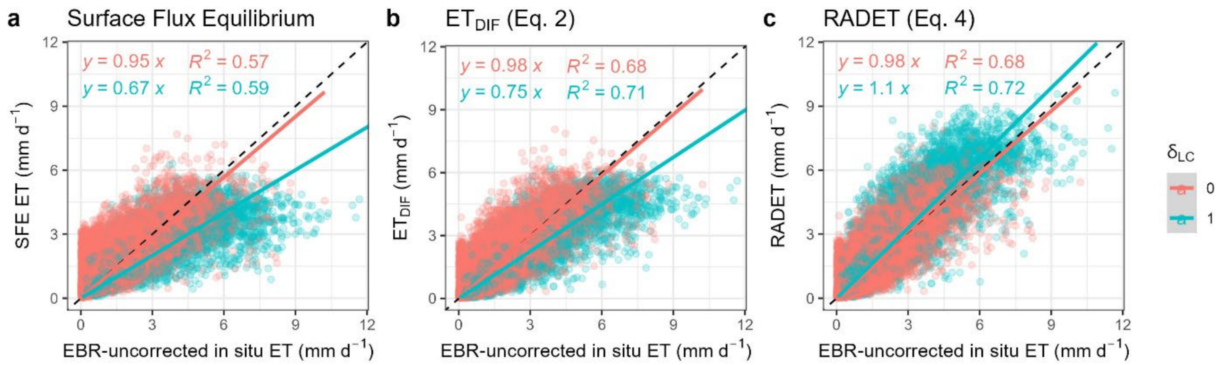

Figure S3 In situ ET observations versus estimated daily ET using the SFE (a), ETDIF (b) and RADET (c) models. Observed ET represents energy balance ratio (EBR) uncorrected data. The dashed line indicates the 1:1 line, and point colors differentiate $\delta_{LC} = 0$ and $\delta_{LC} = 1$. R^2 and the least-squares linear regression forced through the origin are shown (solid line).

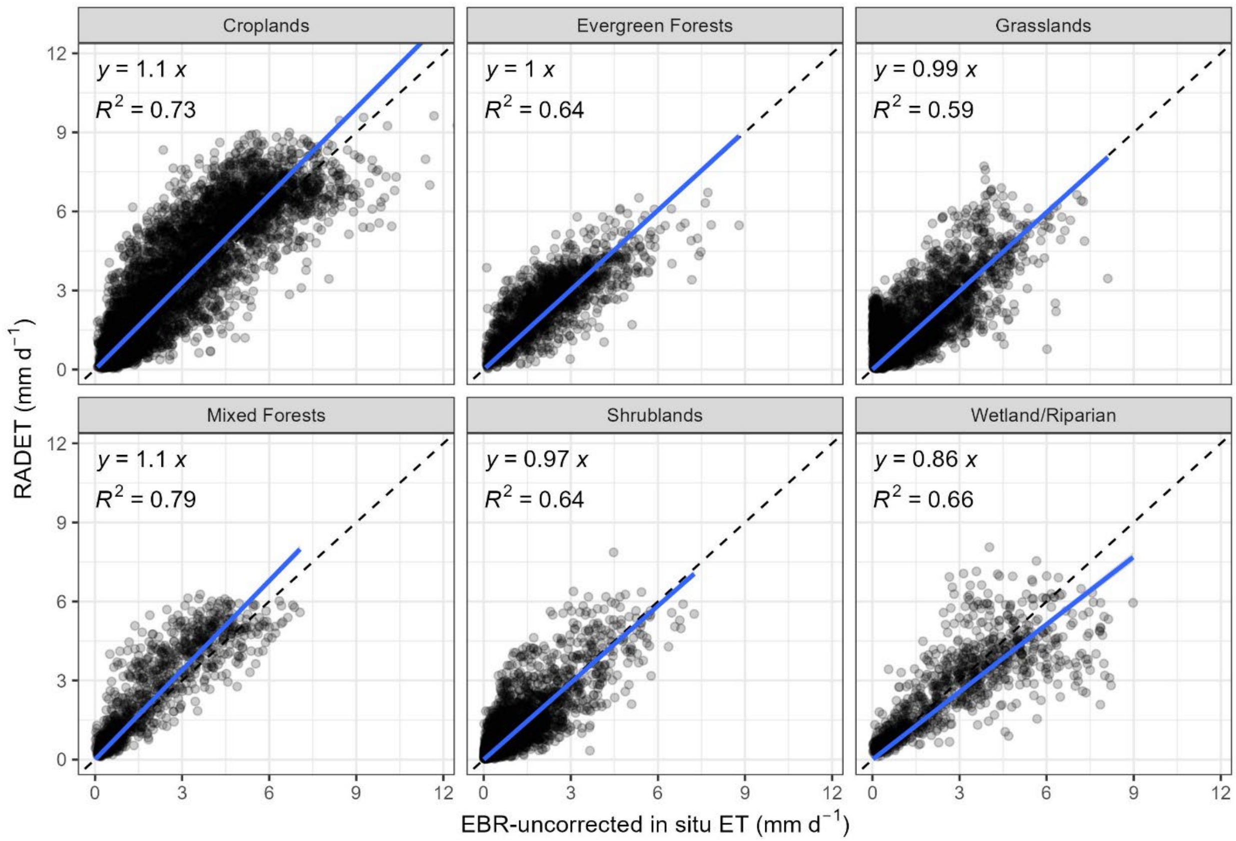

Figure S4 Daily RADET versus in-situ ET observations grouped by land cover type. Observed ET represents energy balance ratio uncorrected data. For each land cover group, the least-squares linear regression forced through the origin and R^2 are shown.

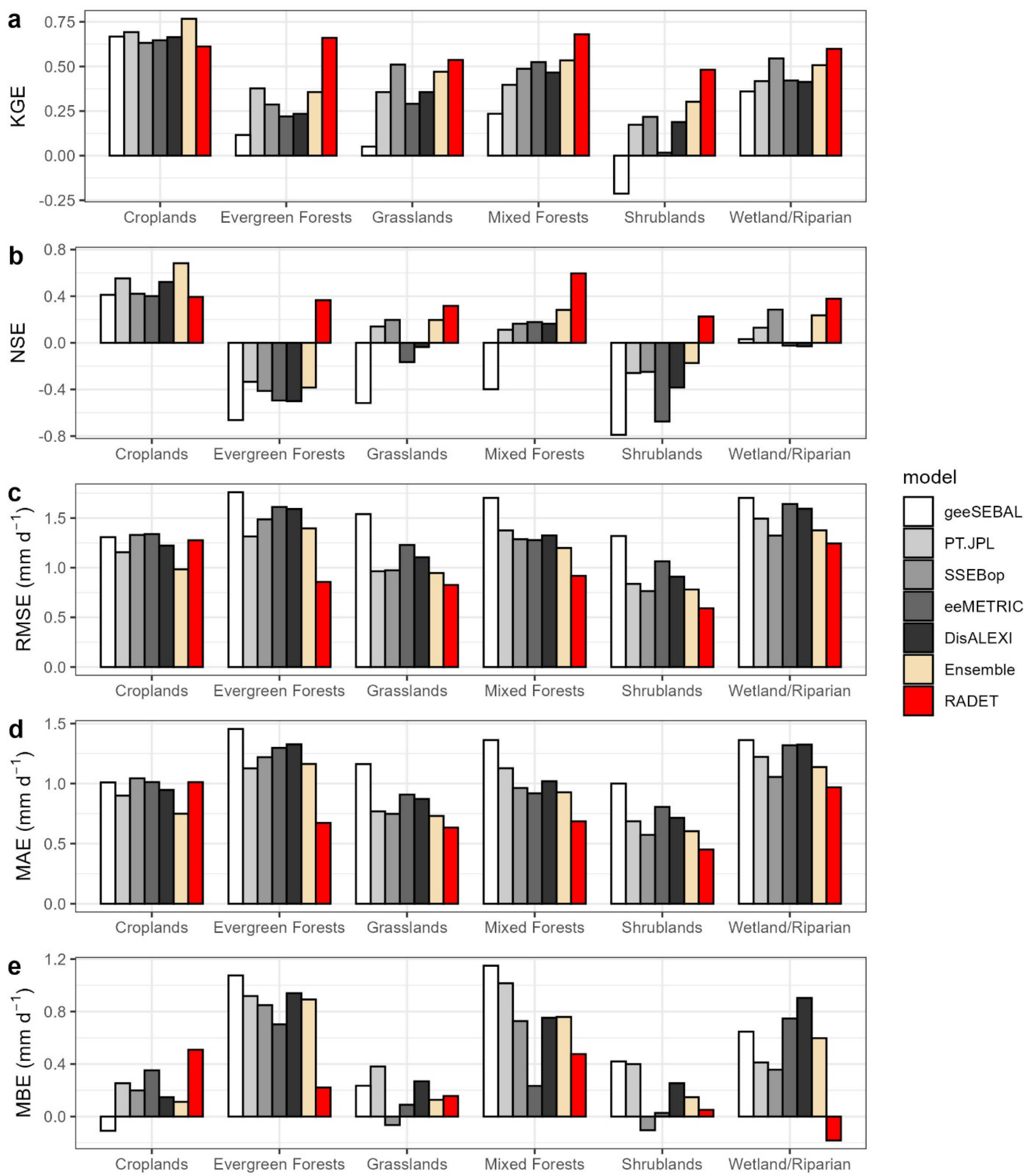

Figure S5 Comparison of daily error statistics between RADET and OpenET models, grouped by land cover type. Model evaluations were performed using EBR–uncorrected in situ ET as the benchmark.

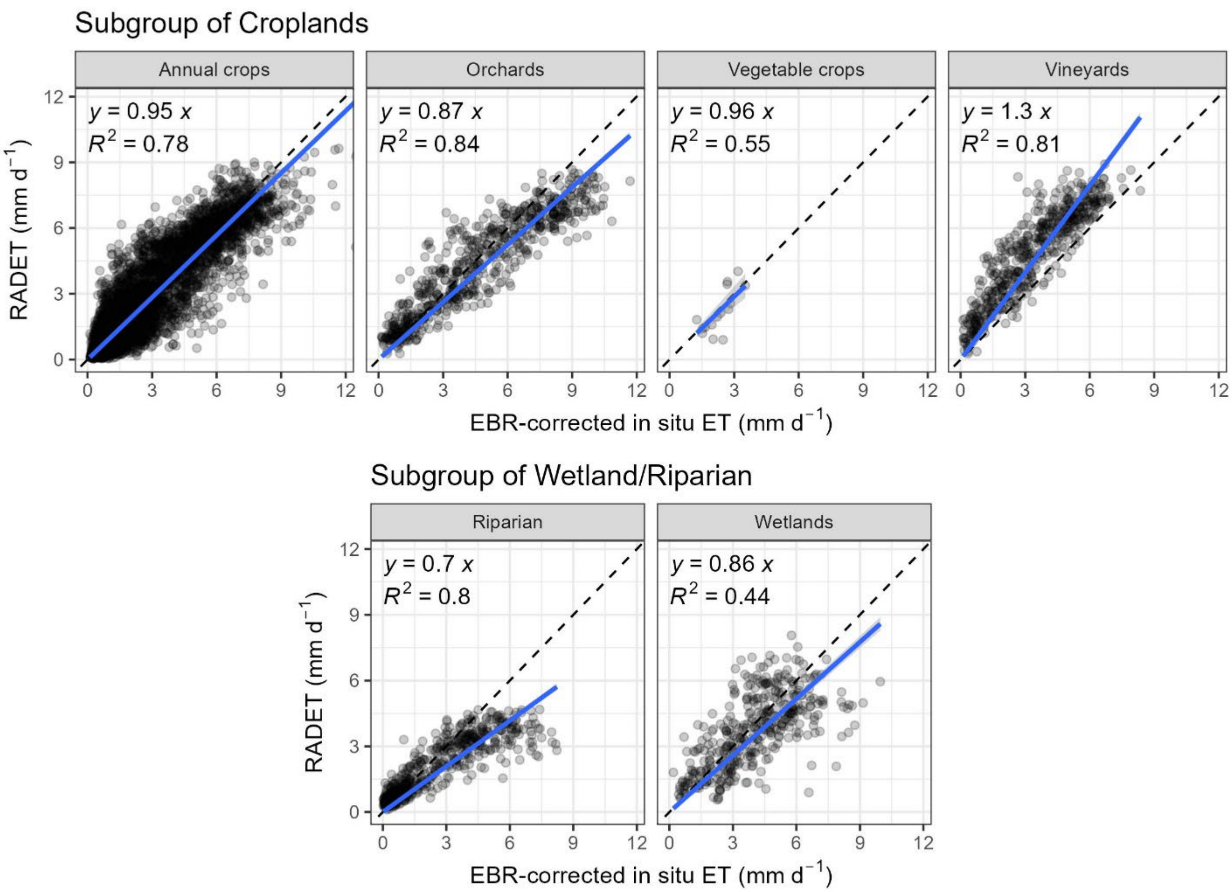

Figure S6 Daily RADET versus in-situ ET observations grouped by land cover subgroups. Observed ET represents energy balance ratio corrected data. For each land cover subgroup, R^2 and the least-squares linear regression forced through the origin are shown.

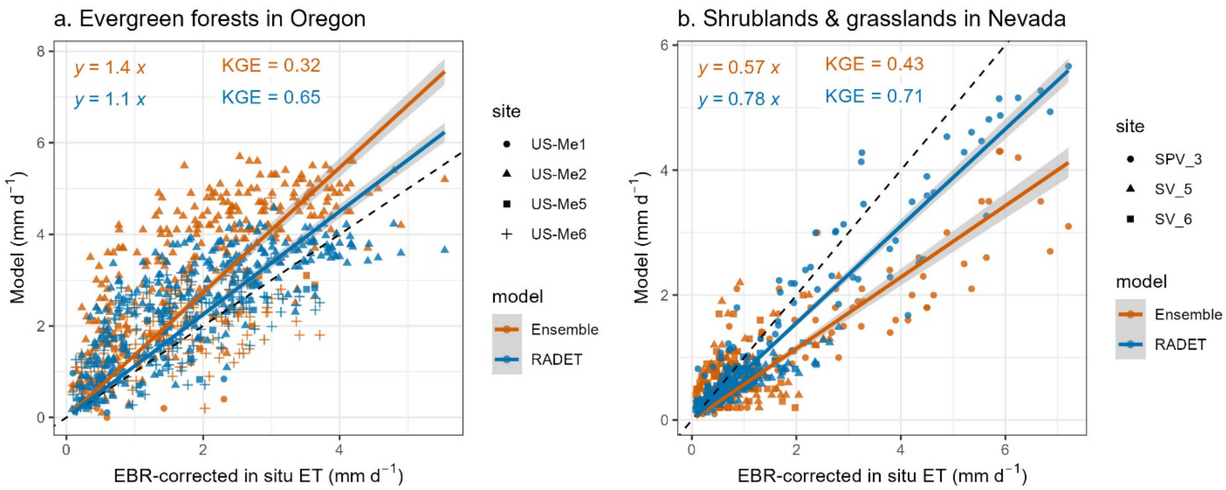

Figure S7 Model estimates versus in situ ET observations (EBR-corrected) for (a) forest sites shown in Figure 5 and (b) shrubland and grassland sites shown in Figure 6. Blue points represent the OpenET ensemble, whereas orange points indicate RADET estimates. Different point shapes correspond to different sites. The dashed line denotes the 1:1 line, and the colored solid lines represent the least-squares regression lines forced through the origin. The Kling-Gupta efficiency (KGE) and regression statistics are also shown.

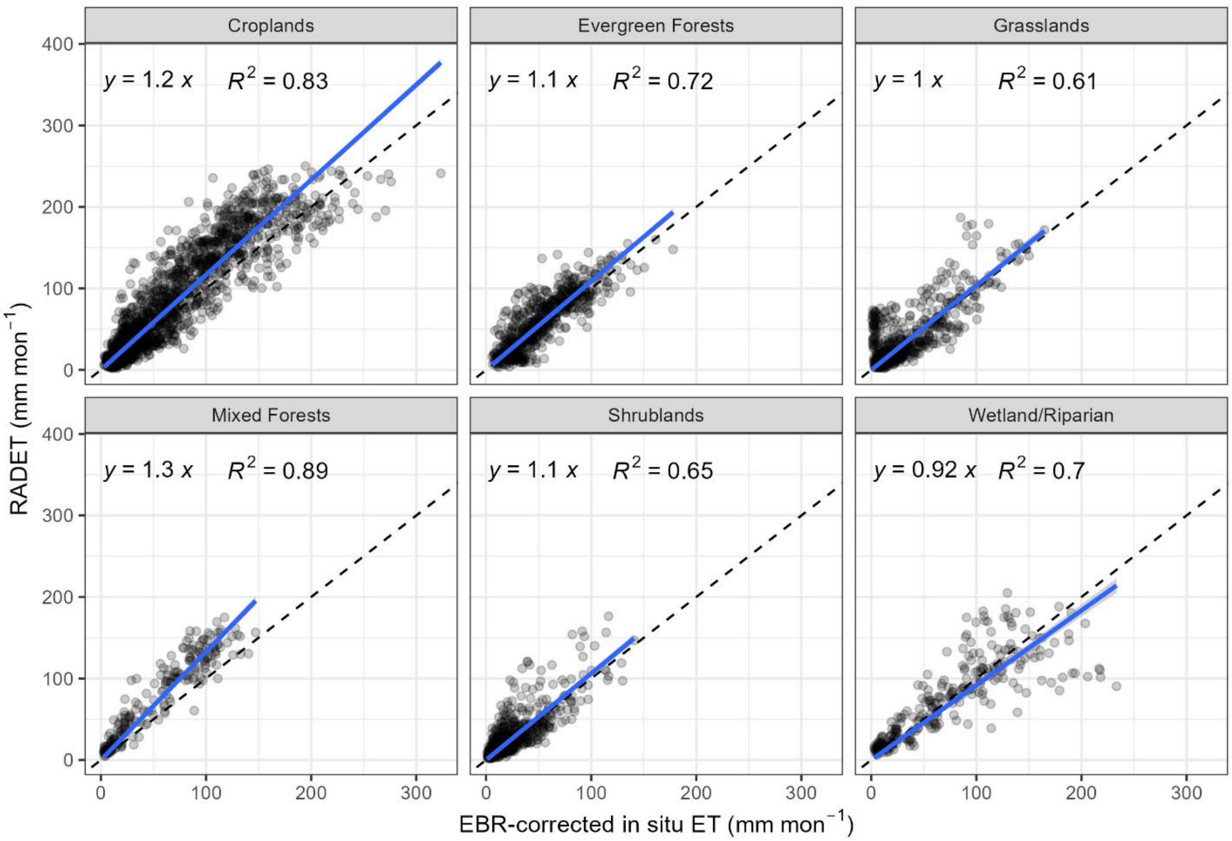

Figure S8 Monthly RADET versus in-situ ET observations grouped by land cover type. Observed ET represents *EBR* uncorrected data. Points indicate results under the strict benchmark criterion (≤5 gap-filled days). For each land cover group, R^2 *and* the least-squares linear regression forced through the origin are shown.

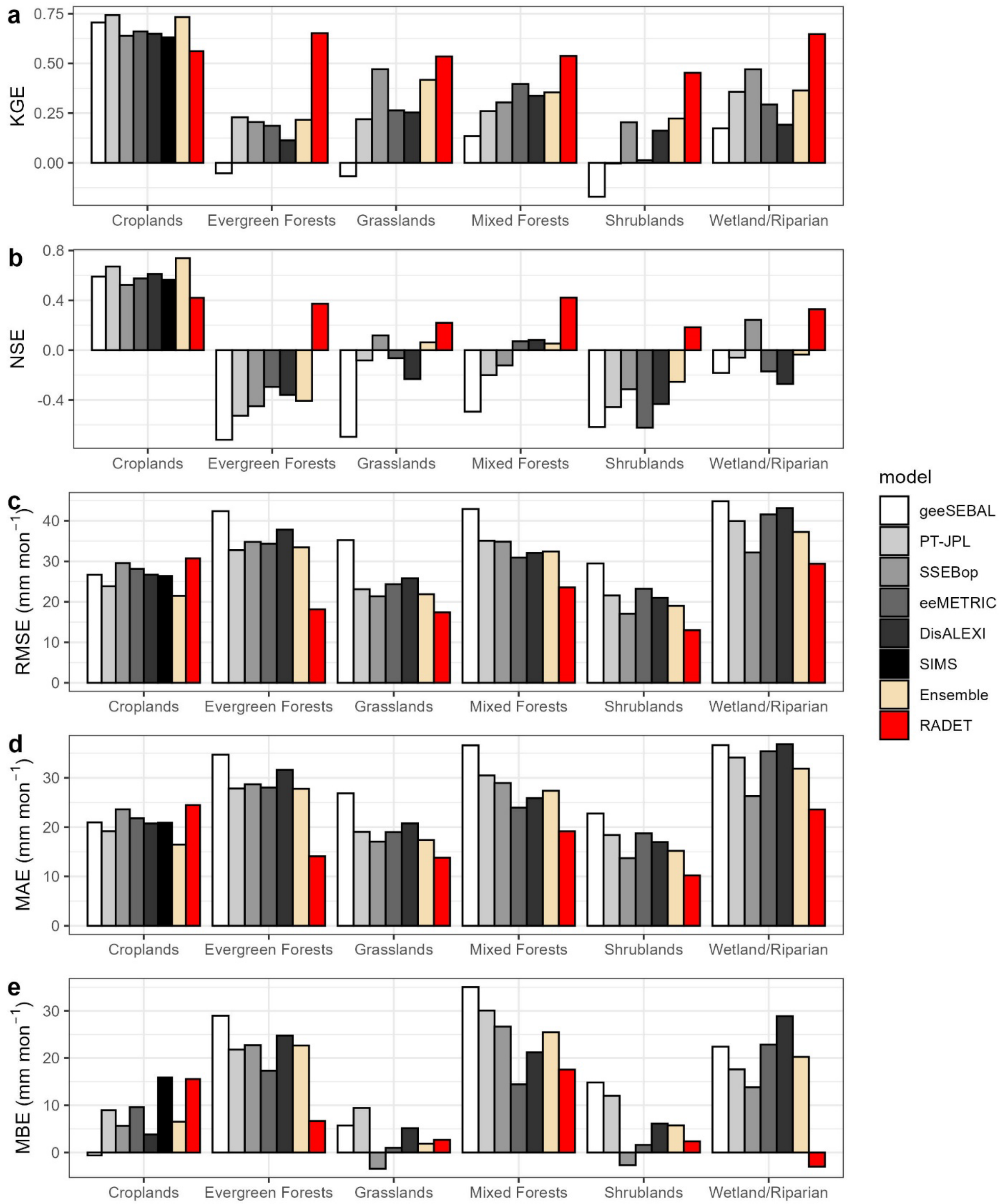

Figure S9 Comparison of monthly error statistics between RADET and OpenET models, grouped by land cover type. Model evaluations were performed using EBR–uncorrected in situ ET as the benchmark.

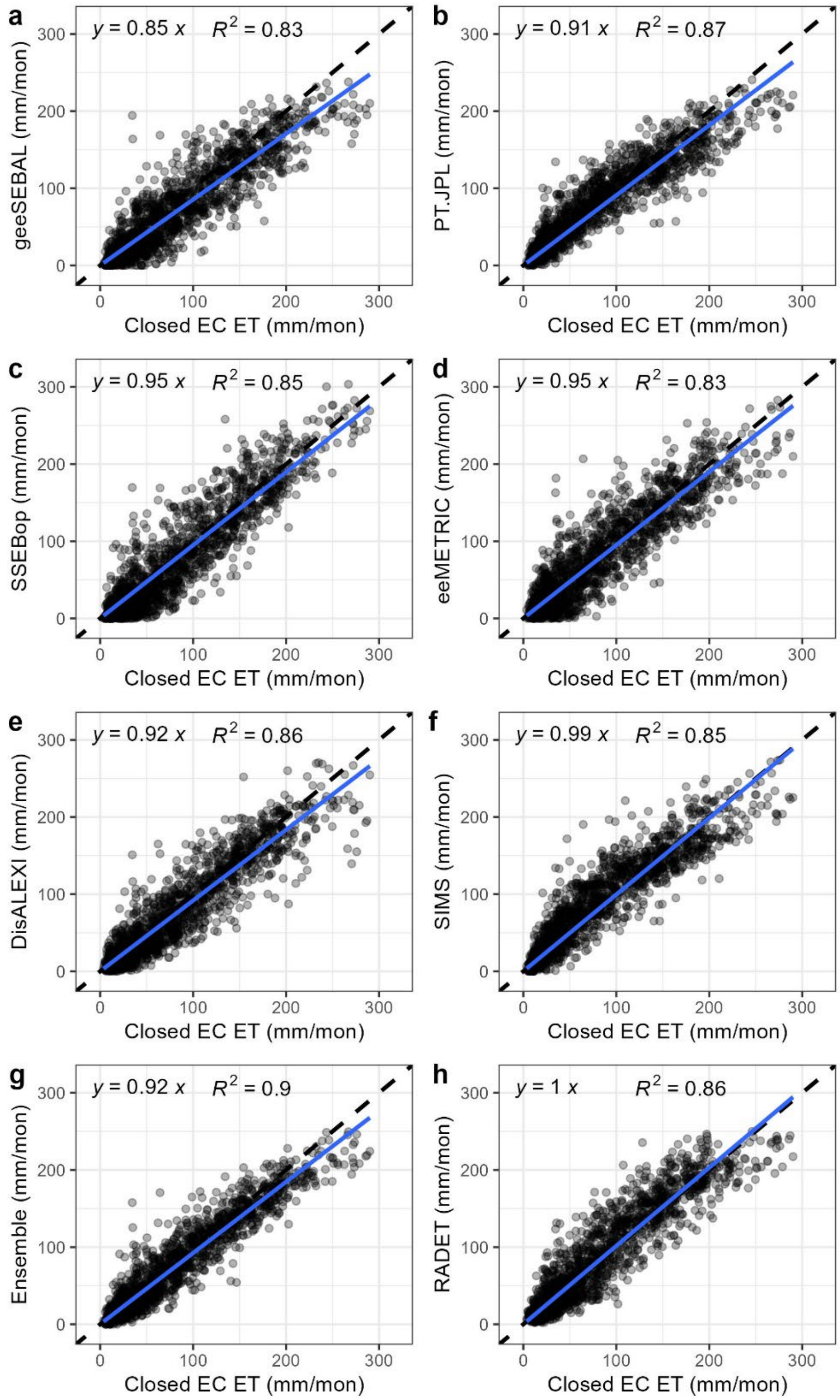

Figure S10 Monthly model estimates versus in situ ET observations (EBR-corrected) over cropland sites. Panels (a)–(f) show individual OpenET model estimates, panel (g) shows the OpenET ensemble, and panel (h) presents RADET. The dashed line denotes the 1:1 line, and the solid lines represent least-squares regression lines forced through the origin.

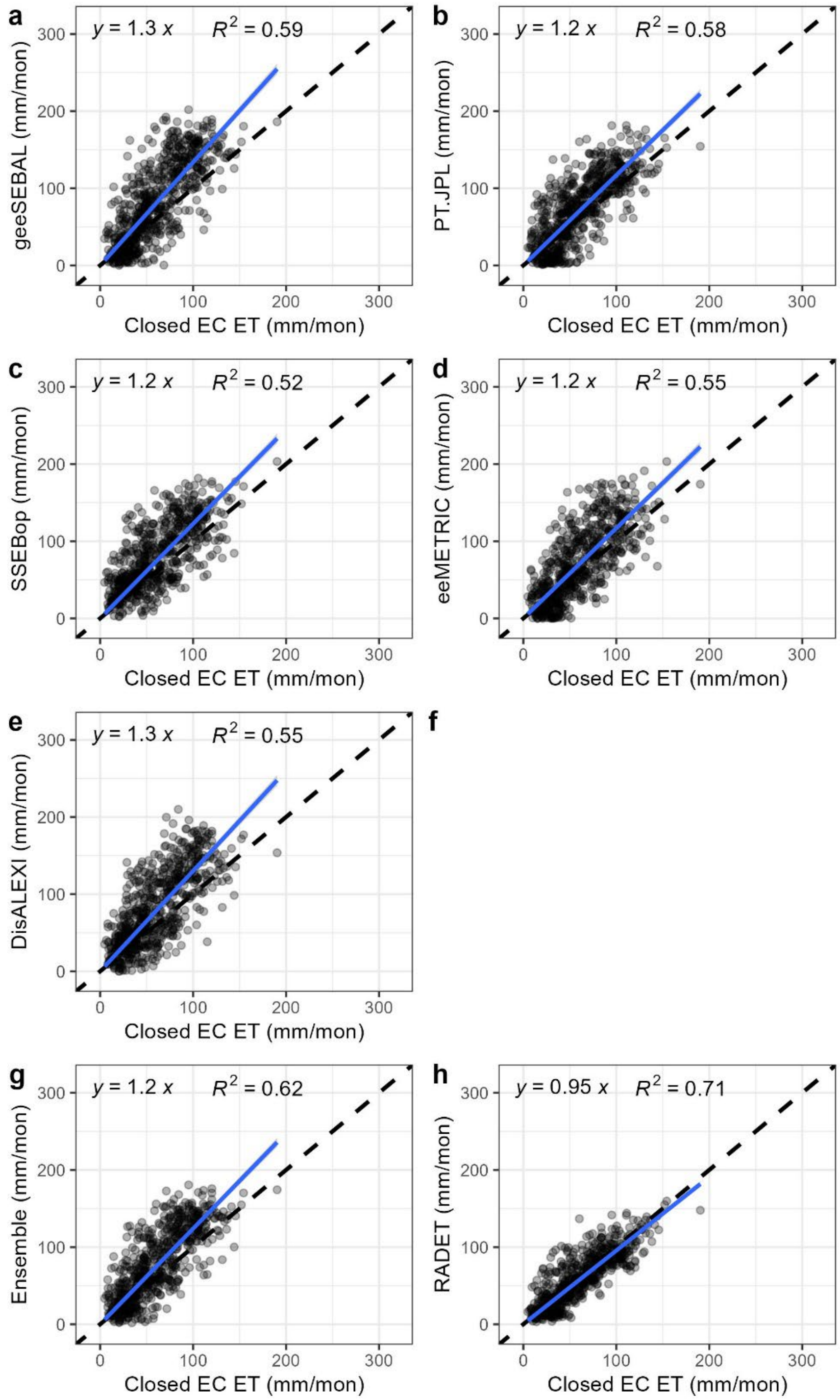

Figure S11 Monthly model estimates versus in situ ET observations (EBR-corrected) over evergreen forest sites. Panels (a)–(f) show individual OpenET model estimates, panel (g) shows the OpenET ensemble, and panel (h) presents RADET. The dashed line denotes the 1:1 line, and the solid lines represent least-squares regression lines forced through the origin.

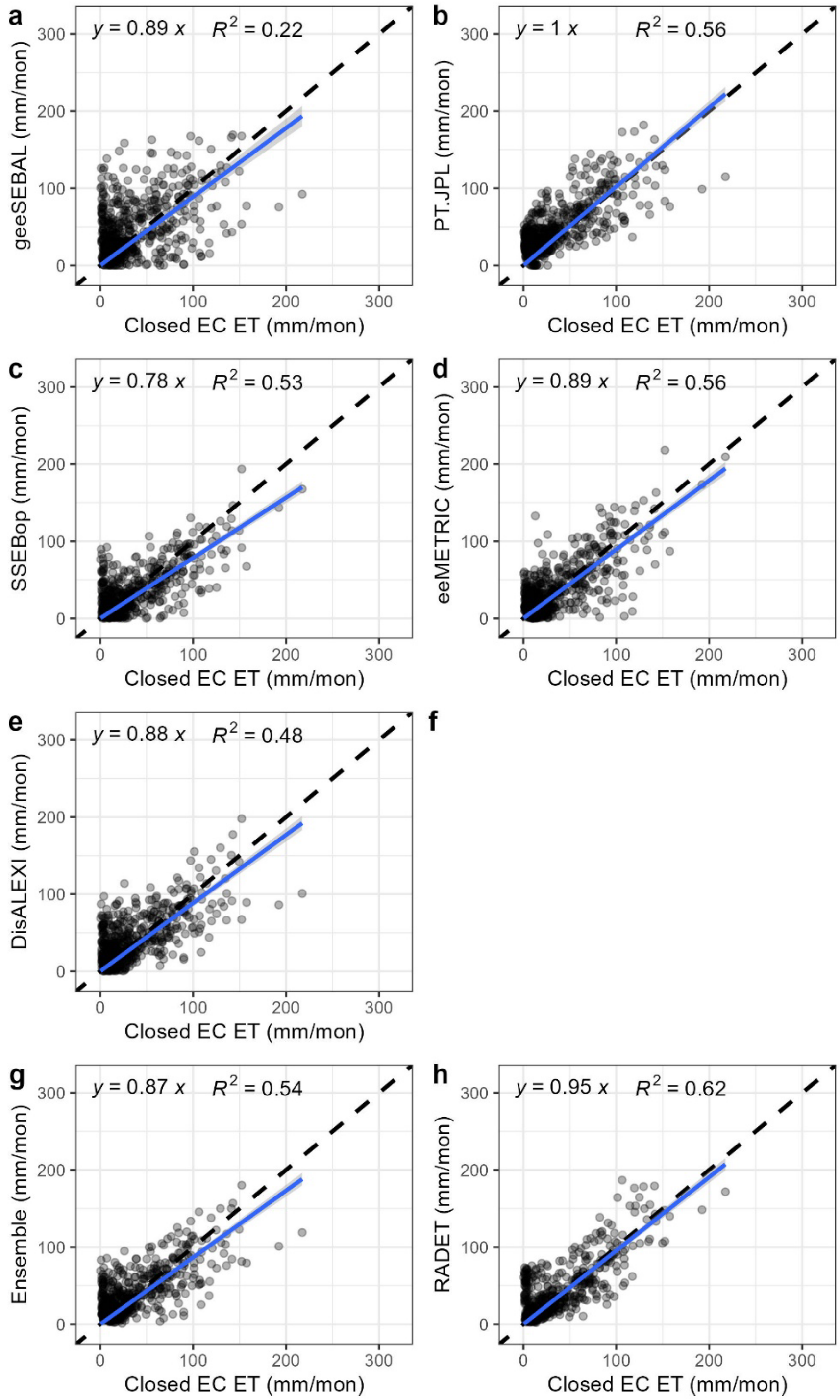

Figure S12 Monthly model estimates versus in situ ET observations (EBR-corrected) over grassland sites. Panels (a)–(f) show individual OpenET model estimates, panel (g) shows the OpenET ensemble, and panel (h) presents RADET. The dashed line denotes the 1:1 line, and the solid lines represent least-squares regression lines forced through the origin.

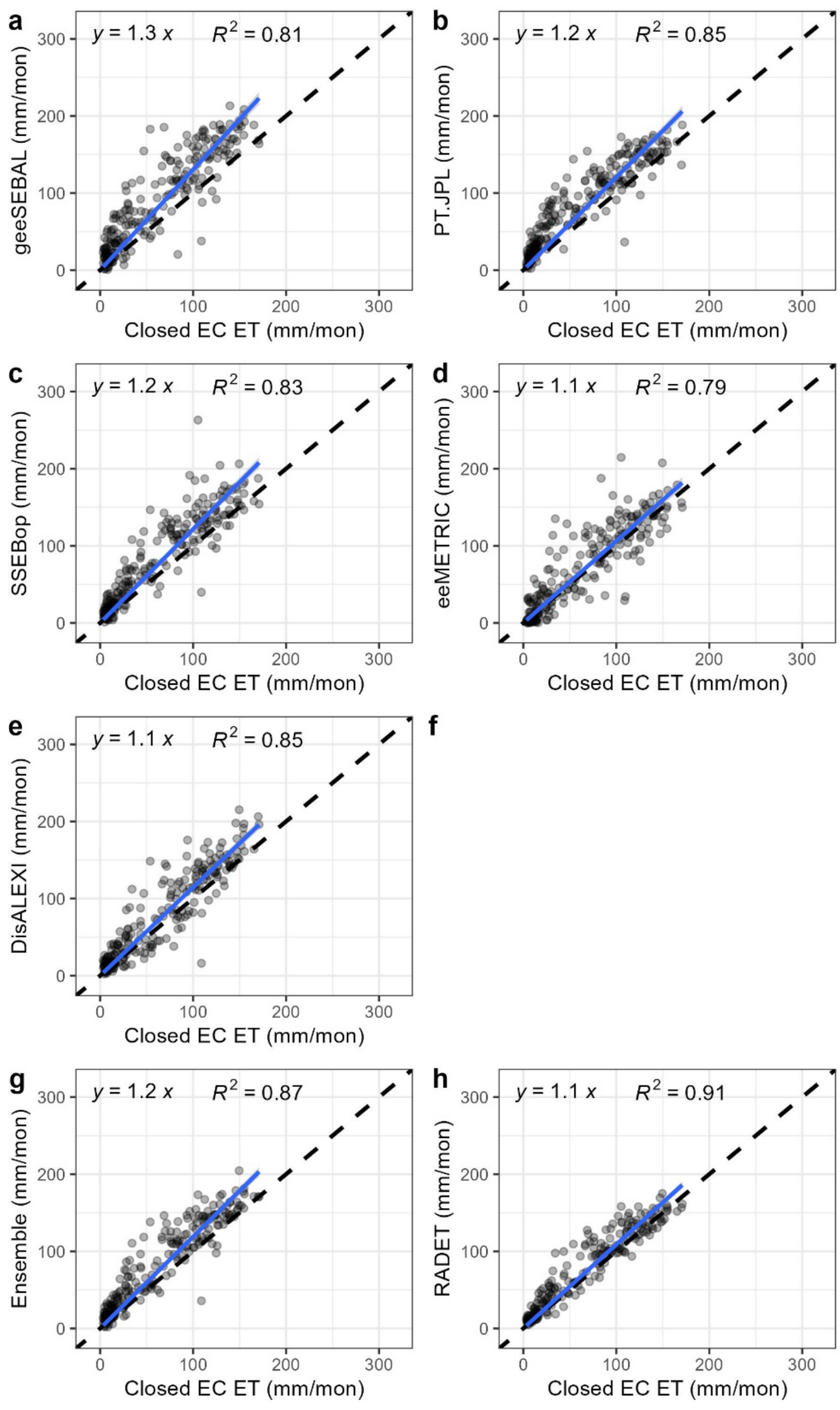

Figure S13 Monthly model estimates versus in situ ET observations (EBR-corrected) over mixed forest sites. Panels (a)–(f) show individual OpenET model estimates, panel (g) shows the OpenET ensemble, and panel (h) presents RADET. The dashed line denotes the 1:1 line, and the solid lines represent least-squares regression lines forced through the origin.

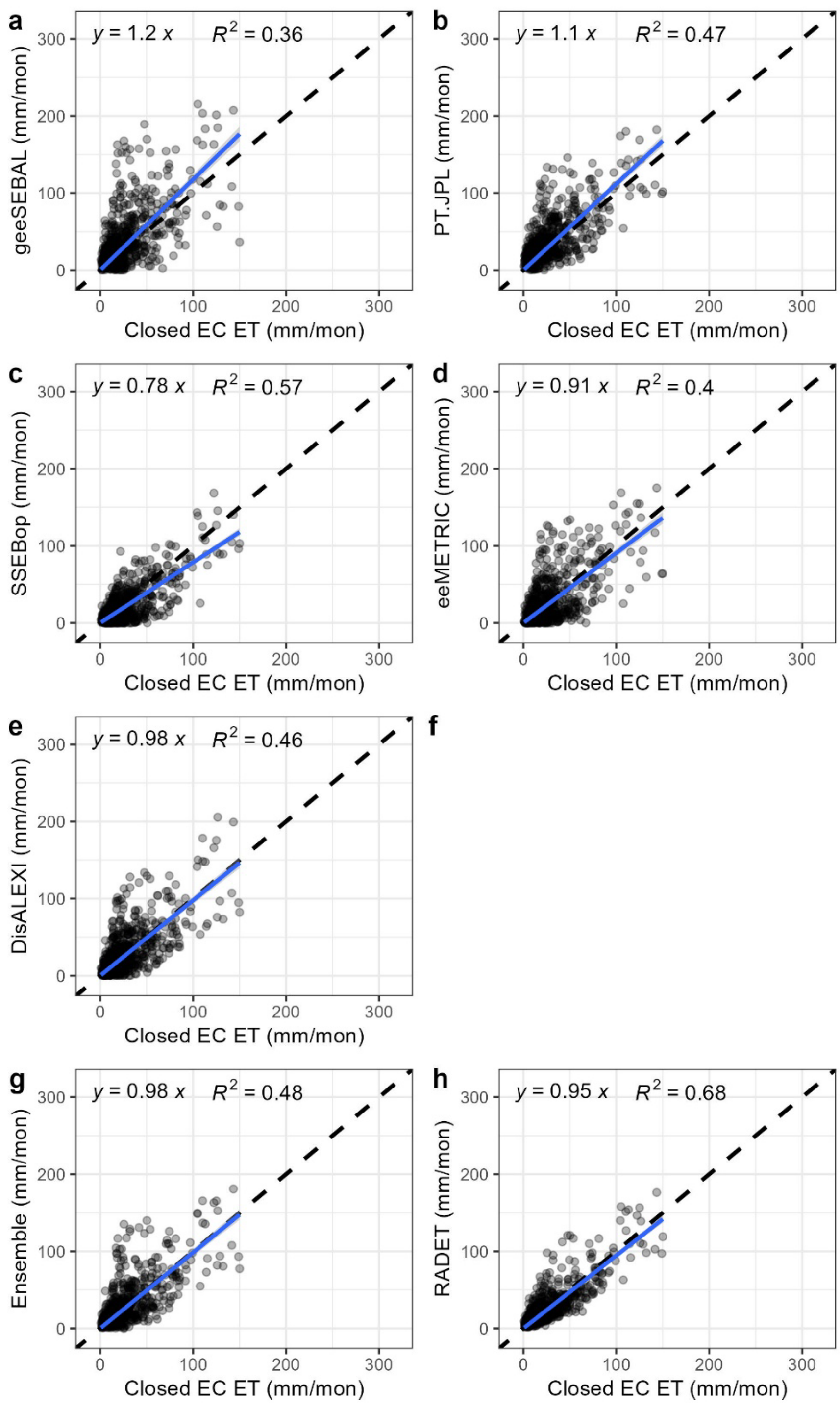

Figure S14 Monthly model estimates versus in situ ET observations (EBR-corrected) over shrubland sites. Panels (a)–(f) show individual OpenET model estimates, panel (g) shows the OpenET ensemble, and panel (h) presents RADET. The dashed line denotes the 1:1 line, and the solid lines represent least-squares regression lines forced through the origin.

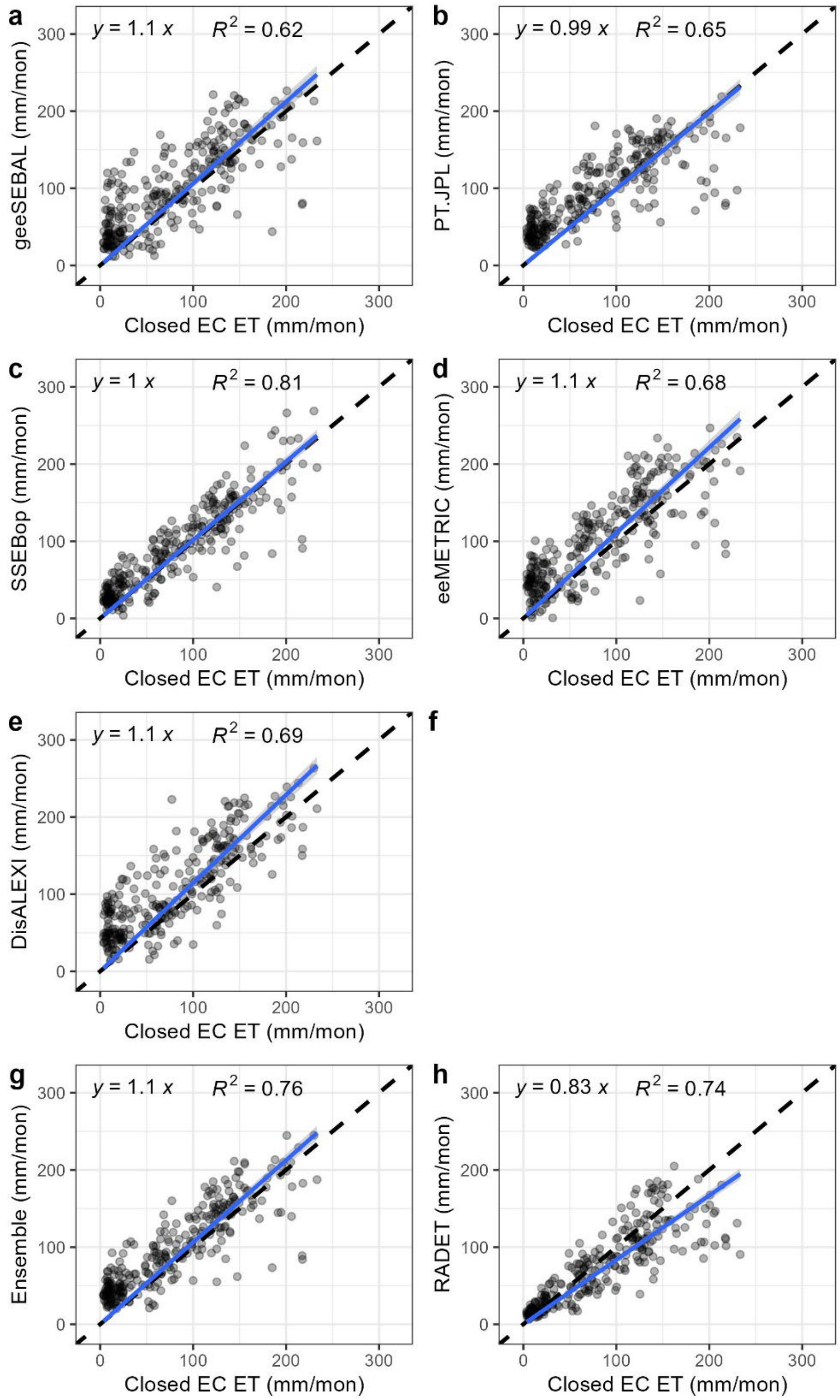

Figure S15 Monthly model estimates versus in situ ET observations (EBR-corrected) over wetland/riparian sites. Panels (a)–(f) show individual OpenET model estimates, panel (g) shows the OpenET ensemble, and panel (h) presents RADET. The dashed line denotes the 1:1 line, and the solid lines represent least-squares regression lines forced through the origin.